Developing Singlet-Triplet Qubits in Gallium Arsenide as a Platform for Quantum Computing

Citation

Harvey, Shannon P. 2019. Developing Singlet-Triplet Qubits in Gallium Arsenide as a Platform for Quantum Computing. Doctoral dissertation, Harvard University, Graduate School of Arts & Sciences.

Developing Singlet-Triplet Qubits in Gallium Arsenide as a Platform for Quantum Computing

A DISSERTATION PRESENTED
BY
SHANNON PASCA HARVEY
TO
THE DEPARTMENT OF PHYSICS

IN PARTIAL FULFILLMENT OF THE REQUIREMENTS
FOR THE DEGREE OF
DOCTOR OF PHILOSOPHY
IN THE SUBJECT OF
PHYSICS

HARVARD UNIVERSITY
CAMBRIDGE, MASSACHUSETTS
MAY 2019

Thesis advisor: Professor Amir Yacoby Shannon Pasca Harvey

Developing Singlet-Triplet Qubits in Gallium Arsenide as a Platform for Quantum Computing

ABSTRACT

There is a huge, worldwide effort to build a quantum computer due to its potential to perform chemical and materials simulations and to break current cryptography schemes. While there has been incredible progress in recent years, each potential platform still faces meaningful obstacles. The singlet-triplet qubit in gallium arsenide, which is based on electric spin, boasts several advantages, including fast single-gate times and readout, long lifetimes, and a clear path to large-scale integration using current semiconductor manufacturing techniques. However, it also suffers from electric and magnetic field noise that limits coherence time and weak two-qubit interactions, which have prevented the construction of multi-qubit systems so far. In this thesis, I will discuss my research measuring and working to improve noise and entangling gates in singlet-triplet qubits and will examine the viability of the singlet-triplet qubit as the building block for a quantum computer.

By measuring the dynamics of the electric and magnetic field noise that the singlet-triplet experiences, we can develop an understanding of their origins and how to reduce their impact. The singlet-triplet can be operated rapidly enough to use it as a sensor and directly measure the fluctuating magnetic field arising from the nuclear spins in the semiconductor heterostructure surrounding it. We use Hamiltonian parameter estimation, a technique that maximizes the rate at which we learn information, given the strange properties of quantum measurement, to measure magnetic noise to within 15 μT at a rate of 2 kHz, and we use these measurements to provide real-time feedback to system controls, increasing the coherence time by a factor of 30. Charge noise has much larger high-frequency components than magnetic noise, and thus requires use of dynamical decoupling methods borrowed from NMR to measure it. We measure its power spectrum up to 1 MHz and find that it has a 1/f spectrum. We perform these measurements for several different devices and have begun to determine how our growth and fabrication processes affect dephasing.

Placing a high-impedance resonator between two singlet-triplet qubits to mediate their interaction shows promise as way to create long-distance entanglement and to increase the speed of the entangling gate. We analyze this gate theoretically, finding that we expect the fidelity to be over 95%, with a straightforward path to increasing it to above 99% with improved resonator parameters. However, because the singlet-triplet qubit is extremely sensitive to changes in its electrostatic environment, which can be affected both by the resonator's fabrication process and the presence of the proximal resonator gate, implementing this gate experimentally is challenging. We have developed processes for fabricating narrow, thin, NbN resonators directly adjacent to the double quantum dots that compose singlet-triplet qubits. These processes yield quantum dots that can be tuned into low-noise, stable singlet-triplet qubits, and superconducting resonators with impedances over 1 kΩ.

Contents

AUTHOR LIST

Chapter 2 has been adapted from reference [87]. "Suppressing qubit dephasing using real-time Hamiltonian estimation." Michael D. Shulman*, Shannon P. Harvey*, John Nichol*, Andrew Doherty, Stephen Bartlett, Vladimir Umansky and Amir Yacoby. Nature Communications 5: 5156 (2014).

Chapter 3 has been adapted from reference [33]. "Coupling two spin qubits with a high-impedance resonator." Shannon Harvey, Charlotte L.G. Bøttcher, Lucas A. Orona, Andrew Doherty, Stephen Bartlett and Amir Yacoby. Physical Review B 97, 23: 235409 (2018).

* denotes equal contribution.

Publication List

9) T. Botzem, M.D. Shulman, S. Foletti, **S.P. Harvey**, O.E. Dial, P. Bethke, P. Cerfontaine, R.P.G. McNeil, D. Mahalu, V. Umansky, A. Ludwig, A. Wieck, D. Schuh, D. Bougeard, A. Yacoby, and H. Bluhm. "Tuning methods for semiconductor spin–qubits." *Physical Review Applied* 10, 5: 054026 (2018).

8) L.A. Orona, J.M. Nichol, **S.P. Harvey**, C.G.L. Bøttcher, S. Fallahi, G.C. Gardner, M.J. Manfra, and A. Yacoby. "Readout of singlet-triplet qubits at large magnetic field gradients." *Physical Review B* 98, 12: 12504 (2018).

7) **S.P. Harvey**, C.G.L. Bøttcher, L.A. Orona, S.D. Bartlett, A.C. Doherty, and A. Yacoby. "Coupling two spin qubits with a high-impedance resonator." *Physical Review B* 97, 23: 235409 (2018).

6) A. Pal, J.M. Nichol, M.D. Shulman, **S.P. Harvey**, V. Umansky, E.I. Rashba, Amir Yacoby, and Bertrand I. Halperin. "Electron spin-flip correlations due to nuclear dynamics in driven GaAs double dots." *Physical Review B* 95, 3: 035306 (2017).

5) J.M. Nichol, L.A. Orona, **S.P. Harvey**, S. Fallahi, G.C. Gardner, M.J. Manfra, and A. Yacoby. "High-fidelity entangling gate for double-quantum-dot spin qubits." *npj Quantum Information* 3, 1: 3 (2017).

4) J.M. Nichol, **S.P. Harvey**, M.D. Shulman, A. Pal, V. Umansky, E.I. Rashba, B.I. Halperin, and A. Yacoby. "Quenching of dynamic nuclear polarization by spin-orbit coupling in GaAs quantum dots." *Nature Communications* 6: 7682 (2015).

3) M.D. Shulman*, **S.P. Harvey***, J.M. Nichol*, S.D. Bartlett, A.C. Doherty, V. Umansky, and A. Yacoby. "Suppressing qubit dephasing using real-time Hamiltonian estimation." *Nature Communications* 5: 5156 (2014).

2) O.E. Dial, M.D. Shulman, **S.P. Harvey**, H. Bluhm, V. Umansky, and A. Yacoby. "Charge Noise Spectroscopy Using Coherent Exchange Oscillations in a Singlet-Triplet Qubit." *Physical Review Letters* 110, 14 (2013).

1) M.D. Shulman, O.E. Dial, **S.P. Harvey**, H. Bluhm, V. Umansky, and A. Yacoby. "Demonstration of Entanglement of Electrostatically Coupled Singlet-Triplet Qubits." *Science* 336, 6078: 202–5 (2012).

* denotes equal contribution.

Listing of figures

Acknowledgments

I want to thank my advisor, Amir Yacoby, for hiring me and teaching me so much about experimental physics, and for giving me a great deal of independence to explore what I was interested in and develop my own identity as a scientist. He's incredibly smart, and has a keen eye for selecting problems, which makes it a lot of fun to work with him. I don't feel I can adequately thank him here; instead, please read the remainder of these acknowledgments and this whole dissertation as a tribute to the opportunities I've gotten by working in his group.

I am also grateful to my other committee members, Bert Halperin and Ron Walsworth. There's little I can say about Bert that hasn't been said by many before, but I will add my voice to the chorus. The questions he asks always indicate that he is not only listening, but also performing any calculations necessary to understand whatever physics we're discussing in his head; watching him think might qualify as a spectator sport. In turn, he gives serious consideration to any question you ask him, and is comfortable saying when he doesn't know (but typically he has an idea of whom you should go to). Having Ron on my committee has also been a great asset. He is so much fun to talk to, and a great listener who has provided a lot of essential support to me. I really admire the way he selects and tackles problems, and appreciate that he's taken the time to help explain how that process works for him. He's always been eager to give advice and do what he can to help, and I've gained a lot from that.

I want to first thank Mikey Shulman for being gracious enough to let me imprint on him like a baby duck and follow him around constantly for my first couple years, trying to learn everything he knew and be just like him. I realize now that he was my coach. I'm not very good at sports, and I'd never had someone work with me like that, engaging with my work, pointing out what was wrong and how I might approach things differently. While I was incredibly grateful for any time he spent with me, until I became a "coach" myself, and began to think about what the point of it was, I didn't realize what it had meant to me: the extent to which it taught me that my work and education were valuable, and worth the effort of paying attention to.

I also worked with Oliver Dial at the time, and again was so unbelievably spoiled. It's a privilege to simply work near Oliver. You carry some piece of your mentors with you, and there are parts of my life where I feel I am "Olivering," in particular when I decide to automate something that may not need automating, even though I think that when Oliver did that he would spend about a day on something that would save us weeks of work and my ratio is… higher. But it's also when I spend a few extra minutes making a graphic that gives some intuition for a complex idea, when I make the effort to really understand all the machinery that undergirds an experiment, and of course, when setting up a prank. Oliver taught me a lot, and he also pushed me forward, both by giving me opportunities and by encouraging me to grasp onto them myself, by believing that I could handle it.

I had the great opportunity to mentor two amazing grad students, Charlotte Bøttcher and Andrew Pierce. They share two powerful traits claimed by many but possessed by few: a deep enjoyment of their work and intense drive to grow. I marvel at the extent each has developed since I met them, and yet, I don't – I see them come in each day and work hard and their ability to meet an experiment wherever it takes them, even if it requires questioning their prior judgment, extensive troubleshooting and entering unfamiliar territory. They came into grad school at a very high level, but instead of polishing their best skills, they've dived in to find the areas in which they have the most room to grow.

Charlotte is incredibly tough (I'll just say that she determined the exact amount of cleanroom fab it is possible to do with a broken foot). I've worked closely with her for the past few years, and it's been incredibly enriching for me. Having a teammate to talk things through with, to share the work and the ups and downs with, and who will come up with ideas and figure out problems, has been so wonderful.

Andrew and I worked on different projects, but we ended up spending a lot of time together maintaining lab equipment. It was great to have a thoughtful voice to talk plans through with and make sure what we were doing made sense. He's now at the point where he's bursting with ideas about experiments, and I expect the next few years to be incredibly fruitful for him.

Pat Gumann played an essential role for me when I was first running my fridge and project independently after Mikey graduated. I was getting my sea legs for leading a project, and when something urgent and terrible happened I would call him, and no matter what time it was, he would appear minutes later, panting. And then we would clinically diagnose the problem and fix it. Need I say that nothing was ever that terrible? I am always trying to carry this with me, to react more slowly and more carefully. Pat is also one of the kindest people I have met, and I am so happy I can call him my friend.

I've also had the pleasure of working with Hannah Belcher for the past few years. She is so good at her job that she actually changed the way I approached mine. Within a few weeks of starting, she reached out to me to find out what parts of my load she could take over. Having someone work to support my research, who treated my time as valuable, and wanted to enable me to have more time to focus on what I'm good at, was incredibly validating, and doesn't happen much for grad students. In addition to the immense support she's provided for my work, she is also an really insightful, intelligent, and kind person, who makes a huge difference in people's lives, and is bound to do so much more in years to come.

At some point in the middle of grad school, Yuliya Dovzhenko and I began a weekly ritual of having a few scotches in her office on Thursday nights after everyone else went home. This soon became one of the highlights of my week, a time in which we could process the work we were doing, the struggles we faced, and to share strategies that had worked for us. Being a woman in physics can be deeply isolating, and having someone who shares many elements of your experience with whom you have rapport is so beneficial, and helped me put what felt like very personal experiences in a global perspective. I'm also glad that Francesco Casola and Rainer Stöhr eventually joined these "meetings," and that we got to learn from Rainer's own experiences and to yell as hard as we could at Francesco (in an attempt to talk over him, a feat that still has not been accomplished) without his minding too much.

Michael Kosowsky, of course, is the mysterious bunny-suited figure who would sidle up to me in the cleanroom and say "Did you see that article on ESPN? It was so unfair to the Pats." I'm lucky to have shared the lab with him, given the amount of responsibility he's taken on, how dependable he has been, and of course, so that I remain updated on any roster moves the Patriots have made recently. I got to share two offices with DiDi Wei, which was great fun because she is such a funny, smart, hard-working scientist. I'm happy to have had her as an ally in the lab, and her friendship has meant a lot to me. I enjoyed working with John Nichol, where I learned a lot from his approach of quickly trying a number of approaches to a problem before homing in on the best. It's been rewarding to watch Lucas Orona grow into a strong scientist. Recently, I have also benefited from sharing fab and tuning issues with Yinyu Liu. Seung Hwan Lee is a continually positive, helpful presence in lab.

Vivek Venkatachalam has always been an inspiration to me. I had a ton of fun chatting with Mike Grinolds, and I find the advice he gave me then increasingly meaningful and helpful today. Ben Feldman embodied the characteristics you want in a coworker; it has been great to catch up with him at conferences since. It was very informative to be fridge buddies with Sean Hart during his last year, and I'm still happy I went bowling with him and Andrew during lunch that one time. I also want to thank Angela Kou, Lucas Thiel, Susanne Müller and Timo Wagner for bringing much fun to lab during their too-short times here. And I have so many other Yacoby Lab members to thank for enriching my time here, far too many to list here.

Jim MacArthur, whom I bothered very, very frequently, was truly one of the best parts of grad school. I went to Jim when I needed him to design a part, I went to Jim so he could tell me that in fact my DAC was working fine but I was doing something wrong, but most of all, I went to Jim to chat about electronics and anything else on my mind. In addition to his incredibly deep understanding of electronics, Jim has a great sense of what is worth spending time on, designing parts so that they are good enough for your experiment but not over-engineered, and the short path there. This is really what grad school was about for me, the opportunity to get near people who know how to approach problems, and watching them do it, then trying to emulate them.

Stan Cotreau plays an essential role in the Physics department, teaching students how to machine, as well as how exist in a community. He is always ready to levy criticism, but he leaves no doubt that it comes from a place of care and a desire to help you grow. Stan was happy (I mean, in a curmudgeonly way) to retrain me on machines I'd forgotten how to use and to talk through how to approach complicated projects. I would often interrupt his lunch hour to chit chat, and he's given me some of the best advice I've ever received. It was lovely to get to know him during grad school.

I had such a great experience working with theorists Stephen Bartlett and Andrew Doherty on the Hamiltonian estimation and resonator projects. They have impeccable calibration of how deep a theorist should get in an experiment they are advising on, and in so doing were able to help us design several experiments and learn a lot of new physics. I never would have had the confidence to write a theory paper without their guidance, and I also benefited from their visits to Boston, where they shared a lot of insight into academic careers with me and were just so fun to hang out with.
I was lucky to get material from Mike Manfra. He was in frequent contact when I had problems with tuning quantum dots or fab issues, and supplied us a lot of great material. I've really enjoyed catching him up with him at conferences over the years. His students John Watson and Saeed Fallahi were always quick to respond to my emails and provided lots of useful information. I want to thank Melissa Franklin for always being ready to joke around with me or chat about the world of physics, and also for existing.

I'm so grateful to all the people who helped me figure out what to do next. I particularly want to thank Ron Walsworth, Julia Mundy, and Nathan Bishop, who repeatedly took time to educate me, support me, and advise me. They made a stressful process far more pleasant, and helped me better understand what I wanted to do next and how to put it in the broader context of a career.

I want to thank everyone in ye olde Marcus Lab and ye newe Kim Lab for providing me with various Swagelok bits, Stycast, and so forth when I was most desperate. I also want to thank Nick Hutzler, for helping me with water jetting and for always being the first person to respond when I sent out an email asking if anyone had a tool I absolutely needed in the next 10 minutes. Pawel Latawiec, Bart Machielse, and Amirhassan Ansari of the Loncar group have been my Elionix F125 and HSQ gurus, training me and answering questions, then serving as the colleagues I contact when my process stops working, to find out if the machine is genuinely misbehaving or if I'm just doing something wrong. I thank Chengye Liu and Donhee Ham for letting me use Sonnet in the Ham Lab. Jingyee Chee was my gallium arsenide brethren, the one person I could compare results with when ohmics suddenly stopped working. I guess I liked going running with Swati Singh, but I preferred when we turned our focus to drinking wine and eating french fries together. I really enjoyed my lunches with Ruffin Evans over the years, and gained a lot from our discussions of how the system works and how to improve it. Across the world, I particularly benefited from my contact with the members of David Reilly's research group, including James Colless, Xanthe Croot, Seb Pauka and John Hornibrook, who ran into many similar tuning and fab issues as me and were able to help me out of a few jams.

I had a lot of fun teaching; all of the platitudes about learning as much from your students as you teach them are true. I got to work with Carey Witkov and Keith Zengel in this, and they were indispensable in developing awesome new projects and making the class run well. I was also delighted to have Brian Warner start doing research with me after being in my class. Brian was thrown into a graduate-level project, and quickly picked up a ton of new skills, from cleanroom fab to dilution refrigerator wiring, as well as quantum mechanics. We really enjoyed having such a smart and talented student in lab. It was also fun to have my fantastic students Anna Biggs and Yunchao Zhang join the lab, and a few years earlier to share a desk with Brian Zhang.

Lisa Cacciabaudo was always able to answer my questions and help with concerns. HUIT has been with me through a lot of submitted tickets; in particular I want to thank Reza Ahrabi and Judit Flo Gaya who helped me a great deal with the weirdly difficult challenge of contacting a license server on a different subnet. John Sweeney and Tiffany Lee guided me through my time as safety officer and aided me in keeping the Yacoby Lab safe.

My PhD would have been far worse if I hadn't received so much advice and help from all the workmen in LISE – Connie, Sean, Bobby, Paul, Larry, Bill, Stephen, and many more. They responded quickly to dozens of work requests, talked through my vague ideas with me, then brought them to fruition. I am also indebted to Frank Morrissey, who always treated me like a queen, and Stuart McNeill, who will go into in my personal hall of fame for saying, when he met me, "so you're the lady with all the work orders."

I spent years of my PhD in the cleanroom facilities at Harvard, and the staff were invaluable to my work. JD Deng has an incredibly hard job and does it with grace. Yuan Lu, ebeam master, was always ready to help me figure out how to make changes when my processes stopped working, come fix the ebeam as soon as I called him, desperate to get it fixed fast enough that I could still fit my write in, and would throw me an hour or two of time when I needed it. When the tool I wanted to use was broken, I usually ended up grabbing Jason Tresback, whether he was in charge of it or not, since he's always in the cleanroom and could usually figure out how to get it working. He was also always happy to help me up my game on the AFMs and profilometers. Guixiong Zhong is in charge of many of the tools that get most used and abused in the cleanroom, and as such received many emails from me, and occasionally my hunting him down in the cleanroom, and was very good about getting things back up and running ASAP. Kenlin Huang was very nice when Charlotte and I pretty much moved into his office when RIE-13 was down, and was always ready to help us develop new recipes, learn new tools, and of course, replace lost wafers. I am also grateful for occasional conversations about broken tools and process issues (sensing a theme here?) with John Tsakirgis, Steve Paolini, Mac Hathaway and Ed Macomber.

A few stellar people from companies: Nick Dent of Oxford and Giorgio Frossati and Arlette de Waard of Leiden, of course, as well as Brian Stoddard at Cryomech, Romaine Deterre at AlazarTech and of course my good friends Tim at Chris' Coffee and Scott at La Marzocco, who helped talk me through some basic espresso machine troubleshooting and repair. When I asked Scott if he thought I could handle some repairs myself, he said "You said you were from the Harvard Physics Department? Yeah, I think you got this." In software land, all the COMSOL and Sonnet support people have been fantastic.

Now I will thank some books. Those who know me won't be surprised...When I was a freshman in college, trying to figure out what I wanted to do with my life, my chemistry professor recommended Primo Levi's "The Periodic Table" to the class. At the time, I didn't know any scientists, and I had no idea what a career in science looks like once you stop taking classes. This book gave me my first grasp of how an experimental scientist uses their mind and what they get from their work, and science began to seem like something I could really spend my life on. Many years later, I'm amazed at the extent to which the stories speak to just what I enjoy about my research.

On the other side of graduate school, I read Randy Shilts's "And the Band Played On" as a break just after taking my quals. At this point, I had been around long enough to be cynical about everyone's motivations and the importance of what we are doing, and this book brought home to me starkly the ethical duty of scientists. As little as it may seem to matter in the everyday spin of things, to be happy with the life I've chosen, I need to keep that voice turned on in my head.

As someone constantly seeking advice, I am lucky to have been blessed with a bounty of wonderful parents. I owe everything to my mom and dad. They have never told me who I am or who I am supposed to be, but have always taken me seriously and treated me with respect. I am always trying to follow their example of living intently and ethically. If my life is anything like theirs, I will consider myself an immense success. I owe so much to Calvin, whose intense interrogative spirit has made me question everything, but has also forced me to learn how to hone an argument, and really know when I believe something. And I thank him for instilling me with my early-adopter traits, which probably got me here and then added an extra year. I owe so much to BJ, who infuses everything she touches with joy. I try to emulate that quality, even if I am not always successful. I also want to thank my brother, as I have no doubt that any ability I have to survive the exile in guyville that is a career in physics comes from my perpetual little-sisterhood, always wanting to spend more time with my big brother. It's wonderful that he's brought Paige, my now sister-in-law, into my life, as she's been a really positive, supporting presence for all of us. It has been so great to be near my family during grad school and get to know them as an adult. I also thank my friends, in particular Lisa, Eunice and Meredith, for providing humor, perspective, and love throughout these long years. To the women of Wait Terrace – I continue to be so inspired by all of you.

I said goodbye to my grandmothers during grad school, a time in which I grew to appreciate how lucky I am to be descended from them. In my family, women's intelligence, creativity, and ambition are so obvious as to be unremarkable, and in entering the larger world I've learned how rare and how valuable that is. It's because of the many women I am related to who have pursued their dreams, uninterested in what any one else thought of it. They may not have gotten the opportunities they deserved, nor the credit that was due to them; yet still they kept going. It is in the work of such people that the world moves forward, whether they sense it in their lifetimes or not. I will also add that, for better or worse, the major uniting drive of my family has been the desire to work, and to do our jobs well. For numerous reasons, sad yet common, many of my ancestors did not get their full chance to do that. I remain everlastingly grateful for everything they did to create a world, to create a family, in which that is truly the least of my concerns.

Finally, we come to Will. Will, spending these years with you has been the greatest joy of my life. None of this makes any sense without you.

0

Introduction

During the last two decades, there has been intense effort directed towards building a quantum computer due to its numerous applications. A quantum computer that could provide useful applications requires millions of qubits, precisely engineered and with extremely low noise [71]. There are number of different possible systems in which it might be implemented, including superconductors, quantum dots, and trapped ions, whose state-of-the-art systems vary from 2 to nearly 100 qubits. Due to the intense requirements, while each platform has shown certain advantages, there remains a huge amount of progress before it is clear if any of them can reach this incredible peak.

When I began graduate school, the team I was working with in the Yacoby Group was beginning to take data showing that they had entangled two singlet-triplet (S-T_0) qubits. With that, one might say that the initial proof-of-principle set of experiments for the S-T_0 in gallium arsenide (GaAs) had been completed. In the years before that, The Yacoby group and others had demonstrated singlet-triplet qubit initialization, readout, and universal quantum control. These properties were all quite promising: loading took only nanoseconds for over 99% fidelity, and when using RF reflectometry, readout was under a microsecond for 98% fidelity. The gate speeds were tunable, from DC to over a GHz for both of the axes of control (with some caveats).

Yet of course, proof-of-principle is merely the first step. Building a functional quantum computer is an immense undertaking, and requires extensive optimization of nearly every aspect of the system. In the short term, though, we are simply trying to push forward so that we can perform somewhat more complicated quantum gates. That requires that we determine the main limiting factors of the S-T_0 qubit, and then focus on attacking them. At the time, I think those would be described as:

1. **Nuclear magnetic field noise.** The fluctuating nuclear spin bath in GaAs couples to the singlet-triplet qubit and causes dephasing. This was seen as one of the primary impediments to spin qubits in GaAs.
2. **Charge noise.** Charge noise also couples to the S-T_0 qubit, limiting the fidelity of both single and two-qubit gates. It's not clear how to reduce the amount of charge noise in semiconductors, though many proposals exist for different ways to instead reduce the qubit's sensitivity to charge noise.
3. **Entangling gate.** The capacitive entangling gate is far slower than single-qubit gates, and

because it falls off dramatically quickly with distance, there was no clear path to scaling to many qubits. The Bell state fidelity measured in the initial demonstration, 72% [86], is not sufficient for performing algorithms.

4. **Fabrication and tuning of devices.** There are a few qubit designs with high yield in both fabrication and tuning, but changing the design or process can lead to numerous side effects. While for single and two-qubit devices, it is possible to perform experiments with low yield fabrication and long periods of time tuning up quantum dots, the next generation of experiments will require these to be improved.

This is not to say these are the only challenges these qubits faced, but that these were the ones that most immediately impeded progress, and without solving these, we could not properly investigate problems likely to arise later.

My PhD thus focused on studying these issues and developing experiments to test some of the ideas we came up with solve them. In this thesis, I will highlight the work I did on these problems. The first chapter introduces the concepts in quantum computing, quantum dots, and S-T_0 qubits needed to understand the remaining chapters. In the second chapter, we present the results of an experiment we performed to use Hamiltonian estimation to quickly measure the nuclear magnetic field bath that coupled to the qubit, and to use that information to extend the qubit's T_2^* to almost $3\,\mu$s. In the third chapter, we propose a scheme to couple S-T_0 qubits to high-impedance resonators, which would increase the speed and range of its entangling gate. In the fourth chapter, we describe our work measuring S-T_0 qubits with adjacent resonators. We found that the changes to the qubit fabrication process needed to incorporate resonators led to a number of unanticipated issues in tuning and measuring the quantum dots, and discuss them as well as the solutions we developed. In the fifth chapter, we discuss the fabrication process for the resonators, and the various measurements we've performed to characterize them. Finally, in the conclusion, we will discuss some of the work that the larger community has done to attack the major issues in the field over this time span.

We can also consider how the research in this thesis has advanced our understanding of the S-T_0 qubit and improved the performance of GaAs based qubits in regards the four challenges listed above.

For the first item, nuclear magnetic field noise, our results in Chapter 2 have made it a "solved" problem until the effects of charge noise are significantly reduced; it no longer prevents experiments from moving forward.

For the second item, my research primarily worked around charge noise, rather than directly engaging with it. The resonator and Hamiltonian estimation may be seen as approaches to reducing its effects without actually reducing it. We did perform measurements of charge noise in devices with resonators, and saw a sharp increase in high-frequency charge noise, and have hypothesized that the inclusion of an ALD layer in the fabrication caused this. However, we have not tackled the question of charge noise's origins head on.

For the third item, the entangling gate, our theoretical proposal on coupling S-T_0 qubits with resonators is a promising approach to solving the issues of the entangling gate. We discuss our work building an experiment to do that at length in this thesis. Initial qubit devices with resonators were not tunable, but we were ultimately able to rectify these issues.

This connects to the fourth item, fabrication and tuning. In the process of making and measuring a number of qubit devices with resonators, we have optimized many facets of the fabrication and tuning process. Our fabrication yield is consistently above 80%. Device design remains heavily dependent on intuition and simple simulations, although our efforts in tuning have made testing the different designs far quicker.

Experimental quantum computing research often follows a fine line between thinking about abstract 0s and 1s and thinking about the more complicated system underneath. It's often a cyclical process, as we spend time building the experiment, grappling with all the details, and then as the experiment is "running," we can focus on the high-level values. But at some point, the building blocks need to be improved. The first experiment discussed in this thesis, in Chapter 2 is a high level experiment, and Chapter 3 is a proposal for another high-level one. Chapters 4 and 5, however, are about the experimental details of how to get there. I believe this research has improved understanding of the S-T_0 qubit in GaAs and hope it paves the way for it to be developed further as a competitive architecture for quantum computing.

1

Singlet-Triplet Qubits

1.1 QUANTUM INFORMATION

We start with the briefest of introductions to quantum computing. Readers interested in learning more about the topic should read some of the excellent teaching materials available, including [70, 65]

In this section, we'll build up the framework for understanding single-qubit gates, loading, and measurement. More sophisticated concepts, such as entanglement fidelities, quantum metrology, and dynamical decoupling are described as they are become relevant in the remainder of this dissertation.

A qubit, or quantum bit, is a two-level quantum system. Qubits are analogous to classical bits, which can be in the states 0 or 1, but because they are quantum systems, qubits can be not only in the $|0\rangle$ or $|1\rangle$ states, but also any superposition of those. The state can be described as

$$\psi = \alpha|0\rangle + \beta|1\rangle, \tag{1.1}$$

where $|\alpha|^2 + |\beta|^2 = 1$. This can also be shown graphically using the Bloch sphere, show in Fig. 1.1**a**, where the qubit's state is described as a point on the surface of the sphere, with

$$\psi = \cos(\frac{\theta}{2})|0\rangle + \sin(\frac{\theta}{2})(\cos\phi + i\sin\phi)|1\rangle. \tag{1.2}$$

Describing qubit states in this manner helps develop intuition for understanding the action of single-qubit gates, which we can think of as being used to rotate the qubit's state around the Bloch sphere. We perform them by turning on energy splittings between states on the Bloch Sphere. This can be solved for quantitatively using the Schrödinger equation,

$$i\hbar\frac{d|\psi\rangle}{dt} = \hat{H}|\psi\rangle, \tag{1.3}$$

where $\hat{H}$ represents the qubit's Hamiltonian. For two-level systems, there is a limited set of physical

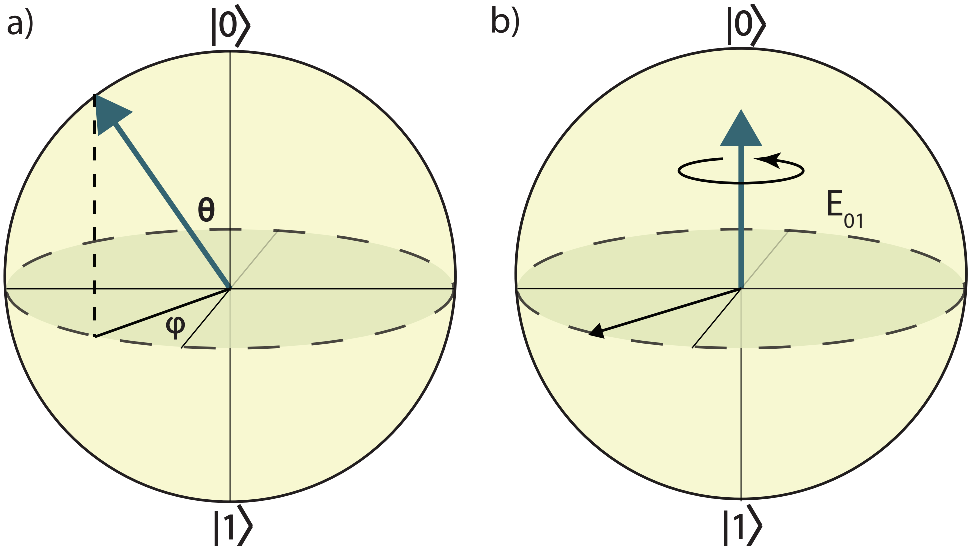

Figure 1.1: a. Schematic of a Bloch Sphere. b) Rotation around Bloch Sphere

Hamiltonians, and these can be written as:

$$\hat{H} = \frac{1}{2} \sum_{i=x,y,z} E_i \hat{\sigma}_i, \tag{1.4}$$

where σ_i are the Pauli matrices and E_i is the difference in energy between the corresponding Pauli vectors. For clarity of expression, we consider the Hamiltonian that is constant for a time t, but it is trivial to extend to those that fluctuate with time. The Schrödinger equation can be solved for two-level systems, with the unitary operator evaluating to

$$\hat{U}(t) = \cos(\frac{\omega t}{2}) I - i \sin(\frac{\omega t}{2})(\hat{\sigma} \cdot \hat{n}), \tag{1.5}$$

where we've written $\omega = \sqrt{\omega_x^2 + \omega_y^2 + \omega_z^2}/\hbar$, $n_i = \frac{\omega_i}{\omega}$, and $E_i = \hbar\omega_i$. We can visualize this on the Bloch sphere as in Fig. 1.1**b**, with a splitting $E_{01}\sigma_z$ causing rotation around the z-axis at a rate $\omega = E_{01}/\hbar$. To perform quantum algorithms, we will need to be able to access the entire surface of the Bloch sphere, which requires the ability to turn on splittings in two directions; this is known as universal control.

We will now discuss an example of performing a quantum gate, known as a Ramsey pulse sequence, which might be used to measure the energy splitting in the z-direction. In general, all quantum gates begin with loading a known state; in this case we will consider the $|0\rangle$ state. Without the ability to load with high-fidelity, it will be impossible to know what state the qubit ends up in. The pulse sequence requires 3 pulses: the first is a "preparation," $\pi/2$ pulse around the x-axis. Next, we rotate around the z-axis for a time t. Finally, we perform a "readout," another $\pi_x/2$ pulse, to rotate the state back to the z-axis. To find the final state of the qubit, we can multiply the pulses together, and let them act on the initial state:

$$\begin{gathered}
\psi_F = \hat{\sigma}_{x,\pi/2}\hat{\sigma}_{z,t}\hat{\sigma}_{x,\pi/2}|0\rangle \\
\hat{\sigma}_{x,\pi/2} = (I - i\hat{\sigma}_x)/\sqrt{2} \qquad\qquad \hat{\sigma}_{z,t} = I\cos(\frac{\omega t}{2}) - i\hat{\sigma}_z\sin(\frac{\omega t}{2}) \\
\Rightarrow \psi_F = \sin(\omega t/2)|0\rangle + \cos(\omega t/2)|1\rangle
\end{gathered} \tag{1.6}$$

In order to experimentally determine the action of the gate, a measurement must be performed. These measurements are quantum mechanical, which means that they are probabilistic. We will consider measurements that are projective, meaning that they fully collapse the quantum wave function onto the measured eigenstates. In this case, the probability of measuring each state is equal to the square of the inner product of the wave function with the measurement eigenstates. We measure in the $|0\rangle$,$|1\rangle$ basis, and find:

$$P(0) = \frac{1}{2}(1 + \sin \omega t) \tag{1.7}$$

In an experiment measuring ω, we would vary t and then fit the collected data set to 1.7. We note that each such experiment requires that we run the pulse above many times for each time t. We measure either 0 or 1 after each pulse, so to fully render the curve, we must average many measurements together. Some applications of this Ramsey measurement will be discussed in Chapters 2 and 4.

Finally, we consider the effects of noise. Here, we will consider only quasistatic noise, which is constant within a pulse but varies across them, for mathematical simplicity, but we note that the concept also applies to higher frequency noise. We assume that ω follows a Gaussian distribution with mean ω_0 and standard deviation σ,

$$P(\omega) = \frac{1}{\sqrt{2\pi}\sigma} \exp(-(\omega - \omega_0)^2/(2\sigma^2)) \tag{1.8}$$

We are interested in how this changes the signal we measure, (1.7), and we now write its average value as

$$\begin{aligned}\bar{P}(0) &= 1/2\int P(\omega)\,(1+\cos\omega t)\;d\omega \\ &= 1/2(1+\cos(\omega_0 t)\exp(-\sigma^2 t^2/2)) = 1/2(1+\cos(\omega_0 t)\exp(-(t/T_2^*)^2)).\end{aligned} \tag{1.9}$$

This can be calculated using a Fourier transform. We've now defined $T_2^* = \sqrt{2}/\sigma$, the so-called inhomogeneous dephasing time, a name which arises from nuclear magnetic spectroscopy. We note that in the remainder of this thesis, we are typically discussing frequencies instead of angular frequencies, in which case $T_2^* = 1/(\sqrt{2}\pi\sigma_f)$. For higher frequencies of noise, the derivation becomes more complicated (it is well-discussed in [18]), and certain special cases are discussed in Appendix B.

1.2 QUANTUM DOTS

The discussion so far has not been specific to a given implementation of qubit. Now, we will start considering how to isolate a two-level quantum system using quantum dots. Quantum dots are systems in which particles confined in three dimensions, leading to an atom-like quantized energy level spacing [5]. While there are several different ways they can be made, the one we discuss here is known as lateral-gating. We start with a semiconductor heterostructure where electrons are confined to the interface between two different semiconductors, known as a two-dimensional electron gas (2DEG) [19]. Gates on the surface of the semiconductor are used to deplete the gas of electrons in the remaining two dimensions, leaving them only in the small region between the gates. An SEM image of three adjacent quantum dots is shown in Fig. 1.2**a**. When the resistance between the quan-

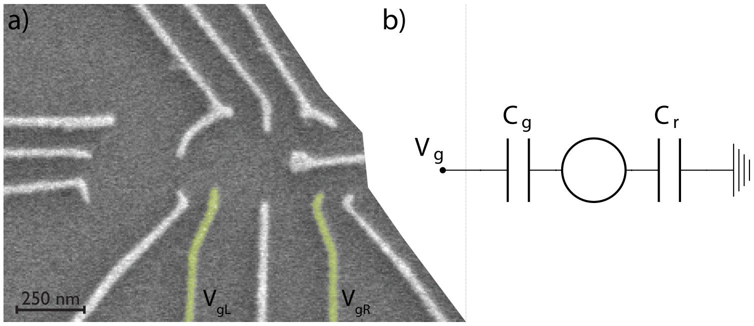

Figure 1.2: a) SEM of a double quantum dot with an additional sensing quantum dot at left. b) Cartoon of a quantum dot with one gate.

tum dot and the 2DEG adjacent to it (referred to from now on as the leads) becomes large enough, $R \gg h/e^2$, the electrons become localized in the quantum dot. In this thesis, we discuss quantum dots formed in a AlGaAs/GaAs heterostructure with the 2DEG 91 nm beneath the surface.

We can calculate the energy of quantum dot by treating it like a metallic object with total capacitance C and charge $Q = ne$, where n is the number of electrons it contains. We consider it to have a nearby gate with voltage V_g and capacitance to the quantum dot C_g. A cartoon of this is shown in Fig. 1.2**b**, where C_r is the rest of the capacitance, $C_r = C - C_g$. The energy of this is then

$$U(n, V_g) = (eN - eN_0 - C_g V_g)^2/2C = E_c/2(N - N_0 - C_g V_g/e)^2, \qquad (1.10)$$

where N_0 is the number of electrons in the dot when V_g is 0, and we've defined $E_c = e^2/C$, the electrostatic cost of adding an electron to dot [94]. We can see this by considering the chemical potential, the energy required to add the Nth electron to the dot.

$$\mu(N, V_g) = U(N, V_g) - U(N-1, V_g) = E_c(N - N_0 - 1/2 - C_g V_g/e) \qquad (1.11)$$

The difference between chemical potential for adding the Nth and Nth+1 electron is, as expected, E_c.

The quantum dots are designed to be near the size of the Fermi wavelength of the 2DEG, about 50 nm. They have capacitance of about 100 aF, leading to $E_c \approx 1$ meV. The orbital energy is approximately $E_n = \frac{n^2\hbar^2}{m^* R^2}$, where R is the dot's radius and n the number of electrons in the dot, and for the last electron is about 50-500 μeV in GaAs dots [75]. Since the electron temperature of the quantum dots is around 50-100 mK in most dilution refrigerators, under 10 μeV, we are well below the point where excited states become thermally occupied, and from now on consider all electrons to be in the orbital ground state with a well defined number of electrons. The electrons that are added to the quantum dot come from the leads, which the quantum dot is tunnel-coupled, allowing electrons to hop between the 2DEG and the quantum dot when the energy of an additional electron is at the Fermi level of the 2DEG.

We now consider two quantum dots next to each other, known as a double quantum dot (DQD). The equation for its potential energy is considerably more complicated than that for a single quantum dot, because in addition to their being an additional dot and gate, the dots also have cross capacitance. A full explanation is given in van der Wiel et al. [94], and here we give a minimal version to give some understanding. We ignore the effects of cross-capacitance. We consider two possible charge states: 0 electrons in the left dot and two in the right dot, and 1 in each dot, which we will refer to as the (0,2) and (1,1) states from now on. Because we are in the ground orbital state of this dot, from here on we will describe the orbital state of the DQD as referring to its distribution between these two charge states. Their difference in energy is

$$\Delta E = U(0,2) - U(1,1) = e\frac{C_{g,L}}{C_L}V_{g,L} - e\frac{C_{g,R}}{C_R}V_{g,R} + E_{c,L}/2(1 + N_{0,L}) + E_{c,R}/2(3 + N_{0,R}) \tag{1.12}$$

We now define $\alpha_i = e\frac{C_{g,i}}{C_i}$, $\{i = L, R\}$ as the lever arms for the V_g gates, which we now assume are connected to coaxial cable, allowing us to change their values on sub-nanosecond time scales. For our experiments, we also have a number of DC gates to tune the potential of the dots, and we'll assume that we use those to offset last two terms in the equation. Finally, we get

$$\Delta E = \alpha_1 V_{g,R} - \alpha_2 V_{g,R} = \epsilon. \tag{1.13}$$

We show the gates on the surface in Fig. 1.2**a**, and now define their difference to be the parameter ϵ, which will be our main control knob in performing experiments. We note that there is a second axis of control, $\alpha_L V_{g,L} + \alpha_R V_{g,R}$, which we will generally set to be constant at 0, so that in varying ϵ we move along the line shown in the figure. We note while ϵ as defined above is more physically meaningful in developing theory, in many experimental papers it is defined as the more directly controllable $V_{g,L} - V_{g,R}$. In this thesis, we will try to be clear about which meaning we are using.

Now, we write this energy difference in a matrix with the basis of $(0,2)$ and $(1,1)$. We also turn on tunnel coupling between the two dots, which takes the form $H_T = t_c|(0,2)\rangle\langle(1,1)| + h.c)$. In practice, this rate can be controlled by tuning the gates in between the quantum dots to change the potential barrier between the two dots. We add a couple of clarifying comments. First, we have been

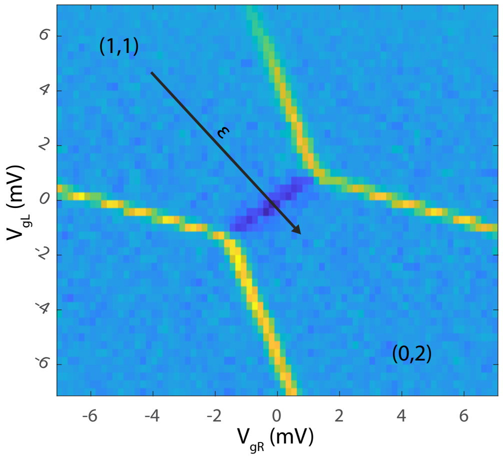

Figure 1.3: Charge Diagram near (1,1)-(0,2) junction. Differentiated date from scan sweeping V_{gL}, V_{gR} gates near the (1,1) and (0,2) charge junction. Yellow lines indicated charges moving into the DQD, and blue line represents charge moving between dots. Most quantum operations will be controlled by changing the value of ϵ, perpendicular to the junction.

discussing the difference in energy between the two orbital states. There is a choice in defining the Hamiltonian how to divide the energy between the $(0,2)$ and $(1,1)$ states; we do so symmetrically (with each state having $E = \pm\epsilon/2$), but others will do so with $(1,1)$ having 0 energy and $(0,2)$ having energy ϵ. Second, we have considered the energy states $(1,1)$ and $(0,2)$, but all of this is applicable to any states $(N, M-1), (N-1, M)$ where N, M are integers greater than 0. The simplest example is $(0,1)$ and $(1,0)$, which is often used for charge qubits.

$$H = \begin{pmatrix} \epsilon/2 & t_c \\ t_c & -\epsilon/2 \end{pmatrix}. \tag{1.14}$$

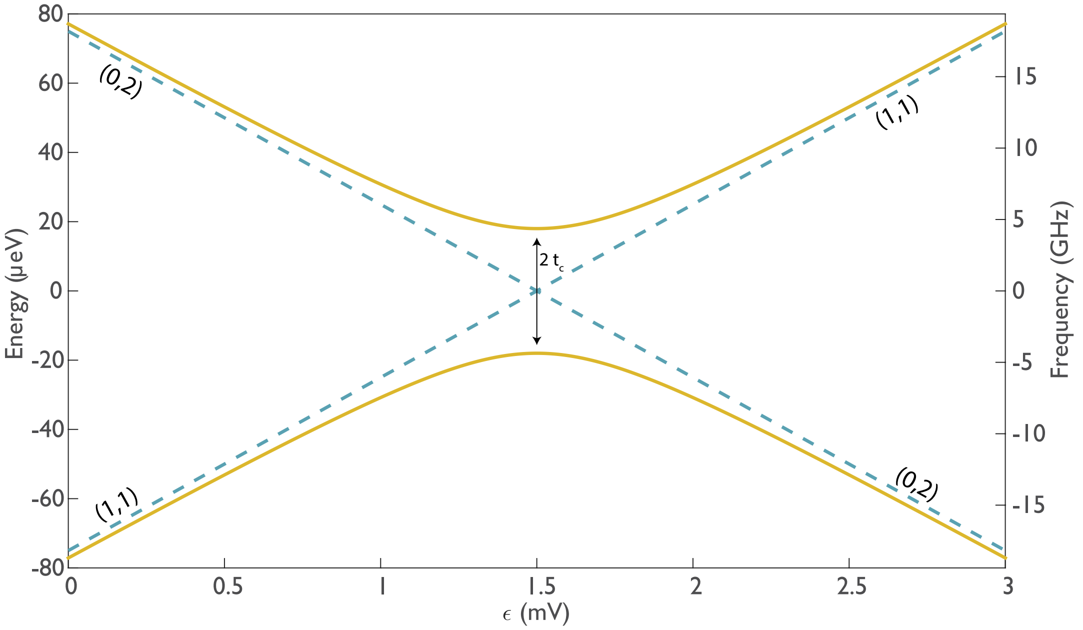

Figure 1.4: Energy diagram for the (0,2) and (1,1) states of a tunnel-coupled double quantum dot.

The eigenstates of this matrix have energy

$$E_i = \mp\sqrt{(\epsilon/2)^2 + t_c^2}. \qquad i = \{g, e\} \tag{1.15}$$

We will primarily be interested in the ground state, which has eigenstate

$$\psi_g = \{\sqrt{\frac{E_g + \epsilon/2}{2E_g}}, \sqrt{\frac{1}{2} - \frac{\epsilon}{E_g}}\} \tag{1.16}$$

While this is not the most intuitive equation, we see that ϵ passes through 0, then, the ground state has equal weight in the (0,2) and (1,1) states to minimize its energy. We will be interested in the charge distribution of the ground state,

$$Q_L - Q_R = |\langle\psi_g|(0,2)\rangle|^2 - |\langle\psi_g|(1,1)\rangle|^2 = \frac{\epsilon}{2E_g} \tag{1.17}$$

We see that this is proportional to $\frac{dE_g}{d\epsilon} = \frac{\epsilon}{4E_g}$.

1.3 Singlet-Triplet Qubits

At this point, we've defined the quantum dot well enough to begin thinking about it as a qubit. The idea of using quantum dots for quantum computation was first described in [52], and the singlet-triplet qubit proposed by Jeremy Levy [50]. There are a wide variety of quantum-dot-based spin qubits, defined primarily by the number of dots and electrons, but also by the spin states that make up the logical subspace and the type of drives applied. Often the most meaningful properties of the qubit arise from the extent to which it is 'spin-like' or 'charge-like.' In general, the charge-like properties arise when there are multiple quantum dots, and the qubit states are defined by which quantum dot the electrons are in. Typically, then the qubit's Hamiltonian can be controlled by applying a voltage to gates defining the quantum dot, which has the benefit of being a simple means of control, but the downside of coupling the qubit to charge noise. The 'spin-like' qubits are often defined in single dots, though there are also certain multi-dot systems in which they have been implemented. In these, both qubit states have the same spatial charge distribution, and the Hamiltonian is not shifted by applying a voltage to local gates, which decouples the system from charge noise but has the downside of making the qubit harder to control as well as making it susceptible to magnetic field noise. The singlet-triplet qubit has the somewhat unique property of being both a spin and charge qubit, depending on how it is biased. We will describe how this works in the remainder of this section.

Continuing with the tunnel-coupled double quantum dot from the previous section, we next endow the electrons with spin [35]. There are four possible combinations of spin states for two-electrons: the singlet state and three triplet states.

$$\begin{aligned} S &= \frac{1}{\sqrt{2}}(|\uparrow\downarrow\rangle - \downarrow\uparrow\rangle) \qquad & T_0 &= \frac{1}{\sqrt{2}}(|\uparrow\downarrow\rangle + \downarrow\uparrow\rangle) \\ T_+ &= |\uparrow\uparrow\rangle & T_- &= |\downarrow\downarrow\rangle \end{aligned} \tag{1.18}$$

The electrons' state will be represented by the product of the orbital and spin state. The singlet spin state is antisymmetric, so it must be in a symmetric orbital state. There are symmetric states with both electrons in the same quantum dot and with the electrons in different quantum dots, so the singlet state. The triplet spin states, however, are symmetric, so they must have an antisymmetric orbital state, which requires the electrons to be in different quantum dots. Due to Pauli exclusion, then, the triplet states cannot be in the same orbital state but the singlet can be. This means that that while the singlet state can inhabit the ground state of the DQD from the Hamiltonian (1.14), the triplet states must cannot be in that hybridized (0,2)-(0,1) state.

The triplet energy can be solved for easily, as it is simply the energy for the (1,1) orbital, $E_T = \epsilon/2$. By turning on a magnetic field, we can separate the energies of the three triplet states, and for the remainder of this thesis we will only consider the T_0 state. The energies of these states as a function

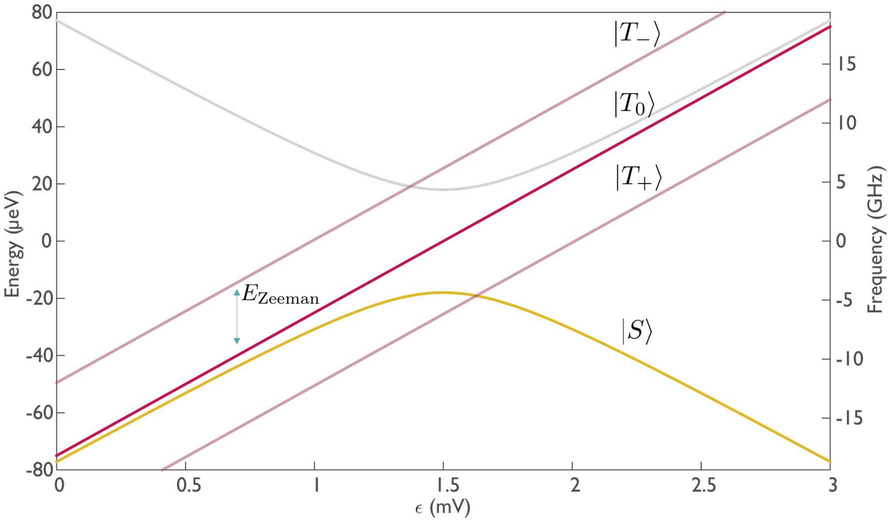

Figure 1.5: Energy diagram for singlet and triplet states. An in plane magnetic field is applied to separate the triplet states by energy E_{Zeeman}. The singlet is in the ground state of the DQD while the triplet states are Pauli-blockaded in (1,1).

of ϵ is shown in Fig. 1.5. We can see from the plot that the energy splitting between the singlet and triplet states can be turned on by shifting ϵ to be positive, so that the singlet has two electrons in the right dot. The gates controlling ϵ are connected to coaxial cable, so the splitting, known as the exchange energy or $J(\epsilon)$, can be turned on or off in nanoseconds. This is the region where the singlet-triplet qubit is 'charge-like' and is useful not only as an axis of control around the Bloch sphere, but also for measurement, loading, and entangling gates [68].

As noted in the Quantum Computing section, for universal control over the quantum state, we need a second axis of control. When ϵ is set so that the qubit is in (1,1) for both states (the left of figure 1.5), exchange is turned off. A magnetic field gradient between the dots as shown in Fig. 1.6**a**, would then split the $|\uparrow\downarrow\rangle$ and $|\downarrow\uparrow\rangle$ states gives the energy $E_{\uparrow\downarrow} = g\mu_B/2(B_L - B_R)$, and flipping the spins changes the sign of the energy. This gives a controllable splitting in the σ_x direction,

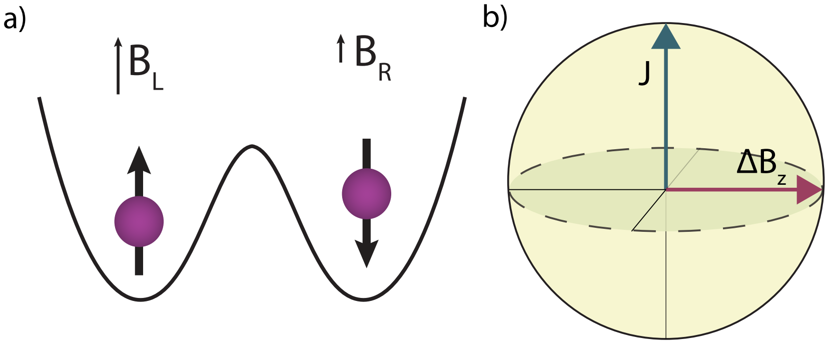

Figure 1.6: a) Cartoon of two quantum dots, each with one electron of opposite spin. The energy is $E = g\mu_B/2(B_L - B_R)$. By flipping the spins we change the sign of the energy. b) Bloch sphere for S-T_0 qubit.

which we define as $\hbar\Delta B_z = g\mu_B(B_L - B_R)$. In the GaAs qubits discussed in this work, the gradient arises from the nuclei in the heterostructure: the nuclei of Al, Ga and As all have nuclear spin $I = 5/2$, which form an Overhauser field that acts on the qubit through hyperfine coupling. This field fluctuates in time, but can be fixed using dynamical nuclear polarization and a feedback method, either one that uses the qubit itself [9] or software feedback, as discussed later in Chapter 4. ΔB_z can be changed over periods of milliseconds, but is considered constant within each set of experiments. In this region of ϵ that the singlet-triplet qubit is effectively a spin qubit, with the states differing only in their spin, and with small voltage pulses not changing the splitting. Of course, the nice thing about the S-T_0 qubit is that we can still use voltage pulses for control; it is simply that in this narrow range of energy that the qubit is voltage-insensitive.

With ΔB_z, we now have control over two different axes, as shown on the Bloch sphere in Fig. 1.6**b**. Gates are performed by changing ϵ, as shown Fig. 1.7. At large ϵ, the total splitting is dominated by the exchange energy. By changing ϵ adiabatically (with respect to the energy splitting from (1.14)), the qubit stays coherent while the splitting changes.

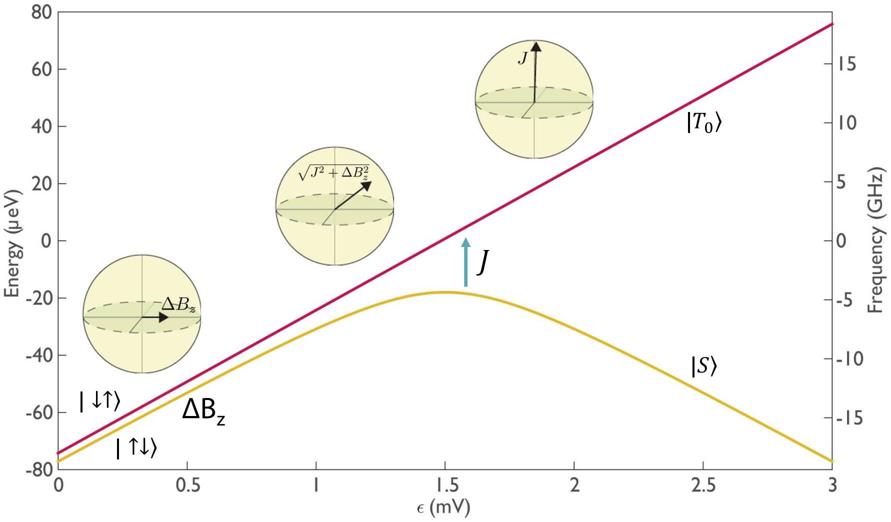

Figure 1.7: Energy diagram for S-T_0 qubit showing regions where $J(\epsilon)$ and ΔB_z are dominant. By changing ϵ, we change the speed and axis of rotation.

There are several remaining ingredients necessary for performing experiments. First is loading the qubits, for which we change the voltages (in this case not just ϵ; we need 2 independent gates) so that the energy of one of the quantum dots is at the Fermi level and so that $|S\rangle$ is the ground state. Then the electrons in the quantum dot can tunnel to the l lead and a $|S\rangle$ state will be loaded. The load time can be tuned from under a nanosecond to microseconds, but we typically set it to a few nanoseconds, which allows fast loading without allowing relaxation when tuned away from the resonance. The other quantum dot is also tunnel coupled to the lead, but much slower to avoid relaxation.

Next, we need to measure the quantum state. A quantum dot fabricated adjacent to the DQD is sensitive to the number of electrons in each dot. By moving to large ϵ, on the graph, we fully localize the singlet state in (0,2), while the triplet remains Pauli-blockaded in (1,1). Then, by measuring the number of electrons in each dot, we can determine if it is a singlet or triplet. To measure states on the x and y-axes, we perform readout pulses after the pulse, either a ΔB_z $\pi/2$ pulse or an adiabatic ramp of ϵ which projects $|\uparrow\downarrow\rangle$ to S and $|\downarrow\uparrow\rangle$ to T_0. The measurement circuit will be discussed further in Chapter 4.

2

Suppressing qubit dephasing using real-time Hamiltonian estimation

Unwanted interaction between a quantum system and its fluctuating environment leads to decoherence and is the primary obstacle to establishing a scalable quantum information processing architecture. Strategies such as environmental and materials engineering, quantum error correction

and dynamical decoupling can mitigate decoherence, but generally increase experimental complexity. Here we improve coherence in a qubit using real-time Hamiltonian parameter estimation. Using a rapidly converging Bayesian approach, we precisely measure the splitting in a singlet-triplet spin qubit faster than the surrounding nuclear bath fluctuates. We continuously adjust qubit control parameters based on this information, thereby improving the inhomogenously broadened coherence time (T_2^*) from tens of nanoseconds to above 2 μs. Because the technique demonstrated here is compatible with arbitrary qubit operations, it is a natural complement to quantum error correction and can be used to improve the performance of a wide variety of qubits in both metrological and quantum-information-processing applications.

2.1 INTRODUCTION

Hamiltonian parameter estimation is a rich field of active experimental and theoretical research that enables precise characterization and control of quantum systems [104]. For example, magnetometry schemes employing Hamiltonian learning have demonstrated dynamic range and sensitivities exceeding those of standard methods [99, 66]. Such applications focused on estimating parameters that are quasistatic on experimental timescales. However, the effectiveness of Hamiltonian learning also offers exciting prospects for estimating fluctuating parameters responsible for decoherence in quantum systems.

The quantum system that we study is a singlet-triplet (S-T_0) qubit [68, 55] which is formed by two gate-defined lateral quantum dots (QDs) in a GaAs/AlGaAs heterostructure (Fig. 2.1**a**), similar to that of refs. [20, 86]. The qubit can be rapidly initialized in the singlet state $|S\rangle$ in $\approx$ 20 ns and read out with 98% fidelity in $\approx 1\ \mu s$ [4, 74] (Supplemenatry Fig. 2). Universal quantum control is provided by two distinct drives [26]: the exchange splitting, J, between $|S\rangle$ and $|T_0\rangle$, and the magnetic field gradient, ΔB_z, due to the hyperfine interaction with host Ga and As nuclei. The Bloch sphere representation for this qubit can be seen in Fig. 2.1**b**. In this work, we focus on qubit evolution around ΔB_z (Fig. 2.2**a**). Due to statistical fluctuations of the nuclei, ΔB_z varies randomly in time, and consequently oscillations around this field gradient decay in a time $T_2^* \approx$ 10 ns [68]. A nuclear feedback scheme relying on dynamic nuclear polarization [9] can be employed to set the mean gradient, ($g^* \mu_B \Delta B_z/h \approx$ 60 MHz in this work) as well as reduce the variance of the fluctuations. Here, $g^* \approx -0.44$ is the effective gyromagnetic ratio in GaAs, μ_B is the Bohr magneton and h is Planck's constant. In what follows, we adopt units where $g^* \mu_B/h = 1$. The nuclear feedback relies on the avoided crossing between the $|S\rangle$ and $|T_+\rangle$ states. When the electrons are brought adiabatically through this crossing, their total spin changes by $\Delta m_s = \pm 1$, which is accompanied by a nuclear spin flip in order to conserve angular momentum. With the use of this feedback, the coherence time improves to $T_2^* \approx$ 100 ns [9] (Fig. 2.2**b**), limited by the low nuclear pumping efficiency [26]. Crucially, the residual fluctuations are considerably slower than the timescale of qubit operations [10].

In this work we employ techniques from Hamiltonian estimation to prolong the coherence of a qubit by more than a factor of 30. Importantly, our estimation protocol, which is based on recent theoretical work [84], requires relatively few measurements ($\approx$100) which we perform rapidly enough (total time $\approx$ 100μs) to resolve the qubit splitting faster than its characteristic fluctuation time. We adopt a paradigm in which we separate experiments into "estimation" and "operation" segments, and we use information from the former to optimize control parameters for the latter in real-time. Our method dramatically prolongs coherence without using complex pulse sequences such as those required for non-identity dynamically decoupled operations [39].

RESULTS

ROTATING FRAME $S - T_0$ QUBIT

To take advantage of the slow nuclear dynamics, we introduce a method that measures the fluctuations and manipulates the qubit based on precise knowledge but not precise control of the environment. We operate the qubit in the rotating frame of ΔB_z, where qubit rotations are driven by modulating J at the frequency $\frac{\Omega_J}{2\pi} = \Delta B_z$ [16, 42]. This is in contrast to traditional modes of opeation of the S-T_0 qubit, which rely on DC voltage pulses. To measure Rabi oscillations, the qubit is adiabatically prepared in the ground state of ΔB_z ($|\psi\rangle$=$|\uparrow\ \downarrow\rangle$), and an oscillating J is switched on (Fig. 2.2**e**), causing the qubit to precess around J in the rotating frame. Additionally, we perform a Ramsey experiment (Fig. 2.2**c**) to determine T_2^*, and as expected, we observe the same decay (Fig. 2.2**d**) as Fig. 2.2**b**. More precisely, the data in Fig. 2.2**d** represent the average of 1024 experimental repetitions of the same qubit operation sequence immediately following nuclear feedback. The feedback cycle resets ΔB_z to its mean value (60 MHz) with residual fluctuations of $(\sqrt{2}\pi T_2^*)^{-1} \approx$ 10MHz between experimental repetitions. However, within a given experimental repetition, ΔB_z is approximately constant. Therefore we present an adaptive control scheme where,

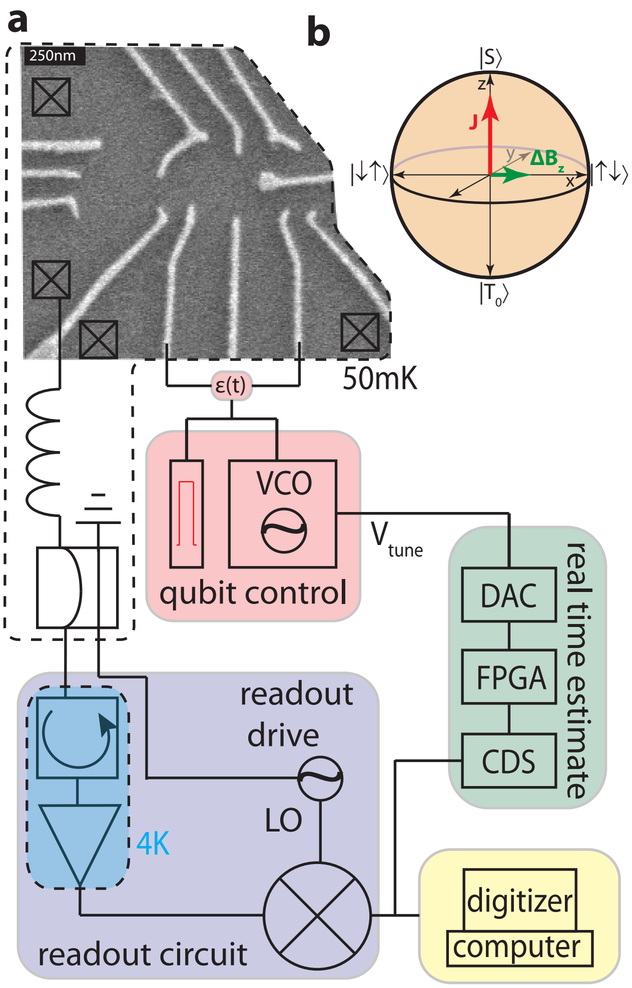

Figure 2.1: Experimental Apparatus. **a,** A scanning electron microscope image of the double QD with a schematic of the apparatus used for adaptive qubit control. A floating metal gate protruding from the right can be seen which increases the capacitance between the qubit and an adjacent qubit (not pictured), which is left inactive for this work. The reflected readout drive signal is demodulated to DC, digitized by a correlated double sampler (CDS), and ΔB_z is estimated in real time by the field programmable gate array (FPGA). The FPGA updates the digital to analog converter (DAC) in order to keep the voltage controlled oscillator (VCO) resonant with the estimated value of ΔB_z. The VCO controls the voltage detuning, $\epsilon(t)$ between the QDs, which, in turn, modulates J at Ω_J. **b,** The Bloch sphere representation for the S-T_0 qubit showing the two axes of control, J and ΔB_z.

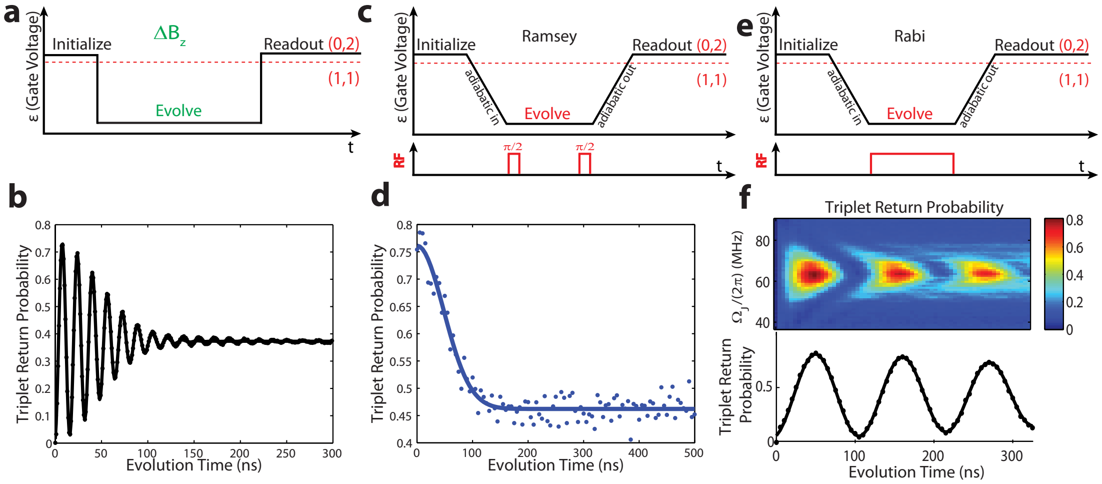

Figure 2.2: ΔB_z oscillations. **a,** The pulse sequence used to estimate ΔB_z. **b,** Using nuclear feedback, ΔB_z oscillations decay in a coherence time $T_2^* = 66$ns due to residual slow fluctuations in ΔB_z. **c,** The Ramsey sequence used to operate the S-T_0 qubit in the rotating frame. **d,** The Ramsey contrast (blue dots) decays in a characteristic time (solid line fit $T_2^* = 68$ns) similarly to the oscillations in **(c)** due to the same residual slow fluctuations in ΔB_z. **e,** The Rabi pulse sequence used to drive the qubit in the rotating frame. **f,** The rotating frame S-T_0 qubit exhibits the typical behavior when sweeping drive frequency and time (top). When driven on resonance (bottom), the qubit undergoes Rabi oscillations, demonstrating control in the rotating frame.

following nuclear feedback, we quickly estimate ΔB_z and tune $\frac{\Omega_J}{2\pi} = \Delta B_z$ in order to prolong qubit coherence (Fig. 2.3**a**).

2.1.1 BAYESIAN ESTIMATION

To estimate ΔB_z, we repeatedly perform a series of singleshot measurements after allowing the qubit to evolve around ΔB_z (using DC pulses) for some amount of time (Fig. 2.2**a**). Rather than fixing this evolution time to be constant for all trials, we make use of recent theoretical results in Hamiltonian parameter estimation [84, 25, 42] and choose linearly increasing evolution times, $t_k = kt_{samp}$, where $k = 1, 2, \cdots, N$. We choose the sampling time t_{samp} such that the estimation

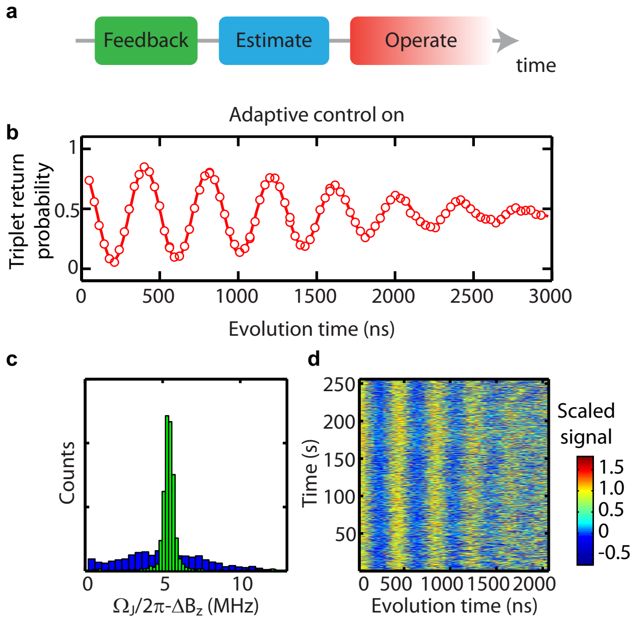

Figure 2.3: Adaptive control. **a,** For these measurements we first perform our standard nuclear feedback, then quickly estimate ΔB_z and update the qubit control, then operate the qubit at the correct driving frequency. **b,** Using adaptive control, we perform a Ramsey experiment (deliberately detuned to see oscillations) and obtain coherence times of $T_2^* = 2066$ ns. **c,** Histograms of measured Ramsey detunings with (green) and without (blue) adaptive control. For clarity, these data were taken with a different mean detuning than those in **(b)**. **d,** Raw data for 1024 consecutive Ramsey experiments with adaptive control lasting 250 s in total. A value of 1 corresponds to $|T_0\rangle$ and 0 corresponds to $|S\rangle$. Stabilized oscillations are clearly visible in the data, demonstrating the effect of adaptive control.

bandwidth $\mathcal{B} = \frac{1}{2t_{samp}}$ is several times larger than the magnitude of the residual fluctuations in ΔB_z, roughly 10 MHz. With a Bayesian approach to estimate ΔB_z in real-time, the longer evolution times (large k) leverage the increased precision obtained from earlier measurements to provide improved sensitivity, allowing the estimate to outperform the standard limit associated with repeating measurements at a single evolution time. Denoting the outcome of the k^{th} measurement as m_k (either $|S\rangle$ or $|T_0\rangle$), we define $P(m_k|\Delta B_z)$ as the conditional probability for m_k given a value

ΔB_z. We write

$$P(m_k|\Delta B_z) = \frac{1}{2}\left[1 + r_k\left(\alpha + \beta\cos\left(2\pi\Delta B_z t_k\right)\right)\right], \tag{2.1}$$

where r_k=1 (-1) for m_k=$|S\rangle$ ($|T_0\rangle$), and $\alpha = 0.25$ and $\beta = 0.67$ are parameters determined by the measurement error and axis of rotation on the Bloch sphere (see Methods2.3). Since we assume that earlier measurement outcomes do not affect later ones (i.e. that there is no measurement back-action), we write the conditional probability for ΔB_z given the results of N measurements as:

$$\begin{aligned} P(\Delta B_z|m_N, m_{N-1}, ...m_1) &= P(\Delta B_z|m_{N-1}, ...m_1) \cdot P(\Delta B_z|m_N) & (2.2)\\ &= \prod_{k=1}^{N} P(\Delta B_z|m_k). & (2.3)\end{aligned}$$

Using Bayes' rule, i.e., $P(\Delta B_z|m_k) = P(m_k|\Delta B_z)P(\Delta B_z)/P(m_k)$, and eq. 2.1, we can rewrite eq. 2.3 as:

$$P(\Delta B_z|m_N, m_{N-1}, ...m_1) = P_0(\Delta B_z)\mathcal{N}\prod_{k=1}^{N}\left(1 + r_k\left(\alpha + \beta\cos\left(2\pi\Delta B_z t_k\right)\right)\right], \tag{2.4}$$

where $\mathcal{N}$ is a normalization constant and $P_0(\Delta B_z)$ is a prior distribution to which the algorithm is empirically insensitive, and which we take to be a constant over the estimation bandwidth. After the last measurement, we find the value of ΔB_z that maximizes the posterior distribution $P(\Delta B_z|m_N, m_{N-1}, ...m_1)$.

2.1.2 Adaptive control

We implement this algorithm in real-time on a field-programmable gate array (FPGA), computing $P(\Delta B_z)$ for 256 values of ΔB_zbetween 50 and 70MHz. With each measurement m_k, the readout signal is digitized and passed to the FPGA, which computes $P(\Delta B_z)$ and updates an analog voltage that tunes the frequency of a voltage controlled oscillator (Fig. 2.1**a**) (Supplementary Note 1). Following the N^{th} sample, $\frac{\Omega_J}{2\pi}$ nearly matches ΔB_z, and since the nuclear dynamics are slow, the qubit can be operated with long coherence without any additional complexity. To quantify how well the FPGA estimate matches ΔB_z, we perform a Ramsey experiment (deliberately detuned to observe oscillations) with this real-time tracking of ΔB_z and find optimal performance for $N \approx 120$, with a maximum experimental repetition rate, limited by the FPGA, of 250kHz and a sampling time $t_{samp} = 12$ ns. Under these conditions, and making a new estimate after every 42 Ramsey experiments, we observe $T_2^* = 2066$ ns, a 30-fold increase in coherence (Fig. 2.3**b**). We note that these data are taken with the same pulse sequence as those in Fig. 2.2**d**. To further compare qubit operations with and without this technique, we measure Ramsey fringes for ≈ 250s (Fig. 2.3**d**), and histogram the observed Ramsey detunings. With adaptive control we observe a stark narrowing of the observed frequency distribution, consistent with this improved coherence (Fig. 2.3**c**).

2.2 Discussion

Although the estimation scheme employed here is theoretically predicted to improve monotonically with N [84], we find that there is an optimum ($N \approx 120$), after which T_2^* slowly decreases with

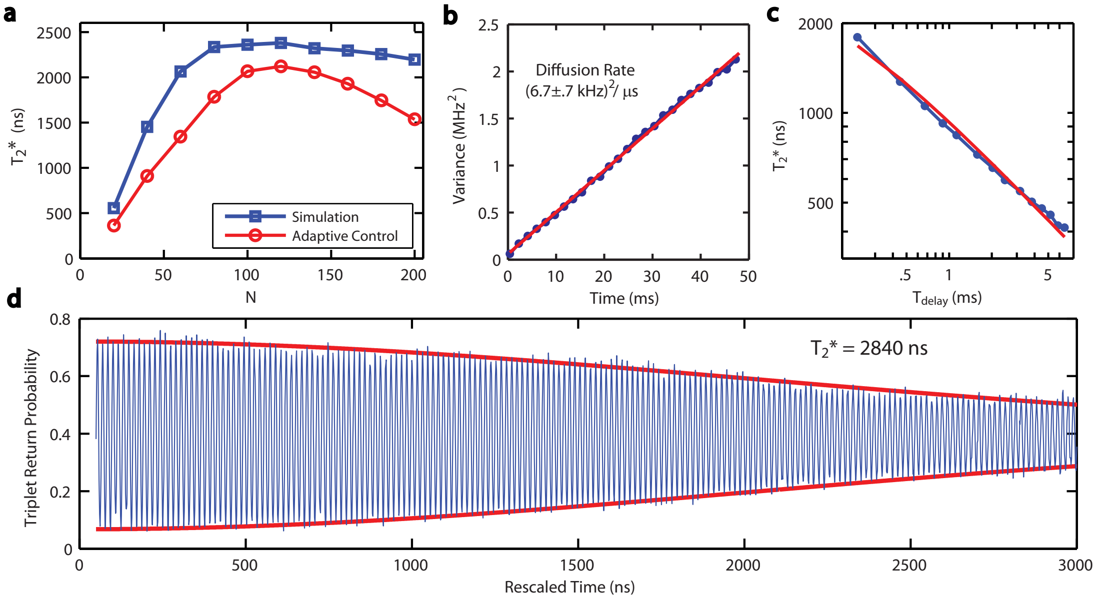

Figure 2.4: ΔB_z diffusion. **a,** The coherence time, T_2^* using the adaptive control and for a simulation show a peak, indicating that there is an optimal number of measurements to make when estimating ΔB_z. **b,** When many time traces of ΔB_z are considered, their variance grows linearly with time, indicating a diffusion process. **c,** The scaling of T_2^* as a function of T_{delay} for software scaled data is consistent with diffusion of ΔB_z. The red line is a fit to a diffusion model. **d,** The performance of the Bayesian estimate of ΔB_z can be estimated using software post processing, giving $T_2^* = 2840$ns, which corresponds to a precision of $\sigma_{\Delta B_z} = 80$kHz.

increasing N (Fig. 2.4**a**). A possible explanation for this trend is fluctuation of the nuclear gradient during the estimation period. To investigate this, we obtain time records of ΔB_z using the Bayesian estimate and find that its variance increases linearly in time at the rate of $(6.7 \pm .7\text{kHz})^2 \mu s^{-1}$ (Fig. 2.4**c**). The observed linear behavior suggests a model where the nuclear gradient diffuses, which can arise, for example, from dipolar coupling between adjacent nuclei. Using the measured diffusion of ΔB_z, we simulate the performance of the Bayesian estimate as a function of N(see Methods2.3.1). Given that the simulation has no free parameters, we find good agreement with the observed T_2^*, indicating that indeed, diffusion limits the accuracy with which we can measure ΔB_z (Fig. 2.4**a**).

This model suggests that increasing the rate of measurements during estimation will improve the accuracy of the Bayesian estimate. Because our FPGA limits the repetition rate of qubit operations to 250 kHz, we demonstrate the effect of faster measurements through software post-processing with the same Bayesian estimate. To do so, we first use the same estimation sequence, but for the operation segment, we measure the outcome after evolving around ΔB_z for a single evolution time, t_{evo}, rather than performing a rotating frame Ramsey experiment, and we repeat this experiment a total of N_{tot} times. In processing, we perform the Bayesian estimate of each $\Delta B_{z,i}$, sort the data by adjusted time $\tau_i = \frac{\Delta B_{z,i} t_{evo,i}}{\langle \Delta B_z \rangle}$ (for $i = 1, 2, \cdots, N_{tot}$), and average together points of similar τ in order to observe oscillations (see Methods 2.3.2). We fit the decay of these oscillations to extract T_2^* and the precision of the Bayesian estimate, $\sigma_{\Delta B_z} = \left(\sqrt{2}\pi T_2^*\right)^{-1}$. For the same operation and estimation parameters, we find that T_2^* extracted from software post-processing agrees with that extracted from adaptive control (Fig. 2.4**a**). Using a repetition rate as high as 667kHz, we show coherence times above 2800 ns, corresponding to an error of $\sigma_{\Delta B_z}$=80kHz (Fig. 2.4**d**), indicating that improvements are easily attainable by using faster (commercially available) FPGAs.

Additionally, we use this post-processing to examine the effect of this technique on the duty cycle of experiments as well as the stability of the ΔB_z estimate. To do so we introduce a delay T_{delay} between the estimation of ΔB_z and the single evolution measurement performed in place of the operation. We find $T_2^* = (a + bT_{\text{delay}}^c)^{-0.5}$, where c = 0.99 (Fig. 2.4**c**), consistent with diffusion of ΔB_z. Indeed, this dependence underscores the potential of adaptive control, since it demonstrates that after a single estimation sequence, the qubit can be operated for $>$ 1ms with $T_2^* >$ 1μs. Thus, adaptive control need not significantly reduce the experimental duty cycle.

In this work, we have used real-time adaptive control based on Hamiltonian parameter estimation of a $S-T_0$ spin qubit to prolong T_2^* from 70ns to more than 2 μs. Dephasing due to nuclear spins has long been considered a significant obstacle to quantum information processing using semiconductor spin qubits [82], and elimination of nuclear spins is an active and fruitful area of research [3, 103, 62]. However, here we have shown that with a combination of nuclear feedback, rotating frame S-T_0 spin resonance, and real-time Hamiltonian estimation, we are able to achieve ratios of coherence times to operation times in excess of 200 without recourse to dynamical decoupling [32, 93, 10]. If the same adaptive control techniques were applied to gradients as high as 1 GHz [26], ratios exceeding 4000 would be possible, and longer coherence times may be attainable with more sophisticated techniques [84]. Though the observed coherence times are still smaller than the Hahn echo time, T_2^{echo} [10], the method we have presented is straightforward to implement, compatible with arbitrary qubit operations, and general to all qubits that suffer from non-Markovian noise. Looking ahead, it is likely, therefore, to play a key role in realistic quantum error correction efforts [65, 72, 100, 90], where even modest improvements in baseline error rate greatly diminish experimental complexity and enhance prospects for a scalable quantum information processing architecture.

2.3 METHODS

BAYESIAN ESTIMATE

We wish to calculate the probability that the nuclear magnetic field gradient has a certain value, ΔB_z, given a particular measurement record comprising N measurements. We follow the technique in Sergeevich *et. al.*[84] with slight modifications. Writing the outcome of the k^{th} measurement as m_k, we write this probability distribution as

$$P\left(\Delta B_z|m_N, m_{N-1}, ...m_1\right). \tag{2.5}$$

To arrive at an expression for this distribution, we will write down a model for the dynamics of the system, i.e. $P\left(m_N, m_{N-1}, ...m_1|\Delta B_z\right)$. Using Bayes' rule we can relate the two equations as

$$P\left(\Delta B_z|m_N, m_{N-1}, ...m_1\right) \cdot P\left(m_N, m_{N-1}, ...m_1\right) \tag{2.6}$$

$$= P\left(m_N, m_{N-1}, ...m_1|\Delta B_z\right) \cdot P\left(\Delta B_z\right). \tag{2.7}$$

First, we seek a model that can quantify $P\left(m_N, m_{N-1}, ...m_1|\Delta B_z\right)$ that accounts for realistic errors in the system, namely measurement error, imperfect state preparation, and error in the axis of rotation around the Bloch sphere. For simplicity, we begin with a model that accounts only for measurement error. Denoting the error associated with measuring a $|S\rangle$ ($|T_0\rangle$) as η_S (η_T), we write

$$P\left(S|\Delta B_z\right) = \left(1-\eta_S\right)\cos^2\left(2\pi\Delta B_z t_k/2\right) + \ \eta_T \sin^2\left(2\pi\Delta B_z t_k/2\right) \tag{2.8}$$

$$P\left(T_0|\Delta B_z\right) = \left(1-\eta_T\right)\sin^2\left(2\pi\Delta B_z t_k/2\right) + \eta_S\cos^2\left(2\pi\Delta B_z t_k/2\right) \tag{2.9}$$

We combine these two equations and write

$$P\left(m_k|\Delta B_z\right) = \frac{1}{2}\left[1 + r_k\left(\alpha + \beta\cos\left(2\pi\Delta B_z t_k\right)\right)\right] \tag{2.10}$$

where r_k=1 (-1) for $m_k = |S\rangle(|T_0\rangle)$ and α and β are given by

$$\alpha = \left(\eta_T - \eta_S\right), \quad \beta = \left(1-\eta_S-\eta_T\right). \tag{2.11}$$

Next, we generalize the model to include the effects of imperfect state preparation, and the presence of nonzero J during evolution, which renders the initial state non-orthogonal to the axis of rotation around the Bloch sphere (see above). We assume that the angle of rotation around the Bloch sphere lies somewhere in the x-z plane and makes an angle θ with the z-axis. We define $\delta = \cos^2(\theta)$. Next, we include imperfect state preparation by writing the density matrix $\rho_{init} = (1-\epsilon)\,|S\rangle\,\langle S|) + \epsilon\,|T_0\rangle\,\langle T_0|$. With this in hand, we can write down the model

$$P\left(S|\Delta B_z\right) = \eta_T + \frac{1}{2}(1-\eta_S-\eta_T)\left\{1 + (1-2\epsilon)\left[\delta\ + (1-\delta)\cos\ (2\pi\Delta B_z t_k)\right]\right\}, \tag{2.12}$$

$$P\left(T_0|\Delta B_z\right) = \eta_S + \frac{1}{2}(1-\eta_S-\eta_T)\left\{1-(1-2\epsilon)\left[\delta\ +(1-\delta)\cos\ (2\pi\Delta B_z t_k)\right]\right\}. \quad (2.13)$$

Using the same notation for r_k=1 (-1) for $m_k = |S\rangle(|T_0\rangle)$, we rewrite this in one equation as

$$P\left(m_k|\Delta B_z\right) = \frac{1}{2}\left[1 + r_k\left(\alpha + \beta\cos\left(2\pi\Delta B_z t_k\right)\right)\right], \quad (2.14)$$

where we now have

$$\alpha = \eta_T - \eta_S + (1-\eta_S-\eta_T)(\delta - 2\epsilon\delta) \quad (2.15)$$

$$\beta = (1-\eta_S-\eta_T)(1-\delta)(1-2\epsilon). \quad (2.16)$$

We find the best performance for $\alpha = 0.25$ and $\beta = 0.67$, which is consistent with known values for qubit errors.

We next turn our attention to implementing Bayes' rule to turn this model into a probability distribution for ΔB_z. First, we assume that all measurements are statistically independent, allowing us to write

$$\begin{aligned} P\left(\Delta B_z|m_N, m_{N-1}, ...m_1\right) &= P\left(\Delta B_z|m_N\right)\cdot\ P\left(\Delta B_z|m_{N-1}, ...m_1\right) \\ &= \prod_{k=1}^{N} P\left(\Delta B_z|m_k\right). \end{aligned} \quad (2.17)$$

We next use Bayes rule (2.7) and rewrite this equation as

$$P\left(\Delta B_z | m_N, m_{N-1}, ...m_1\right) = \prod_{k=1}^{N} P\left(m_k | \Delta B_z\right) \frac{P(\Delta B_z)}{P(m_k)}. \tag{2.18}$$

Using our model (2.14) we can rewrite this as

$$P\left(\Delta B_z | m_N, m_{N-1}, ...m_1\right) = \mathcal{N} P_0(\Delta B_z) \prod_{k=1}^{N} \left[1 + r_k \left(\alpha + \beta \cos\ \left(2\pi \Delta B_z t_k\right)\right)\right], \tag{2.19}$$

where $\mathcal{N}$ is a normalization constant, and $P_0(\Delta B_z)$ is a prior distribution for ΔB_z which we take to be a constant over the estimation bandwidth, and to which the estimator is empirically insensitive. With this formula, it is simple to see that the posterior distribution for ΔB_z can be updated in real time with each successive measurement. After the N^{th} measurement, we choose the value for ΔB_z which maximizes the posterior distribution (2.19).

2.3.1 Simulation with diffusion

We simulate the performance of our software scaling and hardware (FPGA) estimates of ΔB_z using the measured value of the diffusion rate. We assume that ΔB_z obeys a random walk, but assume that during a single evolution time t_k, ΔB_z is static. This assumption is valid when $\sqrt{t_N \mathcal{D}} T_2^* \ll 1$, where $\mathcal{D}$ is the diffusion rate of ΔB_z. For an estimation of ΔB_z with N different measurements, we generate a random walk of N different values for ΔB_z (using the measured diffusion), simulate the outcome of each measurement, and compute the Bayesian estimate of ΔB_z using the simulated outcomes. By repeating this procedure 4096 times, and using the mean squared error, MSE $= \langle \left(\Delta B_z - \Delta B_z{}^{estimated} \right)^2 \rangle$ as a metric for performance, we can find the optimal number of measurements to perform. To include the entire error budget of the FPGA apparatus, we add to this MSE the error from the phase noise of the VCO, the measured voltage noise on the analog output controlling the VCO, and the diffusion of ΔB_z during the "operation" period of the experiment.

2.3.2 SOFTWARE POST PROCESSING

The estimate of ΔB_z can be independently verified using software analysis. In this experiment, we use the same method to estimate ΔB_z as in the adaptive control experiment, but in the operation segment perform oscillations around ΔB_z for verification. We choose m different evolution times and measure each n times for a total of $N_{tot} = m \times n$ measurements of ΔB_z. In the i^{th} experiment ($i = 1, 2, \ldots N_{tot}$), we evolve for a time $t_{evo,i}$, accumulating phase $\phi_i = \Delta B_{z,i} t_{evo,i}$. Because we make a precise measurement of ΔB_z at the start of each experiment, we can employ it to rescale the time, $t_{evo,i}$, so that the phase accumulated for a given time is constant using the equation,

$$\tau_i \equiv t_{evo,i} \frac{\Delta B_{z,i}}{\langle \Delta B_z \rangle}$$

This sets $\phi_i(\tau_i) = \langle \Delta B_z \rangle \tau_i$, with residual error arising from inaccuracy in the estimate of $\Delta B_{z,i}$. The data are then sorted by τ, and points of similar τ are averaged using a Gaussian window with $\sigma_\tau = 0.5$ ns $\ll T \approx 16$ ns, where T is the period of the oscillations.

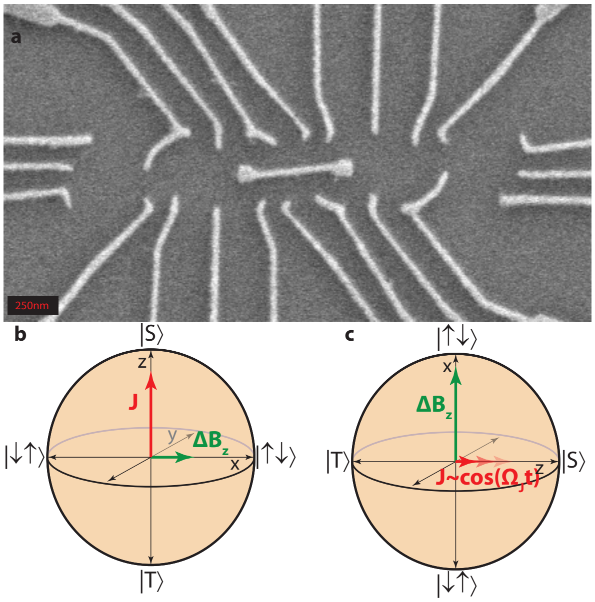

Figure 2.5: **a**. An electron microscope image of the device used. Two qubits each comprising a double quantum dot and an additional quantum dot for charge sensing are fabricated in close proximity. A floating metal gate is fabricated between the qubits to increase the inter-qubit capacitance. The right qubit is left inactive for this work. **b**. The Bloch sphere representation for the S-T_0 qubit. **c**. The Bloch sphere representation for the S-T_0 qubit in the rotating frame, where rotations are driven my modulating J.

2.4 The device

The work presented here was performed on a two-qubit device with one qubit left inactive. An SEM microcgraph can be seen in Fig. 2.1**a**. We operate the S-T_0 qubit in two different ways: static operation with DC pulses (Fig. 2.1**b**) and the new, rotating frame, resonant operation with RF pulses (Fig. 2.5**c**).

2.5 Singleshot Sensor Response

In order to effectively sample ΔB_z oscillations without having to measure each evolution time t_k more than once, we rely on high fidelity readout, which is based on standard RF-reflectometry techniques [74, 4]. The readout fidelity is routinely better than 0.98. Though the Bayesian estimate of ΔB_z has parameters to account for readout error (see below), it nevertheless requires that this error be small. Moreover, in order to effectively process and compare data with both the FPGA and with software rescaling, we must achieve high fidelity readout with both the data acquisition card (DAQ) and with the FPGA. Fig. 2.6**a** shows histograms of all of the measured values. The double-peaked structure indicates that, indeed, high fidelity readout is achieved with both the DAQ and the FPGA. The difference in the heights of the two peaks is caused by residual exchange (J) during evolution, which causes the axis of evolution around the Bloch sphere to be non-orthogonal to the initial state (see section 2.3). For the Bayesian estimate, which requires discretized data ($r_k = \pm 1$), we choose a threshold corresponding to the minimum between the peaks for the adaptive control on the FPGA.

2.6 FPGA and experimental apparatus

The reflected readout drive signal returns to room temperature through a cryogenic circulator and amplifier at 4K. The signal is amplified again at room temperature before being demodulated to DC. This DC signal is split and sent to a digitizing card (AlazarTech 660) in a computer and a home built correlated double sampler (CDS). The CDS digitizes the signal and performs a local reference subtraction to reject low frequency noise. The resulting 16 bit signal is converted to a low voltage digital

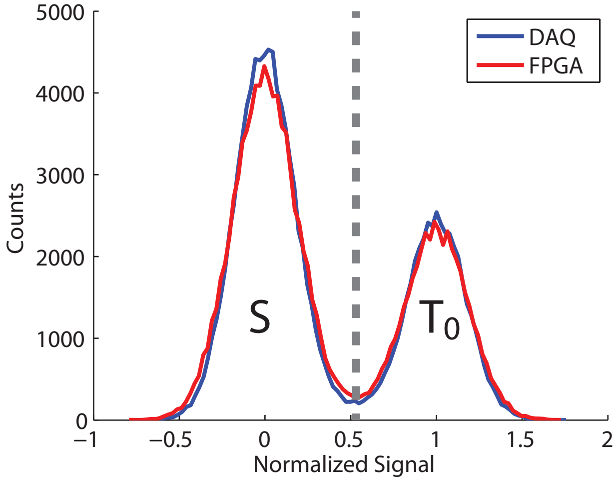

Figure 2.6: a. A histogram of values measured by the data acquisition card (DAQ) and the FPGA/CDS show nearly identical double peaked structures, indicating that they are capable of consistent singleshot readout. The dashed line is chosen as the threshold for estimating ΔB_z with the FPGA.

signal and sent to the FPGA for processing. The FPGA is a National Instruments model PXI-7841R and is clocked at 40MHz to maximize processing speed. The probability $P(\Delta B_z|m_k)$ is computed for 256 consecutive frequencies in the estimation bandwidth, $\mathcal{B}$, in two parallel processes on the FPGA to decrease calculation time. Since $\mathcal{B} \approx$ 40MHz is larger than the residual fluctuations of ΔB_z, we increase the frequency resolution by computing the Bayesian estimate of ΔB_z for the the middle 256 frequencies inside of $\mathcal{B}$. For these parameters, the minimum calculation time is $3.7\mu s$ for a single t_k. The probability distributions are stored and updated as single-precision floating-point numbers, since we find that single-precision improves the accuracy of the estimator over fixed-point numbers.

After estimating ΔB_z, the FPGA returns the index (an integer between 1 and 256) of the most probable frequency, which must be converted to a voltage to control the VCO. To do so, we apply a

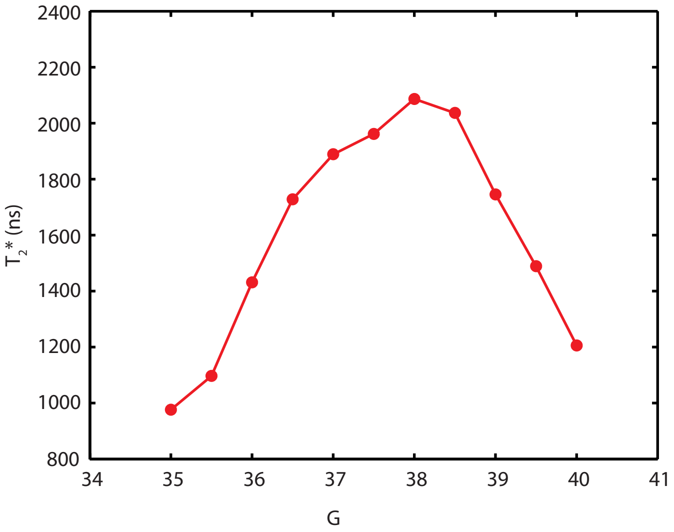

Figure 2.7: a. T_2^* changes with the gain, G, converting a frequency index into a control voltage for the VCO. This allows for the optimal gain to be found.

linear transformation to the index, $V = G \times index + O$, where the O controls the detuning of the driving frequency. We tune the G to maximize T_2^* using adaptive control (Fig. 2.7**a**).

2.7 BAYESIAN ESTIMATE

We wish to calculate the probability that the nuclear magnetic field gradient has a certain value, ΔB_z, given a particular measurement record comprising N measurements. We follow the technique in Sergeevich *et. al.*[84] with slight modifications. Writing the outcome of the k^{th} measurement as m_k, we write this probability distribution as

$$P\left(\Delta B_z | m_N, m_{N-1}, ...m_1\right). \tag{2.20}$$

To arrive at an expression for this distribution, we will write down a model for the dynamics of the system, i.e. $P\left(m_N, m_{N-1}, ...m_1|\Delta B_z\right)$. Using Bayes' rule we can relate the two equations as First, we seek a model that can quantify $P\left(m_N, m_{N-1}, ...m_1|\Delta B_z\right)$ that accounts for realistic errors in the system, namely measurement error, imperfect state preparation, and error in the axis of rotation around the Bloch sphere. For simplicity, we begin with a model that accounts only for measurment error. Denoting the error associated with measuring a $|S\rangle$ ($|T_0\rangle$) as η_S (η_T), we write

$$P\left(S|\Delta B_z\right) = \left(1-\eta_S\right)\cos^2\left(2\pi\Delta B_z t_k/2\right) + \eta_T \sin^2\left(2\pi\Delta B_z t_k/2\right) \tag{2.21}$$

$$P\left(T_0|\Delta B_z\right) = \left(1-\eta_T\right)\sin^2\left(2\pi\Delta B_z t_k/2\right) + \eta_S \cos^2\left(2\pi\Delta B_z t_k/2\right) \tag{2.22}$$

We combine these two equations and write

$$P\left(m_k|\Delta B_z\right) = \frac{1}{2}\left[1 + r_k\left(\alpha + \beta\cos\left(2\pi\Delta B_z t_k\right)\right)\right] \tag{2.23}$$

where r_k=1 (-1) for $m_k = |S\rangle(|T_0\rangle)$ and α and β are given by

$$\alpha = \left(\eta_T - \eta_S\right), \quad \beta = \left(1-\eta_S-\eta_T\right). \tag{2.24}$$

Next, we generalize the model to include the effects of imperfect state preparation, and the presence of nonzero J during evolution, which renders the initial state non-orthogonal to the axis of rotation around the Bloch sphere (see above). We assume that the angle of rotation around the Bloch sphere lies somewhere in the x-z plane and makes an angle θ with the z-axis. We define $\delta = \cos^2(\theta)$. Next, we include imperfect state preparation by writing the density matrix $\rho_{init} = (1-\epsilon)\left|S\right\rangle\left\langle S\right|) + \epsilon\left|T_0\right\rangle\left\langle T_0\right|$. With this in hand, we can write down the model

$$P\left(S|\Delta B_z\right) = \eta_T + \frac{1}{2}(1-\eta_S-\eta_T)\left\{1+(1-2\epsilon)\left[\delta+(1-\delta)\cos\left(2\pi\Delta B_z t_k\right)\right]\right\}, \quad (2.25)$$

$$P\left(T_0|\Delta B_z\right) = \eta_S + \frac{1}{2}(1-\eta_S-\eta_T)\left\{1-(1-2\epsilon)\left[\delta+(1-\delta)\cos\left(2\pi\Delta B_z t_k\right)\right]\right\}. \quad (2.26)$$

Using the same notation for r_k=1 (-1) for $m_k = |S\rangle(|T_0\rangle)$, we rewrite this in one equation as

$$P\left(m_k|\Delta B_z\right) = \frac{1}{2}\left[1+r_k\left(\alpha+\beta\cos\left(2\pi\Delta B_z t_k\right)\right)\right], \quad (2.27)$$

where we now have

$$\alpha = \eta_T - \eta_S + (1-\eta_S-\eta_T)(\delta-2\epsilon\delta) \quad (2.28)$$

$$\beta = (1-\eta_S-\eta_T)(1-\delta)(1-2\epsilon). \quad (2.29)$$

We find the best performance for $\alpha = 0.25$ and $\beta = 0.67$, which is consistent with known values for qubit errors.

We next turn our attention to implementing Bayes' rule to turn this model into a probability distribution for ΔB_z. First, we assume that all measurements are independent, allowing us to write

$$\begin{aligned} P\left(\Delta B_z | m_N, m_{N-1}, ...m_1\right) &= P\left(\Delta B_z | m_N\right) \cdot P\left(\Delta B_z | m_{N-1}, ...m_1\right) \\ &= \prod_{k=1}^{N} P\left(\Delta B_z | m_k\right). \end{aligned} \tag{2.30}$$

We next use Bayes rule (2.7) and rewrite this equation as

$$P\left(\Delta B_z | m_N, m_{N-1}, ...m_1\right) = \prod_{k=1}^{N} P\left(m_k | \Delta B_z\right) \frac{P(\Delta B_z)}{P(m_k)}. \tag{2.31}$$

Using our model (2.27) we can rewrite this as

$$P\left(\Delta B_z | m_N, m_{N-1}, ...m_1\right) = \mathcal{N} P_0(\Delta B_z) \prod_{k=1}^{N} \left[1 + r_k\left(\alpha + \beta \cos\left(2\pi \Delta B_z t_k\right)\right)\right], \tag{2.32}$$

where $\mathcal{N}$ is a normalization constant, and $P_0(\Delta B_z)$ is a prior distribution for ΔB_z which we take to be a constant over the estimation bandwidth, and to which the estimator is empirically insensitive. With this formula, it is simple to see that the posterior distribution for ΔB_z can be updated in real time with each successive measurement. After the N^{th} measurement, we choose the value for ΔB_z which maximizes the posterior distribution (2.32).

2.8 Simulation with diffusion

We simulate the performance of our software scaling and hardware (FPGA) estimates of ΔB_z using the measured value of the diffusion rate. We assume that ΔB_z obeys a random walk, but assume that during a single evolution time t_k, ΔB_z is static. This assumption is valid $\sqrt{t_N \mathcal{D}} T_2^* \ll 1$, where $\mathcal{D}$ is the diffusion rate of ΔB_z. For an estimation of ΔB_z with N different measurements, we generate a random walk of N different values for ΔB_z (using the measured diffusion), simulate the outcome of each measurement, and compute the Bayesian estimate of ΔB_z using the simulated outcomes. By repeating this procedure 4096 times, and using the mean squared error, MSE $= \langle \left(\Delta B_z - \Delta B_z{}^{estimated}\right)^2 \rangle$ as a metric for performance, we can find the optimal number of measurements to perform. To include the entire error budget of the FPGA apparatus, we add to this MSE the error from the phase noise of the VCO, the measured voltage noise on the analog output controlling the VCO, and the diffusion of ΔB_z during the "operation" period of the experiment.

2.9 Software Post Processing

The estimate of ΔB_z can be independently verified using software analysis. In this experiment, we use the same method to estimate ΔB_z as in the adaptive control experiment, but in the operation segment perform oscillations around ΔB_z for verification. We choose m different evolution times and measure each n times for a total of $N_{tot} = m \times n$ measurements of ΔB_z. In the i^{th} experiment ($i = 1, 2, \ldots N_{tot}$), we evolve for a time $t_{evo,i}$, accumulating phase $\phi_i = \Delta B_{z,i} t_{evo,i}$. Because we

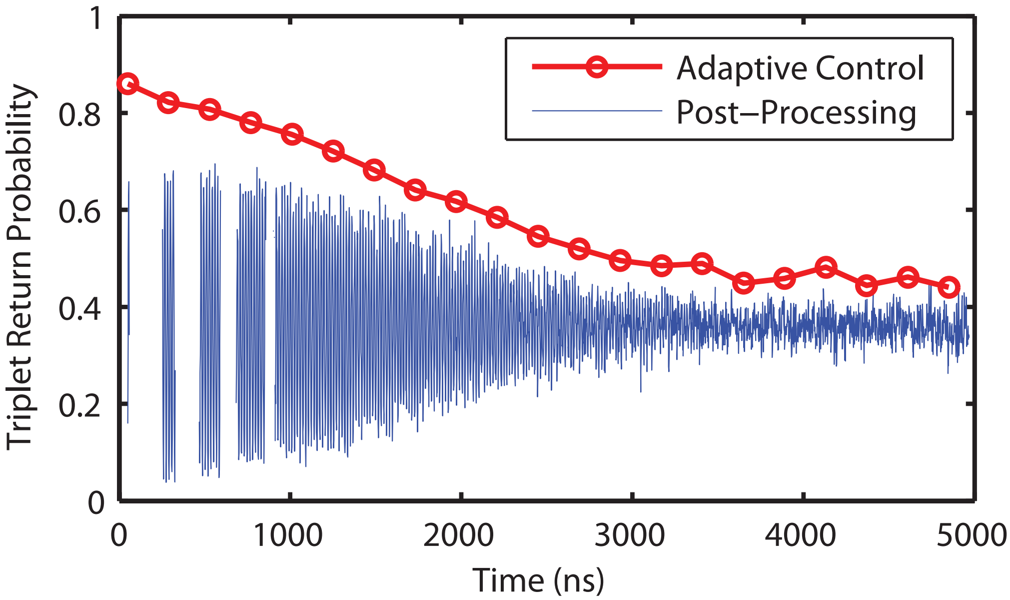

Figure 2.8: a. When using the same estimation sequence, post-processed oscillations (blue) and data taken using adaptive control (red) show the same decay, indicating similar performance of the estimation. The post-processing technique allows us to explore estimation sequences that are too fast for the FPGA.

make a precise measurement of ΔB_z at the start of each experiment, we can employ it to rescale the time, $t_{evo,i}$, so that the phase accumulated for a given time is constant using the equation,

$$\tau_i \equiv t_{evo,i}\frac{\Delta B_{z,i}}{\langle \Delta B_z \rangle}$$

This sets $\phi_i(\tau_i) = \langle \Delta B_z \rangle \tau_i$, with residual error arising from inaccuracy in the estimate of $\Delta B_{z,i}$. The data are then sorted by τ, and points of similar τ are averaged using a Gaussian window with $\sigma_\tau = 0.5$ ns $\ll T \approx 16$ ns, where T is the period of the oscillations.

To compare post-processing with adaptive control, we first perform the same estimation sequence for both software post-processing and adaptive control, with a 250 kHz repetition rate,

$t_{samp} = 12$ ns and N =120, followed by an operation sequence of 30 measurements. We find $T_2^* = 2148 \pm 30$ ns with software and $T_2^* = 2066$ ns with adaptive control, showing good agreement between the two approaches (Fig. 2.8**a**).

For the software post-processing, we can reduce the amount of diffusion that occurs during the operation sequence by performing only one verification measurement following the same estimation sequence, enhancing T_2^*, to 2580 ± 40 ns. For the software rescaling in Fig. 4d, the 109 estimations were performed in 225 μs instead of the 440 μs used by the FPGA, yielding $T_2^* = 2840 \pm 30$ ns. This is likely limited by diffusion and the precision of the estimator with N=109.

3

Coupling Two Spin Qubits with a High-Impedance Resonator

Fast, high-fidelity single and two-qubit gates are essential to building a viable quantum information processor, but achieving both in the same system has proved challenging for spin qubits. We propose and analyze an approach to perform a long-distance two-qubit controlled phase (CPHASE) gate between two singlet-triplet qubits using an electromagnetic resonator to mediate their interaction. The qubits couple longitudinally to the resonator, and by driving the qubits near the resonator's frequency they can be made to acquire a state-dependent geometric phase that leads to a CPHASE gate independent of the initial state of the resonator. Using high impedance resonators enables gate times of order 10 ns while maintaining long coherence times. Simulations show average gate fidelities of over 96% using currently achievable experimental parameters and over 99% using state-of-the-art resonator technology. After optimizing the gate fidelity in terms of parameters tuneable in-situ, we find it takes a simple power-law form in terms of the resonator's impedance and quality and the qubits' noise bath.

3.1 Introduction

Spin qubits with gateable charge-like states have many desirable features for quantum computing, and have been pursued through a range of qubit implementations including singlet-triplet (S-T_0) and hybrid qubits in a double quantum dot (DQD) as well as exchange-only qubits in triple dots[67, 105, 23, 41, 57]. Coupling to charge speeds up many crucial operations, including single and two-qubit operations and measurement, compared with a solely magnetic control, but they retain coherence times that are orders of magnitude above those of pure charge qubits. For instance, implementations of S-T_0 qubits in GaAs boast $> 98\%$ fidelity single gate operations up to several GHz as well as 98% measurement fidelity in 1 μs[14, 63, 86]. However, the spin-like nature of these qubits typically leads two-qubit gates to be much slower than single-qubit gates and to have speeds that fall off sharply with distance, making scaling to more than two qubits challenging[86]. One way to remedy both of these issues is to couple two distant qubits using a resonator[98, 60, 81, 44]. We consider electric coupling between the resonator field and a charge-like state of a spin qubit, focusing on the S-T_0 qubit, although we note that it is possible to use any of the spin qubits with gateable charge-like states.

The S-T_0 qubit's logical subspace consists of the hyperfine-degenerate singlet and triplet states of two electrons in a tunnel coupled DQD. While electrons in the singlet state are hybridized between the two dots in the ground state, with a distribution determined by the dots' relative energies and their tunnel coupling, the electrons in the triplet state are Pauli-blockaded with one electron in each dot. The S-T_0 energy splitting, J, is thus controlled by the difference in chemical potentials of the two dots, ϵ, which can be tuned by proximal RF gates on nanosecond timescales. A magnetic field gradient between the dots drives rotations around σ_x, but will be neglected for the remainder.

The qubit's electric dipole operator is diagonal in the energy basis, so the qubit-resonator coupling is a longitudinal interaction, as has been investigated in Refs. [8, 37, 83, 7, 21, 76, 79]. The resulting gate that we describe in this paper has a number of advantages over transverse-coupled gates. It is not necessary to bring the qubits into resonance with one another or the resonator, making the gate quite simple; it relies on applying a single tone near the resonator's frequency to each of the qubits, with no direct control of the resonator required. Moreover, this makes it compatible with remaining at sweet spots for enhanced dephasing time. The gate speed is a linear function of the drive, so it can be turned completely off and does not require high powers for fast gates. Furthermore, there is no Purcell effect and no dispersive approximation is necessary, so the drive frequency can be near the resonator's frequency and the drive amplitude is unconstrained, enabling faster gates. Another advantage is that the gate is independent of the resonator's initial state, and only depends on its dynamics (e.g., its decay rate). As a result, cross-talk to the resonator and elevated temperatures are not barriers to implementing the gate, as noted in [83].

3.2 GEOMETRIC PHASE GATE

We begin by outlining the essential physics underlying the two-qubit gate. By driving ϵ of the first qubit near the resonator's frequency, we cause electrons in the singlet state to oscillate between the two quantum dots while electrons in the triplet state remain stationary due to Pauli blockade. The resonator is thereby excited in a qubit-state-dependent manner, which in turn acts to drive ϵ in the far qubit. When the two qubits are driven at the same frequency, the interaction with the resonator has a non-zero average, and the qubits accrue a resonator-dependent geometric phase that lets us perform a CPHASE gate. We can now consider the main noise processes of this interaction. Driving the qubits closer to the resonator's frequency excites the resonator more, which makes the gate faster, but causes more photons to be lost from the resonator. For similar coupling mechanisms in other systems with a far larger resonator decay rate than qubit dephasing rate, fidelity can be optimized by driving at a frequency that equalizes dephasing through the qubits and the resonator[22, 28, 83]. However, in the case of an S-T_0 qubit coupled to a superconducting resonator, the resonator decay rate is comparable to the qubit dephasing rate. In this regime of large qubit dephasing, noise from the resonator is relatively unimportant, and it is essential to perform the gate as fast as possible. The

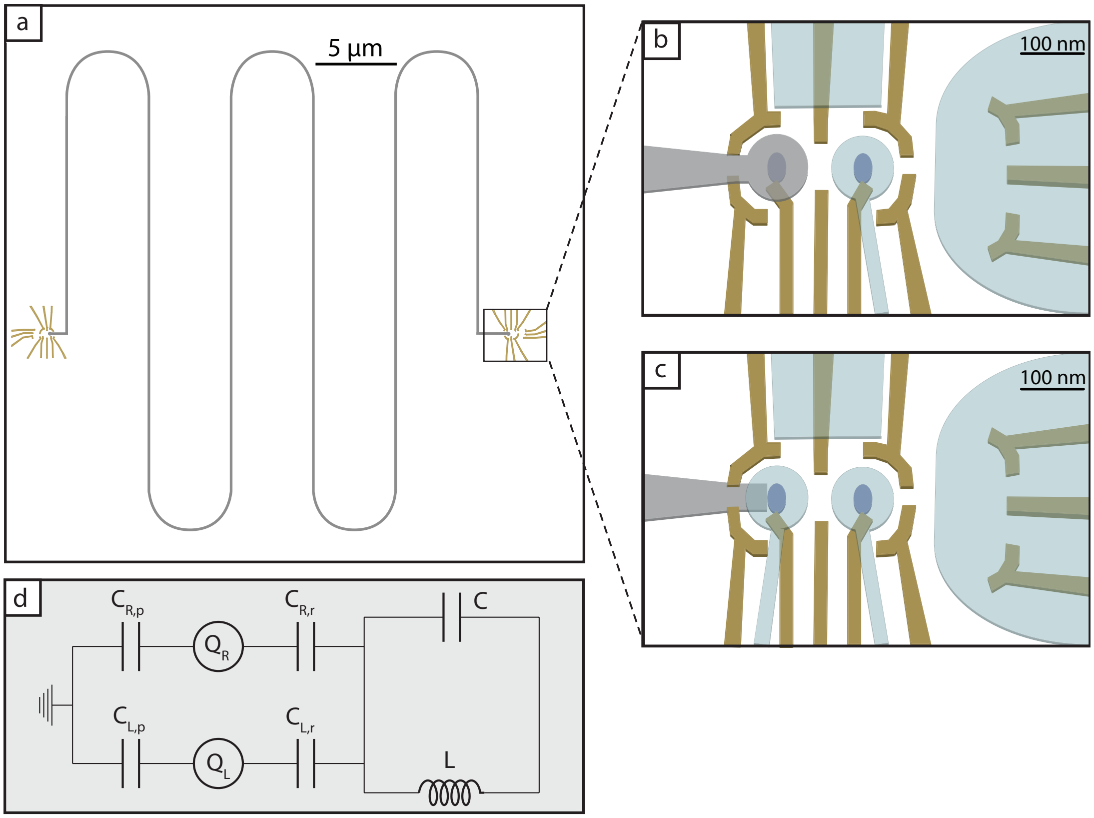

Figure 3.1: **a**, Schematic of the two-qubit-resonator device. A double quantum dot is placed at either end of a high-impedance resonator. A nanowire resonator is shown, but other types have similar dimensions; the resonator can be further meandered to reduce its footprint, or straightened to transport information over larger distances. **b-c**, Proposed designs for Si-SiGe quantum-dot-resonator devices. Accumulation gates are shaded pale blue, depletion gates gold, and the resonator gray. In **b**, the resonator replaces one of the accumulation gates, so it is separated by an additional 50 nm oxide, $c_r = 0.02$. In **c**, the resonator is at the depletion gates layer, $c_r = 0.25$. **d**, A circuit schematic of a qubit resonator system (the left qubit is not shown, but is identical to the right qubit). The left and right quantum dots, Q_L and Q_R, have capacitance $C_{i,r}$ to the resonator and total capacitance $C_i = C_{i,r} + C_{i,p}$, $i = \{L, R\}$. The resonator has inductance L and capacitance C.

maximum fidelity is achieved when the detuning is set so that the CPHASE gate is performed in a small, integral number of oscillations. This approach is known as a geometric phase gate[47, 49, 77].

We quantify the strength of the qubit-resonator coupling by analyzing the effect of the resonator on the qubit's splitting. The voltage along a high-impedance resonator is much larger than for a conventional 50 Ω resonator [89, 80]; the voltage at the resonator's antinode due to a single photon is $V_0 = \sqrt{\hbar Z_r}\omega_r$, where ω_r is the resonator's frequency and Z_r its impedance. Quantum-dot-based qubits are compatible with high impedance resonators because they have only tens of attofarads of capacitance and thus have little parasitic effect on the impedance, $Z_r = \sqrt{L/C}$, where L and C are the total inductance and capacitance in the system, respectively. We consider exciting the resonator near its fundamental frequency, i.e., a half-wave resonator, and place qubits at its antinodes (Fig. 1a). The voltage at each antinode can be written $V_r = V_0(a + a^\dagger)$. This voltage shifts the chemical potentials of the quantum dots, which are characterized by a capacitance matrix describing the interactions between each dot and its electrostatic environment [94]. Denoting the DC contributions to this chemical potential by ϵ_0, we can write $\epsilon = \epsilon_0 + ec_gV_g + ec_rV_r$, where e is an electron charge, and c_g and c_r represent the lever arms between the double quantum dot and the RF gate and resonator, respectively, and which determine the shift in chemical potential of the DQD caused by a voltage shift on those gates. We define the drive on the RF gate as $eV_gc_g = \epsilon_d \cos\omega_d t$. We then expand J around ϵ_0 to second order:

$$\begin{aligned} J(\epsilon) \approx J(\epsilon_0) + \left.\frac{dJ}{d\epsilon}\right|_{\epsilon_0} \left(c_r V_0(a + a^\dagger) + \epsilon_d \cos\omega_d t\right) \\ + \frac{1}{2}\left.\frac{d^2J}{d\epsilon^2}\right|_{\epsilon_0} \left(c_r V_0(a + a^\dagger) + \epsilon_d \cos\omega_d t\right)^2 + \dots \end{aligned} \tag{3.1}$$

The Hamiltonian for a qubit-resonator system is $H_{QR} = \hbar\omega_r a^\dagger a + \frac{1}{2}J(\epsilon)\sigma_z$. We move to an interaction picture with respect to $H_0 = \hbar\omega_d a^\dagger a + \frac{1}{2}\tilde{J}(\epsilon_0)\sigma_z$, where $\tilde{J} = J(\epsilon_0) + \frac{1}{2}\left.\frac{d^2J}{d\epsilon^2}\right|_{\epsilon_1}(c_r^2V_0^2 + \epsilon_d^2/2)$ includes second-order corrections to the DC value of J. Considering the first two orders of expansion and averaging over oscillating terms yields:

$$
\begin{aligned}
H_{\text{int}} &= \hbar\Delta a^\dagger a + \frac{1}{4}\frac{d^2J}{d\epsilon^2}\Big|_{\epsilon_0}\big(c_r V_0 \epsilon_d (a + a^\dagger) + 2c_r^2 V_0^2 a^\dagger a\big)\sigma_z \\
&= \hbar\Delta a^\dagger a + \tfrac{1}{2} g (a + a^\dagger)\sigma_z + \tfrac{1}{2}\chi a^\dagger a \sigma_z,
\end{aligned} \tag{3.2}
$$

where $\Delta = \omega_r - \omega_d$ is the detuning, and $g = \frac{1}{2}\frac{d^2J}{d\epsilon^2}\big|_{\epsilon_0} c_r V_0 \epsilon_d$ and $\chi = \frac{d^2J}{d\epsilon^2}\big|_{\epsilon_0} c_r^2 V_0^2$ are coupling strengths. The second coupling χ is smaller than g by a factor of $c_r V_0/\epsilon_d \ll 1$ for the optimal drive that we will consider, and so we will ignore it for the remainder. Higher order terms do not add additional terms to the equation, they only change their relative magnitude.

To create a two-qubit coupling, we now add a second qubit to the model at the opposite antinode of the resonator, and drive it at the same frequency ω_d and 180° out of phase as the first qubit, giving the two-qubit Hamiltonian $H_2 = \hbar\Delta a^\dagger a + \frac{g_1}{2}(a + a^\dagger)\sigma_{z1} + \frac{g_2}{2}(a + a^\dagger)\sigma_{z2}$. The technique of driving two qubits in resonance to enlarge the longitudinal coupling to the resonator and in turn one another is also employed in [79]. Following Roos et al.[77], it can be shown that H_2 generates a time-dependent phase space displacement $U(t) = \exp[-i\Delta \cdot t a^\dagger a]\hat{D}[\alpha(t)]\exp[\Phi_{12}\sigma_{z1}\sigma_{z2}]$, where $\hat{D}$ is a qubit-dependent displacement operator, $\alpha(t) = (1 - e^{i\Delta\cdot t})(g_1\sigma_{z1} + g_2\sigma_{z2})/(2\hbar\Delta)$, and $\Phi_{12}(t) = \frac{g_1 g_2}{2\hbar^2\Delta^2}(\Delta \cdot t - \sin\Delta \cdot t)$. When $\alpha(t) = 0$, the resonator disentangles from the qubits. A CPHASE gate occurs on the qubits when $\Phi_{12} = \pi/4$. Together, this requires that $\Delta \cdot t_g = 2\pi n$ and $\frac{g_1 g_2}{2\hbar^2\Delta} t_g = \pi/4$, where n is a positive integer. This yields a requirement on the detuning $\hbar\Delta = 2\sqrt{n g_1 g_2}$, and a CPHASE gate time $t_g = \pi\hbar\sqrt{n/(g_1 g_2)}$. While $n = 1$, corresponding to a single oscillation of the resonator, yields the fastest gate, we will also consider $n > 1$

gates to allow compatibility with dynamical decoupling, described below.

We now turn to an analysis of the main decoherence processes of this gate. There are two main sources of loss in the system: dephasing of the qubits and loss of photons from the resonator. A master equation that governs the time evolution of the total system is:

$$\dot{\rho} = -i[H_2, \rho] + 2\kappa\mathcal{D}[a]\rho + \gamma_{\phi,1}\mathcal{D}[\sigma_{z1}]\rho/2 + \gamma_{\phi,2}\mathcal{D}[\sigma_{z2}]\rho/2, \tag{3.3}$$

where $\kappa = \omega_r/(2Q)$ is the cavity decay rate, $\gamma_{\phi,i} = 1/T_{2,i}$ is the dephasing rate of qubit i, and $\mathcal{D}[c]\rho = c\rho c^\dagger - c^\dagger c\rho/2 - \rho c^\dagger c/2$ is the usual damping superoperator. We neglect T_1 effects because T_1 exceeds T_2 by several orders of magnitude in most S-T_0 systems. We note that, while T_2 is limited by charge noise with a $1/f$ spectrum, the damping superoperator implements white noise. As a result, we expect the fidelities from solving this master equation to be slightly lower than in an exact simulation based on $1/f$ noise.

In this master equation, it is straightforward to analytically solve the dephasing of the qubits because all terms in the Hamiltonian commute with σ_z. Each qubit therefore dephases at the rate $\gamma_{\phi,i}$ throughout the gate. For dephasing due to loss of photons from the resonator, it is illustrative to solve the master equation analytically using a quantum trajectory approach. We make the simplifying assumption that $g_1 = g_2 = g$ and $\gamma_{\phi,1} = \gamma_{\phi,2} = \gamma_\phi$. In general, if the qubits differ, we can replace g and γ_ϕ in equations below with the geometric mean of the terms in the different qubits. The resulting dephasing process on the two qubits can be viewed as a stochastic process depending on whether an even or odd number of photons are lost from the cavity. Odd numbers of lost photons result in a random π phase shift of one of the qubits, whereas even numbers of lost photons result in a correlated π phase shift of both qubits. The full analytical derivation of the system's evolution is provided in Appendix 3.7.

3.3 AVERAGE GATE FIDELITY

We can use the analytical derivation of the density matrix at the conclusion of the gate to find the average gate fidelity. The average gate fidelity $\bar{F}_g$, as defined in Refs. [69, 64], is used as a measure to assess the performance of a noisy quantum gate compared with an ideal (unitary) gate. It can be related to the fidelity of entanglement F_e, which is a simpler quantity to directly calculate, through the relation $\bar{F}_g = \frac{dF_e+1}{d+1}$, where d is the dimension of the Hilbert space ($d = 4$ in the case of a two-qubit gate).

We define a map to represent the action of our noisy CPHASE gate on a density matrix of two qubits as $\rho' = \mathcal{N}_g[\rho]$. This map can be expressed as a matrix that acts on the space of density operators for 2 qubits. To calculate the fidelity of entanglement for this two-qubit gate, we consider a maximally entangled state of *four* qubits, with two of the qubits acted on by the gate. Let $|\Psi\rangle = \frac{1}{2}\sum_{i,j=0,1}|ij,ij\rangle$ be the maximally entangled state of four qubits, with density matrix given by $\rho_\Psi = |\Psi\rangle\langle\Psi| = \frac{1}{4}\sum_{i,j,k,l=0,1}|ij,ij\rangle\langle kl,kl|$. Then $\rho'_\Psi = (\mathcal{N}_g \otimes I)[\rho_\Psi]$ is a 4-qubit density matrix where the map $\mathcal{N}_g$ has been applied to qubits 1 and 2, and nothing has been done to qubits 3 and 4. We define $|\Psi'\rangle = (U_g \otimes I)|\Psi\rangle$ as the state of the system after it has evolved under the ideal gate, so the fidelity of entanglement is

$$F_e = \langle\Psi'|(\mathcal{N}_{t_g} \otimes I)[\rho_\Psi]|\Psi'\rangle = \langle\Psi|(\mathcal{N}'_{t_g} \otimes I)[\rho_\Psi]|\Psi\rangle\,, \tag{3.4}$$

where we have defined $\mathcal{N}'_{t_g} = \mathcal{U}_g^{-1} \circ \mathcal{N}_{t_g}$ with $\mathcal{U}_g^{-1}$ being the inverse ideal gate. That is, $\mathcal{N}'_{t_g}$ describes only the noise in the gate.

This expression for the fidelity of entanglement can be made more explicit by using a trace-orthonormal basis of 2-qubit operators, such as the 2-qubit Pauli operators, to resolve the inner product of Eq. (3.4). Let $\{\rho_\mu, \mu = 1, \ldots, 16\}$ be such a basis. Then

$$F_e = \frac{1}{16}\sum_\mu \mathrm{Tr}\big[\rho_\mu^\dagger\big(\mathcal{N}'_{t_g}(\rho_\mu)\big)\big]\,, \tag{3.5}$$

We can then analytically calculate the gate fidelity using the basis of 2-qubit operators ρ_μ as initial states $\rho(0)$ in the solution of Eq. (3.29). Note that, for our numerical simulations, we use physical density matrices ρ_k constructed from all two-qubit combinations of single qubit states $|0\rangle$, $|1\rangle$, $\frac{1}{\sqrt{2}}(|0\rangle + |1\rangle)$, $\frac{1}{\sqrt{2}}(|0\rangle + i\,|1\rangle)$ states, which can easily be shown to form an orthonormal basis of the operator space.

Given the analytical expression for the noisy CPHASE gate given in Eq. (3.29), and including qubit dephasing as described by Eq. (3.59), we can analytically calculate the average gate fidelity. Specifically, the terms in Eq. (3.29) corresponding to zero, odd, and even numbers of lost photons provide Kraus operators for an operator product expansion of the map $\mathcal{N}_{t_g}$. The average gate fidelity evaluates to

$$\bar{F_g} = \frac{1}{10}(4 + 4b(t_g)e^{-\gamma_\phi t_g} + (b(t_g)^4 + 1)e^{-2\gamma_\phi t_g})\,, \tag{3.6}$$

where $b(t_g)$ represents the effect of photons lost from the resonator during the gate and remaining in the resonator at its completion and is defined in (3.33) If we take the first order Taylor expansion of this around κt_g and $\gamma_\phi t_g$, we find:

$$1 - \bar{F_g} \approx \tfrac{4}{5}(\gamma_\phi t_g + \kappa t_g/(2n)). \tag{3.7}$$

In the limit of small dephasing, the optimal gate time is $t_g = \sqrt{n}\pi\hbar/g$, and the corresponding gate fidelity $\bar{F_g}$ becomes

$$1 - \bar{F_g} \approx \frac{4\sqrt{n}\pi}{5g}(\gamma_\phi + \kappa/(2n)) = \frac{8\sqrt{n}\pi\epsilon_0^2}{5c_r J\sqrt{\hbar Z_r}\omega_r\epsilon_d}(\gamma_\phi + \frac{\omega_r}{4nQ})\,. \tag{3.8}$$

This simple expression for the fidelity enables us to find the optimal values of J and ϵ_d, giving a clearer picture of how the fidelity of the gate depends on the resonator's parameters and charge noise in the system.

3.4 EFFECT OF CHARGE NOISE ON OPTIMAL DRIVE AND FIDELITY

To optimize the parameters for driving the qubits with respect to their noise baths, we consider how spin qubits dephase under the influence of charge noise [20, 18]. Charge noise has a power spectrum described by $S(f) = S_\epsilon/f^\beta$, where β is between 0.6 and 1.4 for a "1/f" spectrum[43]. In the singlet-triplet qubit, we find that the noise is best understood as fluctuating charges affecting the chemical potentials of the quantum dots, which can be quantified by S_ϵ, a function of the substrate, the dots' geometry and the qubit's wave function. To understand how this couples to the qubits' splitting, we perform a Taylor expansion similar to that in 3.1, but we include an error term, $\delta\epsilon$, that is time-dependent but negligible at the resonator's frequency due to the 1/f nature of charge noise. Retaining terms linear in $\delta\epsilon$ in the third-order expansion and setting terms oscillating at the resonator frequency, we find:

$$\delta J \approx \delta\epsilon\left(\frac{dJ}{d\epsilon}\bigg|_{\epsilon_0} + \frac{1}{4}\,\frac{d^3J}{d\epsilon^3}\bigg|_{\epsilon_0}\epsilon_d^2\right). \tag{3.9}$$

We can then find S_J using the relation $S_J = 1/2(\frac{\delta J}{\delta\epsilon})^2 S_\epsilon$. Empirical studies show that J is an exponential of ϵ, $J(\epsilon) \approx J_0\exp(\epsilon/\epsilon_a)$, where J_0 and ϵ_a are tuning-dependent but can be treated as constants throughout multiple experiments where tuning is not substantially changed.

We consider the possibility of employing dynamical decoupling pulses, despite the added complexity and requirement to perform the gate during multiple resonator oscillations, as they dramatically improve coherence times. Most gains come from a single echo, applied half-way through the gate time, which increases coherence times by about a factor of 30 [20]. For this reason, previous implementations of two-qubit gates in this system [86, 63] have employed a Hahn echo or rotary echo. Both gates rely on the same $\sigma_z \otimes \sigma_z$ interaction, so by performing simultaneous echoes on the qubits, we cancel noise but not the coupling. We intend to use the same technique in performing this gate, but to do this without affecting the CPHASE gate requires more care when the qubits are entangling with a resonator. One must perform echo π pulses when the qubit is fully disentangled with the resonator, which can be achieved by performing the gate over multiple oscillations of the resonator.

To understand how T_2 varies with J, we consider previous work studying the effect of dynamical decoupling for colored noise [18]. If we implement dynamical decoupling with Gaussian charge noise, the resultant decay of qubit coherence takes the form $A(t) \propto \exp(-(t/T_2)^{1+\beta})$. In general, $T_2 = m^\beta/(\eta S_\epsilon^{1/(\beta+1)})$, where η is a constant of order 1 and m is the number of pulses performed. For certain pulse types, η can be solved for analytically; for instance, for a Hahn echo, $\eta = \frac{1}{(2\pi)}(2^{1-\beta}-1)\Gamma(-1-\beta)\sin(\frac{\pi\beta}{2})$. Combining the equations above, we find

$$1/T_2 = \left(\eta S_\epsilon \frac{J^2}{\epsilon_a^2}\left(1+\frac{\epsilon_d^2}{4\epsilon_a^2}\right)^2\right)^{\frac{1}{\beta+1}} \equiv \gamma_{\phi,0}\left(1+\frac{\epsilon_d^2}{4\epsilon_a^2}\right)^{\frac{2}{\beta+1}}, \tag{3.10}$$

where we've defined the term $\gamma_{\phi,0}$ to represent the dephasing rate at a given value of J with no drive applied. For the values of S_ϵ and β used in simulations for this paper, and with no drive applied, $T_2(J)$ takes on the same set of values as in Ref [20]. We optimize ϵ_d assuming exact $1/f$ noise to simplify the solution and from numerical solutions we find that this gives an accurate result, with the infidelity about 2% lower when the exact form is used.

Using the model of the spectrum for charge noise with $\beta < 1$, we can find optimal values $\epsilon_{d,\text{opt}}$ and J_{opt} for the drive : $\epsilon_{d,\text{opt}} = 2\epsilon_a\sqrt{1+\frac{\kappa}{2n\gamma_{\phi,0}}}$ and $J_{\text{opt}} = (\frac{\beta}{2n(1-\beta)}\kappa)^{(1+\beta)/2}\frac{\epsilon_a}{\sqrt{S_\epsilon \eta}}$. The value J_{opt} has a strong dependence on β, going to ∞ for true $1/f$ noise and 0 for white noise. Because

J is limited to between about 50 MHz, where it becomes too small to drive effectively, and tens of GHz, we will not always be able to achieve the optimal value, but for values of $\beta \approx 0.7$ that have been measured previously, those limits are not reached [20]. Upon substituting in the optimal values $\epsilon_{d,\text{opt}}$ and J_{opt}, we find that

$$1 - \bar{F}_g \approx \frac{4/5\pi \left(\frac{2^3 n}{\beta}\right)^{\beta/2} (1-\beta)^{(1-\beta)/2} \sqrt{S_\epsilon \eta}}{\sqrt{\hbar Z_r} c_r Q^{(1-\beta)/2} \omega_r^{(1+\beta)/2}}. \tag{3.11}$$

We note that (3.11) does not apply for $n = 1$, because there S_ϵ takes on a much larger, low-frequency value.

3.5 Expected Gate Performance

To estimate the gate time and fidelity, we now look at the range of possible values taken by the parameters in the above expressions. We first consider the impedance of the resonator. While transmission lines relying on magnetic inductance are limited to approximately the impedance of free space, $Z \approx 377\,\Omega$, kinetic inductance has no such physical limitation. Kinetic inductance, which arises from the inertia of electrons, can be found in several types of superconducting devices, including nanowires formed from type II superconductors and chains of SQUIDs. Using superconducting nanowires has yielded impedances up to 4000 Ω with quality 200,000 and chains of SQUIDs up to 50,000 Ω [80, 6]. Such large impedances preclude addressing or measuring the qubit using the resonator. The qubits we consider, however, allow for universal control and 98% measurement fidelity independent of the resonator, and this has the added benefit of not requiring additional high fre-

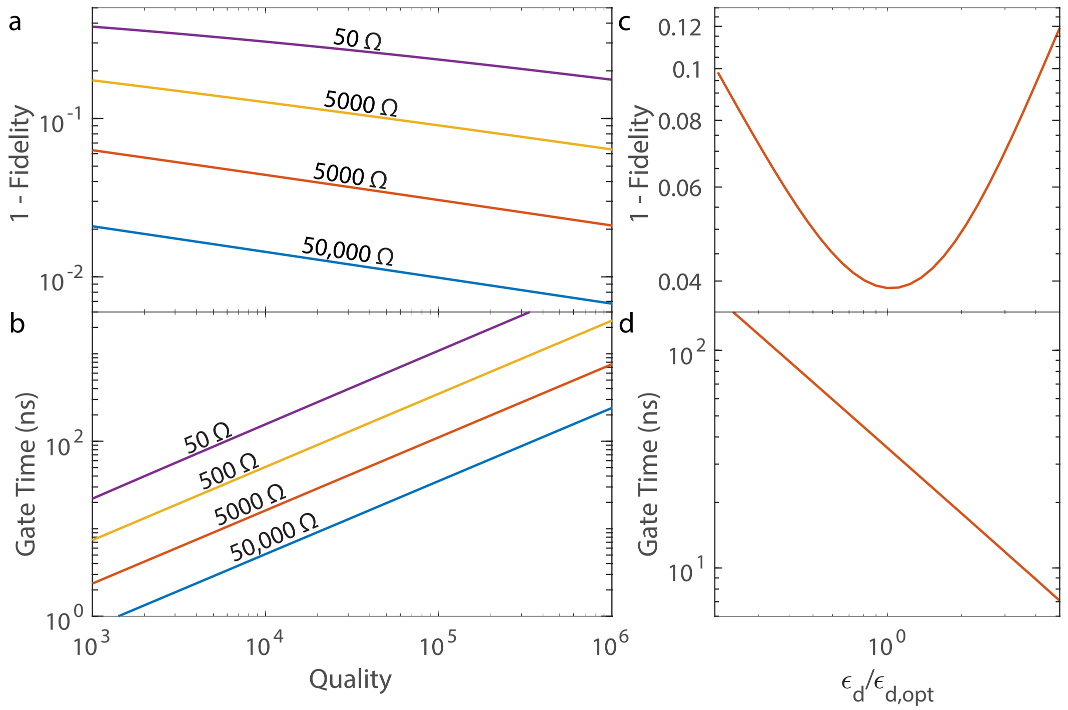

Figure 3.2: **a**, Average gate fidelity simulated by a numeric solution of the master equation with optimal values of J and ϵ_d as a function of resonator quality for resonator impedances of 50 Ω (standard), 500 Ω (maximum for magnetic impedance), 5000 Ω (typical nanowire), 50,000 Ω (SQUID array). **b**, CPHASE gate time for the same parameters as in a. **c** and **d**, Average gate fidelity and gate time as ϵ_d is varied around its optimal value with $Z_r = 5000 \ \Omega$ and $Q = 20,000$. As quality increases, the gate time for the maximum fidelity gate increases as well, but by adjusting the drive, faster gate times can be achieved with minor loss of fidelity.

quency lines for resonators. High-impedance nanowires are typically much more compact than traditional resonators: for instance, a 5 GHz nanowire is of order 1 mm in length, but because it is only 100 nm wide, it can be folded so that it occupies a $(20\mu\text{m})^2$ area, or it can be extended to transport information over longer distances. Because S-T_0 qubits are typically a few μm^2 in size, this retains the small size of a quantum dot based quantum processor, necessary for scaling to large numbers on chip.

We next turn to the qubit-resonator coupling. Because the S-T_0 qubit has a dipole-like charge distribution, to generate a large coupling, we must maximize the coupling to one of the dots comprising the qubit while minimizing the coupling to the other dot. This is quantified by the lever arm, $c_r = C_{R,r}/C_R - C_{L,r}/C_L$, with $C_{i,r}$ the capacitance between the resonator and each dot and C_i the total capacitance of each dot. COMSOL simulations predict its value can range from 0 to 0.3, with $c_r = 0.05$ for previously measured functioning S-T_0 qubits in GaAs. In Fig. 3.1**b-c**, we show two proposals for resonator and qubit geometries in silicon-silicon germanium (Si-SiGe) quantum well devices. In Fig. 3.1**c**, the resonator is at the same layer as the depletion gates and laterally adjacent to the near quantum dot, for which we predict c_r to be 0.25. This large coupling relies on precise knowledge of the location of the dot, as a small shift would substantially reduce the coupling. In Fig. 3.1**b**, we replace one of the accumulation mode gates, which are vertically separated by an additional oxide layer, with the resonator, for which we predict c_r to be 0.02. An ideal coupler would be as large as the gate in Fig. 3.1**b**, making it robust to different quantum dot locations, but would need to be separated by a much thinner layer of oxide, as has been used in recent experiments with aluminum gates separated with alumina [59].

We perform simulations of the density matrix to predict the expected average gate fidelity and gate time, as well as to confirm the power law behavior in Eq. (3.11). To solve the differential equation for the density matrix of the system, we use a 4th order Runge-Kutta equation. The resonator can be populated up to 5 photons; the 5th level has a population of lower than 10^{-4} for all simulations. We use time spacing of 20 ps unless this gives more than 10,000 or under 200 time steps, in which case we use those limiting values. We use parameters $S_\epsilon = 1.4 \times 10^{-16}\,\mathrm{eV}^2/\mathrm{Hz}^{1-\beta}$, $\beta = 0.67$, $c_r = 0.18$, the lever arm for devices that have been measured in GaAs, $w_r/(2\pi) = 6.5$

GHz and $\eta = 0.086$, which corresponds to a Hahn echo pulse. The value of S_ϵ was measured in a GaAs device, as it has not available for any silicon devices at this time.

In Fig. 3.2**a-b**, we plot the simulated fidelity as a function of resonator quality and impedance. Fidelity ranges from 96% to 99.3%, an improvement of a factor of 5 to 25 compared to the maximum Bell state fidelity of 72% achieved for the static capacitive gate reported in Ref. [86]. The dephasing experienced by the qubit increases by a factor of close to 3; dephasing through the resonator increases the total rate by only about 50%, however driving J doubles the total noise. Gate times near 10 ns are readily achievable, as can be seen by inspection of Fig. 3.2**b,d**. The dependence of $\epsilon_{d,\text{opt}}$ and J_{opt} on the resonator's quality and the qubits' noise bath acts to equalize the effective noise from the two noise sources, the qubits and the resonator, for whatever the absolute values of noise may be. For instance, an increase in S_ϵ requires that we decrease J and ϵ_d to keep the total noise originating with the qubit constant. As a result, the optimal gate time increases with quality, as that dictates a reduction of J_{opt} and $\epsilon_{d,\text{opt}}$. We can decrease the gate time at the cost of fidelity, as is shown in Fig. 3.2**c-d**. Here, we sweep ϵ_d while keeping all other parameters constant, and see that gate time has an inverse linear dependence on it, while the infidelity has a quadratic relationship on it, so the gate time can be substantially decreased without a corresponding excessive decrease in the fidelity. We note that the values of g we find are generally larger than those in recent experimental works [60, 45, 81], which we attribute to increased coupling to charge in the singlet-triplet qubit and the ability to increase g by driving the qubit in our model.

While our focus has been on the coupling between two qubits, it is straightforward to include more qubits. Because the resonator does not require additional wiring, incorporating a resonator for each qubit pair does not impose scaling challenges. Another benefit of using resonators for two-qubit gates arises from the relative ease of fabricating and characterizing resonators compared to spin qubits. Improving the static capacitive gate's fidelity requires reducing charge noise in the system, which remains poorly understood and is challenging and time-consuming to measure. By comparison, resonator fabrication is an area of extremely active research, and dozens of resonators can be made and tested at once. High-impedance resonators will enable entangling gates to be performed in noisier samples than the pristine GaAs heterostructures that have been used in the past, an asset in the endeavor to scale to larger numbers of qubits.

3.6 LEVER ARMS

For singlet-triplet qubits, it is common to define $\epsilon = \frac{V_L - V_R}{2}$, with V_L and V_R the voltages on the RF gates directly over the left and right quantum dots, because that can be directly set. Here, we have defined $\epsilon = \mu_L - \mu_R$, the difference in chemical potential between the left and right dots. Two terms are affected by this change of definition: $\frac{dJ}{d\epsilon}$ and S_ϵ. To convert these values, we first define $V_\epsilon = \frac{V_L - V_R}{2}$. Then $\frac{dJ}{d\epsilon} = \frac{dJ}{dV_\epsilon}\frac{dV_\epsilon}{d\epsilon}$ and $S_\epsilon = S_{V_\epsilon}(\frac{d\epsilon}{dV_\epsilon})^2$. We define $C_i,\ i = \{L, R\}$, to be the total capacitance of the left and right quantum dot, and $C_{i,j},\ i, j = \{L, R\}$ to be the capacitance between dot i and gate j. Then $\frac{d\epsilon}{dV_\epsilon} = e\left(\frac{C_{LL} - C_{LR}}{C_L} - \frac{C_{RL} - C_{RR}}{C_R}\right)$, where e is an electron charge. To find these capacitances, we perform a COMSOL simulation using a CAD file of the device, which allows us to extract a capacitance matrix for the system. We find that for the device in [20], with which S_ϵ was measured, $\frac{d\epsilon}{dV_\epsilon} = 0.182e$, which allows us to transform the power spectrum given in the paper, in terms of voltages on the gates, to the power spectrum of the dots' chemical potentials.

3.7 GEOMETRIC PHASE GATE

3.7.1 IDEAL GATE OPERATION

The ideal operation of our phase gate has been widely discussed in the ion trapping literature [46, 77]. We now give a brief outline of these results so that the discussion here is self-contained and to establish notation. This discussion follows [77] closely.

Consider first a driven oscillator of oscillation frequency ω_r. For our purposes it will be convenient to work in an interaction picture at the oscillator frequency. In this picture, there will only be a linear drive of the oscillator, which makes it easier to find the explicit time-evolution operator. A linear drive of the oscillator takes the general form

$$H_{\text{int}} = -i[E^*(t)a - E(t)a^\dagger], \tag{3.12}$$

where $E(t)$ is a complex amplitude describing the linear drive.

The resulting time-evolution operator generated by this Hamiltonian satisfies the differential equation

$$\frac{d}{dt}U(t) = -iH_{\text{int}}(t)U(t)/\hbar. \tag{3.13}$$

There is a particularly straightforward solution to this equation using Glauber's displacement operators, $D[\alpha] = \exp\left(\alpha a^\dagger - \alpha^* a\right)$. The time-evolution operator for H_{int} is

$$U(t) = D[\alpha(t)]\exp[\Phi(t)], \tag{3.14}$$

where

$$\alpha(t) = \int_0^t dt' E(t')/\hbar \tag{3.15}$$

$$\Phi(t) = \text{Im} \int_0^t dt' E(t') \int_0^{t'} dt'' E^*(t'')/\hbar^2. \tag{3.16}$$

This can be checked using standard facts about displacement operators. The phase factor Φ can be interpreted as the area enclosed in phase space by the oscillator dynamics; this can be seen by modifying the arguments at the end of the supplementary material of [49] and is discussed in [46].

We are interested in a system of two qubits longitudinally coupled to a single oscillator, in which case the interaction picture Hamiltonian involves only qubit-state-dependent forces on the oscillator and can be written

$$H_{\text{int}} = -i[E_1^*(t)\sigma_{z1} + E_2^*(t)\sigma_{z2}]a + \text{h.c.} \tag{3.17}$$

As noted in [77], because σ_{zi} is a constant of the motion and commutes with a and $a^\dagger$, we can obtain the solution for the full unitary by replacing the drive amplitude $E(t)$ by the qubit operator $E_1(t)\sigma_{z1} + E_2(t)\sigma_{z2}$ everywhere in the solution. Realistically, there would also be some direct drive of the oscillator of the form given by equation (3.12), but we defer consideration of this to a later section. The resulting time-evolution operator generated by this Hamiltonian is

$$U(t) = \hat{D}[\alpha_1(t)\sigma_{z1} + \alpha_2(t)\sigma_{z2}] \exp[\Phi_{12}(t)\sigma_{z1}\sigma_{z2}] \exp[\Phi_0(t)], \tag{3.18}$$

where

$$\alpha_j(t) = \int_0^t dt' E_j(t')/\hbar \tag{3.19}$$

$$\begin{aligned} \Phi_0 =& \mathrm{Im}\left(\int_0^t dt' E_1(t') \int_0^{t'} dt'' E_1^*(t'') + \int_0^t dt' E_2(t') \int_0^{t'} E_2^*(t'')\right)/\hbar^2, \\ \Phi_{12} =& \mathrm{Im}(\int_0^t dt' E_1(t') \int_0^{t'} dt'' E_2^*(t'') + \int_0^t dt' E_2(t') \int_0^{t'} E_1^*(t''))/\hbar^2. \end{aligned} \tag{3.20}$$

We have introduced the notation

$$\hat{D}[\alpha_1\sigma_{z1} + \alpha_2\sigma_{z2}] = \exp\left[(\alpha_1\sigma_{z1} + \alpha_2\sigma_{z2})a^\dagger \ -(\alpha_1^*\sigma_{z1} + \alpha_2^*\sigma_{z2})a\right].$$

$\hat{D}$ is a qubit-state-dependent displacement of the oscillator, so it is an entangling operation that acts on both qubits as well as the oscillator. We reserve the notation $D[\alpha]$ for the usual displacement operators that act nontrivially on the oscillator alone.

In the main text, we worked in an interaction picture with respect to the drive frequency ω_d, which has the Hamiltonian described by (3.2). When we move to the interaction picture used above, we find that the resulting interaction picture Hamiltonian is a special case of the one in (3.17):

$$H_{\text{int}} = -\frac{i}{2}\left[g_1 e^{-i\Delta t}\sigma_{z1} + g_2(t)e^{-i\Delta t}\sigma_{z2}\right] a + \text{h.c.} \tag{3.21}$$

Thus for the purposes of the main text we are interested in the case where $E_j = g_j e^{i\Delta t}/2$. In this case,

$$\alpha_j(t) = i\frac{g_j}{2\hbar\Delta}\left(1 - e^{i\Delta t}\right) \tag{3.22}$$

$$\Phi_{12} = \frac{g_1 g_2}{2\hbar^2\Delta^2}\left(\Delta t - \sin\Delta t\right), \tag{3.23}$$

and we want to choose a gate time such that $|\Delta| t_g = 2\pi n$, for which $\alpha_j = 0$ and the gate acts only on the qubits with $\Phi_{12} = \pm n g_1 g_2/2\hbar^2\Delta^2$, as stated in the main text.

Ultimately, we are interested in the time evolution operator generated by the Hamiltonian H_2 in the original interaction picture. This is straightforward to find from the textbook discussion of the interaction picture:

$$U(t) = \exp[-i\Delta t a^\dagger a]\hat{D}[\alpha_1(t)\sigma_{z1} + \alpha_2(t)\sigma_{z2}]\exp[\Phi_{12}(t)\sigma_{z1}\sigma_{z2}]\exp[\Phi_0(t)].$$

3.7.2 DEPHASING DUE TO CAVITY DECAY

We now consider the effects of dephasing on the two-qubit gate. It is illustrative to first study the effect of the decay of photons from the resonator on its own and how this decay affects the geometric phase acquired. Qubit dephasing is straightforward to incorporate later because it commutes with the gate. The restricted master equation is:

$$\dot{\rho} = -i[H_{\text{int}}, \rho] + 2\kappa\mathcal{D}[a]\rho\,. \tag{3.24}$$

We first write the solution of this master equation for the oscillator initially in its ground state and the pair of qubits in an initial state ρ_q, so that the initial state of the system is $\rho(0) = |0\rangle\langle 0| \otimes \rho_q$. At the conclusion of the gate, we average (trace) over the state of the cavity. Initial coherent and thermal states of the cavity are also tractable and will be discussed in a later section. We will restrict attention to the case where $E_1(t) = E_2(t)$; one could write analogous expressions with different driving on the two qubits, but certain simplifications would not occur.

We begin by defining $\alpha(t)$ so that it satisfies

$$\dot{\alpha} = -\kappa\alpha + E(t)/\hbar\,, \tag{3.25}$$

describing the amplitude of the oscillator subject to the decay rate κ. Associated with this differential equation we define a phase, analogous to the two-qubit phase acquired in the lossless case,

$$\Phi_{12}(t) = 2\text{Im}\int_0^t dt' E(t')\alpha^*(t')/\hbar. \tag{3.26}$$

Continuing the analogy, we define a two-qubit gate performed at time t_g,

$$U_g = \exp[i\Phi_{12}(t_g)\sigma_{z1}\sigma_{z2}]. \tag{3.27}$$

It can be shown that state of the qubits after evolving according to the master equation (3.24) and averaging over the oscillator is then

$$\rho_q(t_g) = U_g\mathcal{E}[\rho_q(0)]U_g^\dagger, \tag{3.28}$$

where $\mathcal{E}$ is a correlated dephasing process associated with residual excitations in the oscillator at the end of the gate and the excitations lost from the oscillator during the gate. The dephasing process $\mathcal{E}$ commutes with the action of the unitary gate U_g so the order of operations in equation (3.28) can be changed as required.

The correlated dephasing process can be described as

$$\mathcal{E}[\rho_q(0)] = \rho_0 + \rho_{\text{odd}} + \rho_{\text{even}}. \tag{3.29}$$

The three contributions correspond to, respectively, zero photons, an odd number of photons, and an even number of photons either lost from the cavity or remaining in it at the end of the pulse.

They are defined as follows:

$$\rho_0 = [(1+b)I - (1-b)\sigma_{z1}\sigma_{z2}]\rho_q(0)[(1+b)I - (1-b)\sigma_{z1}\sigma_{z2}]/4\,, \tag{3.30}$$

$$\rho_{\text{odd}} = \frac{1}{2}\left(1-b^4\right)[\sigma_{z1}+\sigma_{z2}]\rho_q(0)[\sigma_{z1}+\sigma_{z2}]/4\,, \tag{3.31}$$

$$\rho_{\text{even}} = \frac{1}{2}\left(1-b^2\right)^2[I+\sigma_{z1}\sigma_{z2}]\rho_q(0)[I+\sigma_{z1}\sigma_{z2}]/4\,, \tag{3.32}$$

where

$$b(t_g) = \exp\left(-4\kappa\int_0^{t_g} dt'|\alpha(t')|^2 - 2|\alpha(t_g)|^2\right). \tag{3.33}$$

Together, the equations (3.30-3.32) provide a Kraus operator expansion for $\mathcal{E}$.

As in the ideal case, we are most interested in the specific drive where $E = ge^{i\Delta t}/2$. In this case we find

$$\alpha(t) = -\frac{g}{2\hbar}\frac{1}{i\Delta+\kappa}(e^{-\kappa t} - e^{i\Delta t}). \tag{3.34}$$

Substituting this into (3.33) yields

$$\begin{aligned} b(t_g) =& \exp\left[\frac{-\kappa t_g g^2}{\hbar^2(\Delta^2+\kappa^2)} + \frac{g^2(\Delta^2-\kappa^2)}{\hbar^2(\Delta^2+\kappa^2)^2}(\cos\Delta t_g e^{-\kappa t_g} - 1)\right. \\ &\left. + \frac{2g^2 e^{-\kappa t_g}\kappa\Delta}{\hbar^2(\Delta^2+\kappa^2)^2}\sin\Delta t_g\right]. \end{aligned} \tag{3.35}$$

At $t_g = \pi\sqrt{n}\hbar/g$ and $\hbar\Delta = 2\sqrt{n}g$, this simplifies to $b(t_g) = \exp(-\pi\hbar\kappa/(2g\sqrt{n}))$ when $\kappa \ll \Delta$.

3.7.3 EXPLICIT SOLUTION TO THE MASTER EQUATION

In this subsection we will justify the expression for the state of the qubits at the conclusion of the gate (3.28). Recall that this arises from solving the dynamics according to the master equation (3.24) with the initial state $\rho(0) = |0\rangle\langle 0| \otimes \rho_q$ and then averaging over the state of the oscillator. The correlated dephasing of the qubits described by (3.29) arises from both the operation of the gate and the entanglement of the qubits with the oscillator at the conclusion of the gate. These two contributions can be seen in the two terms in the exponent on the right hand side of equation (3.33).

Our approach in this section will be to first state the solution $\rho(t)$ to the master equation (3.24) with the initial condition given above. We will then outline an argument that verifies that this proposed solution satisfies the master equation (although we originally found the solution by solving the master equation explicitly, the details are unnecessarily complicated to repeat here). In the second step of the calculation, we will average over the oscillator to obtain the reduced density matrix ρ_q for the qubits alone, recovering the claimed solution (3.29). Readers willing to trust this solution may wish to skip the rest of this subsection.

It will be simpler to write various intermediate expressions as members of a one-parameter family of correlated dephasing processes $\mathcal{E}_b$ that we define as follows:

$$\mathcal{E}_b[\rho_q(0)] = \rho_0 + \rho_{\text{odd}} + \rho_{\text{even}}. \tag{3.36}$$

The terms on the right hand side are defined as

$$\rho_0 = [(1+b)I - (1-b)\sigma_{z1}\sigma_{z2}] \times \rho_q(0)[(1+b)I - (1-b)\sigma_{z1}\sigma_{z2}]/4\,, \tag{3.37}$$

$$\rho_{\text{odd}} = \tfrac{1}{2}\left(1-b^4\right)[\sigma_{z1}+\sigma_{z2}]\rho_q(0)[\sigma_{z1}+\sigma_{z2}]/4\,, \tag{3.38}$$

$$\rho_{\text{even}} = \tfrac{1}{2}\left(1-b^2\right)^2[I+\sigma_{z1}\sigma_{z2}]\rho_q(0)[I+\sigma_{z1}\sigma_{z2}]/4\,, \tag{3.39}$$

For this to be a valid quantum operation, the parameter b needs to satisfy $0 \le b \le 1$. This definition has the useful property that

$$\mathcal{E}_{b_1}[\mathcal{E}_{b_2}[\rho]] = \mathcal{E}_{b_1 b_2}[\rho]. \tag{3.40}$$

The value of b for the solution is given in (3.33).

Given that notation, the solution to the master equation with our desired initial state is

$$\rho(t) = U_g\hat{D}[\alpha(\sigma_{z1}+\sigma_{z2})]\big(|0\rangle\langle 0| \otimes \mathcal{E}_{b_l}[\rho_q]\big)\hat{D}^\dagger[\alpha(\sigma_{z1}+\sigma_{z2})]U_g^\dagger, \tag{3.41}$$

where α, and U_g are defined above in equations (3.25), and (3.27) respectively and b_l, which represents the contribution to qubit dephasing arising from the *loss* of excitations from the oscillator during the operation of the gate, is defined as

$$b_l(t) = \exp\left(-4\kappa\int_0^t dt'|\alpha(t')|^2\right). \tag{3.42}$$

There are several ways to establish this solution. In our original approach we found analytical solutions to the quantum trajectory equations that describe the dynamics of the system as the oscillator emits excitations into the bath[104, 13] and then summed over the number of emissions and averaged over the various emission times. In this solution, ρ_0 is associated with trajectories in which no emissions occur, ρ_{odd} with an odd number of emissions, and ρ_{even} with an even number of emissions. While this calculation gives a nice physical picture, the details are tedious and to verify the solution we just need to check that it satisfies the master equation and has the appropriate initial condition as we do in the following.

We begin by performing the well-known polaron transform, often used to analyze the master equations for longitudinal coupling of qubits to oscillators [28]. This transformation simplifies the dynamics by essentially decoupling the qubits and the oscillator. The "polaron picture" density matrix is defined as follows:

$$\tilde{\rho}(t) = \hat{D}[-\alpha(\sigma_{z1} + \sigma_{z2})]\rho(t)\hat{D}^{\dagger}[-\alpha(\sigma_{z1} + \sigma_{z2})]. \tag{3.43}$$

Since $\alpha(0) = 0$, the initial condition for this master equation is $\tilde{\rho} = |0\rangle\langle 0| \otimes \rho_q(0)$. Our proposed solution for $\tilde{\rho}(t)$, from (3.41), is

$$\tilde{\rho}(t) = |0\rangle\langle 0| \otimes \left(U_g \mathcal{E}_{b_t}[\rho_q] U_g^{\dagger}\right). \tag{3.44}$$

In the polaron picture, the oscillator remains in the ground state at all times.

The master equation for $\tilde{\rho}$ is

$$\begin{aligned}\frac{d}{dt}\tilde{\rho} = &\left(\frac{d}{dt}\hat{D}[-\alpha(\sigma_{z1}+\sigma_{z2})]\right)\rho\hat{D}^{\dagger}[-\alpha(\sigma_{z1}+\sigma_{z2})]\\ &+\hat{D}[-\alpha(\sigma_{z1}+\sigma_{z2})]\rho\left(\frac{d}{dt}\hat{D}[-\alpha(\sigma_{z1}+\sigma_{z2})]\right)^{\dagger}\\ &+\hat{D}[-\alpha(\sigma_{z1}+\sigma_{z2})]\left(\frac{d}{dt}\rho(t)\right)\hat{D}^{\dagger}[-\alpha(\sigma_{z1}+\sigma_{z2})]. \qquad (3.45)\end{aligned}$$

Standard techniques can be used to show that

$$\begin{aligned}\frac{d}{dt}\hat{D}[-\alpha(\sigma_{z1}+\sigma_{z2})] =&[(\dot{\alpha}^{*}a-\dot{\alpha}a^{\dagger})(\sigma_{z1}+\sigma_{z2})+(\dot{\alpha}\alpha^{*}-\dot{\alpha}^{*}\alpha)(\sigma_{z1}\sigma_{z2}+I)]\\ &\times\hat{D}[-\alpha(\sigma_{z1}+\sigma_{z2})]. \qquad (3.46)\end{aligned}$$

After some calculations relying on the fact that the oscillator remains in its ground state, we find

$$\dot{\tilde{\rho}} \quad = \quad -i[\tilde{H}_{\text{int}},\tilde{\rho}]+2\kappa|\alpha(t)|^{2}\mathcal{D}[\sigma_{z1}+\sigma_{z2}]\tilde{\rho}, \qquad (3.47)$$

where

$$\tilde{H}_{\text{int}} = -i[E(t)\alpha^{*}(t)-E^{*}(t)\alpha(t)]\sigma_{z1}\sigma_{z2} \qquad (3.48)$$

and $\alpha(t)$ is a solution to equation (3.25).

It is easy to check that $\tilde{\rho}(t)$ as given in (3.44) satisfies the polaron picture master equation by substituting $\tilde{\rho}$ into the left and right hand side of (3.47) and checking that they match. This therefore shows that $\rho(t)$ is the correct solution of the original master equation.

The final step to find the state of the qubits $\rho_q(t)$ is to average over the oscillator by taking the partial trace

$$\rho_q(t) = U_g \mathrm{Tr}_{\mathsf{cav}} \left[\hat{D}[\alpha(\sigma_{z1} + \sigma_{z2})] \times \left(|0\rangle\langle 0| \otimes \rho_q' \right) \hat{D}^\dagger[\alpha(\sigma_{z1} + \sigma_{z2})] \right] U_g^\dagger, \tag{3.49}$$

where $\rho_q' = \mathcal{E}_{b_l}[\rho_q]$. To facilitate the calculation of the partial trace note that

$$\begin{aligned} \hat{D}[\alpha(\sigma_{z1} + \sigma_{z2})] =& D[2\alpha] \otimes |00\rangle\langle 00| + I \otimes |01\rangle\langle 01| \\ &+ I \otimes |10\rangle\langle 10| + D[-2\alpha] \otimes |11\rangle\langle 11|. \end{aligned} \tag{3.50}$$

We can make use of the following identity for a pair of coherent states,

$$\mathrm{Tr}[|\alpha\rangle\langle\beta|] = \langle\beta|\alpha\rangle = e^{-|\alpha|^2/2 - |\beta|^2/2 + \beta^*\alpha}. \tag{3.51}$$

It is then straightforward to verify that

$$\mathrm{Tr}_{\mathsf{cav}} \left[\hat{D}[\alpha_1\sigma_{z1} + \alpha_2\sigma_{z2}] \left(|0\rangle\langle 0| \otimes \rho_q' \right) \; \hat{D}^\dagger[\alpha_1\sigma_{z1} + \alpha_2\sigma_{z2}] \right] = \mathcal{E}_{b_e}[\rho_q'],$$

where we have defined

$$b_e(t) = \exp\left(-2\kappa |\alpha(t)|^2 \right). \tag{3.52}$$

b_e is the contribution to the dephasing of the qubits arising from the *entanglement* of the qubits with the oscillator at the conclusion of the gate.

Therefore, using (3.40), we obtain the desired result

$$\rho_q(t_g) = U_g \mathcal{E}_b[\rho_q] U_g^\dagger, \tag{3.53}$$

with $b(t) = b_l(t) b_e(t)$ given by equation (3.33).

3.7.4 Effect of direct oscillator drive and non-vacuum initial state

It may seem overly restrictive to restrict the initial oscillator state to the ground state. In practice, we would like to understand the behavior of the gate for both initial coherent and initial thermal states of the oscillator. Likewise, in practice the longitudinal coupling of the qubits to the oscillator will involve some direct drive of the oscillator, and we would like to model this effect. In this section, we explain how to extend the solution to these cases.

We consider an interaction picture Hamiltonian of the form

$$H_{\text{int}} = -i[E_c^*(t) + E^*(t)\sigma_{z1} + E^*(t)\sigma_{z2}]a + \text{h.c.} \tag{3.54}$$

which includes a direct cavity drive E_c. We consider initial states of the form $\rho(0) = |\beta\rangle\langle\beta| \otimes \rho_q$, where $|\beta\rangle$ is a coherent state. Finding the solution for an initial coherent state also allows us to model thermal states by averaging over a Gaussian probability distribution for β.

In the limiting case where the longitudinal coupling is negligible, it is straightforward to show that the solution is $\rho(t) = |\alpha_c(t)\rangle\langle\alpha_c(t)| \otimes \rho_q$ where $\alpha_c(t)$ satisfies

$$\dot{\alpha}_c = -\kappa\alpha_c + E_c/\hbar, \tag{3.55}$$

and $\alpha_c(0) = \beta$. Following the approach used in the previous section, we define

$$\tilde{\rho}(t) = D[-\alpha_c]\rho(t)D^\dagger[-\alpha_c], \tag{3.56}$$

so that $\tilde{\rho}(t) = |0\rangle\langle 0| \otimes \rho_q$ at all times for negligible longitudinal coupling.

Working with a master equation for $\tilde{\rho}$, we have

$$\dot{\tilde{\rho}} = \dot{D}[-\alpha_c]\rho D^\dagger[-\alpha_c] + D[-\alpha_c]\rho\left(\dot{D}[-\alpha_c]\right)^\dagger + D[-\alpha_c]\dot{\rho}(t)D^\dagger[-\alpha_c].$$

We find

$$\begin{aligned}\dot{\tilde{\rho}} =& -(\dot{\alpha}_c^* a + \dot{\alpha}_c a^\dagger)\tilde{\rho} - \tilde{\rho}(\dot{\alpha}_c a^\dagger + \dot{\alpha}_c^* a) - i[-iE_c^* a + iE_c a^\dagger, \tilde{\rho}] - i[H_{\text{int}}, \tilde{\rho}] + 2\kappa\mathcal{D}[a + \alpha_c]\tilde{\rho} \\ =& - i[\tilde{H}_{\text{int}}, \tilde{\rho}] + 2\kappa\mathcal{D}[a]\tilde{\rho}, \end{aligned} \tag{3.57}$$

where

$$\tilde{H}_{\text{int}} = -i[E_c^*(t)a - E_c(t)a^\dagger](\sigma_{z1} + \sigma_{z2}) - i[\alpha_c^*(t)E_c^*(t) - \alpha_c(t)E_c(t)](\sigma_{z1} + \sigma_{z2}).$$

We see that the coherent state in the oscillator can be handled by adding a classical drive that affects only the qubits. Since this drive term commutes with the terms that couple the qubits and the cavity, we can infer the solution to this master equation from the solution with no extra drive by adding an appropriate local unitary U_{1q} at the end of the calculation.

Again, we are interested in the reduced state of the qubits at the conclusion of the gate, which is given by $\rho_q(t_g) = \mathrm{Tr}_{\mathsf{cav}}[\rho(t_g)]$. Because the displacement is a unitary that acts only on the oscillator, it does not affect the partial trace, so $\rho_q(t_g) = \mathrm{Tr}_{\mathsf{cav}}[\tilde{\rho}(t_g)]$ and we can work entirely in this displaced picture to calculate the quality of the gate. We find as before

$$\rho_q(t_g) = U_{1q} U_g \mathcal{E}_b[\rho_q] U_g^\dagger U_{1q}^\dagger, \tag{3.58}$$

with $b(t)$ given by equation (3.33).

3.7.5 Adding qubit dephasing

The above analysis considered only the restricted master equation that describes dephasing due to cavity decay. As we noted above, it is straightforward to include qubit dephasing because all of the dephasing terms commute with one another. That is, the effect of intrinsic dephasing on each qubit can be described as a noise map on the input density matrix that acts independently of, and commutes with, the noise resulting from cavity decay.

As discussed in the main text, qubit dephasing for two qubits is described by a contribution to the master equation $\dot{\rho} = \gamma_{\phi,1}\mathcal{D}[\sigma_{z1}]\rho + \gamma_{\phi,2}\mathcal{D}[\sigma_{z2}]\rho$, and in the absence of coupling to the oscillator ($g = 0$), this has the following solution:

$$\begin{aligned}\rho_q(t) =&\mathcal{E}_q[\rho_q(0)] = (1-p_1)(1-p_2)\rho_q(0) + p_1(1-p_2)\sigma_{z1}\rho_q(0)\sigma_{z1} \\ &+ p_2(1-p_1)\sigma_{z2}\rho_q(0)\sigma_{z2} + p_1 p_2 \sigma_{z1}\sigma_{z2}\rho_q(0)\sigma_{z1}\sigma_{z2},\end{aligned} \tag{3.59}$$

where $p_j = \frac{1}{2}(1 - e^{-\gamma_{\phi,j}t})$. This intrinsic dephasing of the qubits is independent of the coupling to the cavity because all terms commute with σ_{z1} and σ_{z2}, so the overall solution is

$$\rho_q(t_g) = U_g \mathcal{E}[\mathcal{E}_q[\rho_q(0)]]U_g^\dagger. \tag{3.60}$$

The structure of this solution would be unchanged if the intrinsic qubit dephasing were non-Markovian and therefore not described by a master equation. The effect of the dephasing would still be described by some single qubit dephasing process of the same form as (3.59) with some values of p_1 and p_2, so (3.60) holds.

4

Quantum Dot and Singlet-Triplet Qubit Tuning and Measurement

4.1 Drift

Surprisingly, drift proved to be the most challenging problem in tuning up S-T_0 qubits with resonators. In the first generation of devices made from material provided by the Manfra group at

Purdue, which did not have resonators, this was a minor problem, with the junction between the (1,1) and (0,2) states slowly moving to more positive gate voltages over periods of months. However, in resonator devices, there were shifts of hundreds of millivolt after performing a singlet set of one-dimensional gate sweeps to check that all were working. Then, while quantum dots could typically be tuned up, they were not in the correct place, and they were often over tunnel coupled to the leads and could not be adjusted by local gates.

In troubleshooting, we made several devices using the same process but without the resonators, and these had the same issues. A very similar gate design had been successfully tuned many times previously. We had made some changes to the fabrication process to allow for the resonators. We had found that depositing NbN on samples after using the image reversal photoresist AZ-5214E on them, the NbN no longer superconducting. In one sample, we tried to remove this residue by with an ozone clean of the sample before annealing the ohmics, and in other samples by using PMMA in place of AZ-5214E in all parts of the recipe. We believe that the resist residue may have been acting as a tunnel barrier on the surface, preventing charge from accumulating.

Similar types of effects had been seen by other groups using the material, and the Manfra group investigated the physical cause was studied in Fallahi et al. [24]. They concluded that the electrons were being trapped by a donor state in the heterostructure shallower than the DX state and possessing a barrier to emission. It is likely that this led to the issues with tuning: the trapped electron created a electrical potential around the dots that we couldn't control, the precision afforded by the gates not sufficient to counteract the one internal to the material.

One approach to reducing this effect is to change the growth pattern to limit tunneling, and this may be the best approach in the long term. We took the short-term solution to solving this, growing 10 nm of HfO_2 on the surface before depositing gates [12]. Devices made with this oxide layer did not have drift issues, and in fact the incidence of "switches," multiple microvolt level jumps in voltage that occur over hour or day long periods, completely disappeared. However, as will be discussed at the end of this chapter, it had high-frequency noise levels about a factor of 10 higher than in previous devices. That HfO_2 was grown at 130 C, and it is thought at higher temperatures, HfO_2 is of higher quality. We began growing it at 220 C, and are planning to measure a device soon to see if the noise issues have been reduced.

4.2 Readout

Readout of the singlet-triplet qubit is performed using a nearby quantum dot, shown in Fig. 4.1**a**. This quantum dot is tuned so that it is at the most sensitive point of a Coulomb blockade peak, making its conductance maximally sensitive to its local charge environment. Then, when electrons move into the double dot from the 2DEG, or between the two dots, they cause a measurable shift in the quantum dot's conductance. This is used both for differentiating singlet and triplet states, used primarily when performing quantum information experiments and to measure the number of electrons in the quantum dot, used for the initial tuning to get the correct number of electrons in each dot and other parameters appropriately set.

To increase the speed of these measurements, we use RF reflectometry of the quantum with a tank circuit. These measurements have been described well in other theses [92], but I will go

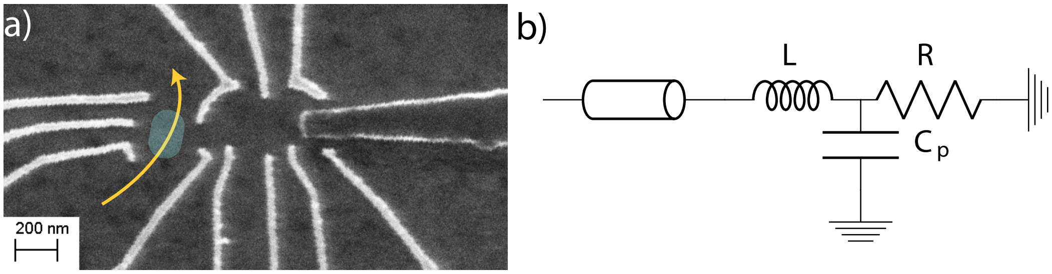

Figure 4.1: a) SEM of double quantum dot with resonator. Resonator is the darker grey. The quantum dot for readout is at far left, with its area highlighted in teal. The path through which measurement current travels is highlighted in yellow. b) Tank circuit shown at right. R represents the resistance of the quantum dot.

through the basic equations for comprehensiveness and discuss the practice of forming these circuits with quantum dots. The measurement circuit circuit used in these experiments is described in more detail in [27, 85].

The reflected signal from an impedance Z_{in} is

$$S_{11} = \frac{Z_{in} - Z_0}{Z_{in} + Z_0}, \tag{4.1}$$

so the sensitivity to changes in impedance is

$$\frac{dS_{11}}{dZ_{in}} = \frac{2Z_0}{(Z_0 + Z_{in})^2} \tag{4.2}$$

These will only start to have meaningful sensitivity well under a conductance quanta (7.75e-5 S). If we were to only send an RF signal down to the quantum dot and measure its reflection from it then, we can see from (4.2), the sensitivity is approximately, $2Z_0/R^2 \approx 10^{-7}$ S, near zero.

Incorporating a tank circuit "steps" down the quantum dot's impedance to Z_0 on resonance, allowing matching. The circuit is shown in Fig. 4.1**b** with the coaxial line connected to a printed circuit board with a Coilcraft wire-wound ceramic (1206CS) inductor soldered onto it. This is connected to the sensing quantum dot through wire bonds and then ohmic contacts. The capacitance to ground arises from parasitic capacitance, whose source is discussed at the end of the section. The input impedance of this circuit is:

$$Z_{in} = i\omega L + R\,||1/i\omega C_p = i\omega L + \frac{R}{1 + i\omega C_p R} = \frac{i\omega L + R(1-\omega^2 C_p L)}{1 + i\omega C_p R} \tag{4.3}$$

We will now define $Z_{LC} = \sqrt{L/C}$. The resonance occurs when the imaginary part of Z_{in} is 0, at frequency

$$\omega_0 = 1/\sqrt{LC}\sqrt{1 - (Z_{LC}/R_q)^2} \tag{4.4}$$

At ω_0, the real part of the impedance is equal to Z_{LC}^2/R. If the resistance of the sensor is $R = Z_{LC}^2/Z_0$, we achieve matching, and $S_{11} \rightarrow 0$, while the sensitivity from (4.2) is 0.5 S, a huge improvement over the measurement without a tank circuit.

There are a number of common issues that require troubleshooting when setting these up, and I will now discuss some of the main ones. Our purpose here has been to maximize the sensitivity of the measurement to the conductance of the quantum dot. To make comparisons, we solve for $\frac{dS_{11}}{dG}$, where $G = 1/R$. First, we calculate $\frac{dZ_{\text{in}}}{dG}$:

$$\frac{dZ_{\text{in}}}{dG} = 1/(\sqrt{1/Z_{LC}^2/ - G^2} - iG)^2 \approx Z_{LC}^2, \tag{4.5}$$

where we've made the approximation because we are working in the regime where $G \approx 1/(25Z_{LC})$

Putting everything together,

$$\frac{dS_{11}}{dG} = \frac{dS_{11}}{dZ_{in}}\frac{dZ_{\text{in}}}{dG} = \frac{2Z_0Z_{LC}^2}{(Z_0 + Z_{LC}^2G)^2} \tag{4.6}$$

When we are on matching, $Z_{LC}^2G = Z_0$, and the result is

$$\frac{dS_{11}}{dG} = Z_{LC}^2/2Z_0 = \frac{1}{2G_{\text{match}}} \tag{4.7}$$

In the typical case, however, we are on resonance ($\text{Im}(Z) = 0$) but not at the matching resistance. In those cases, it is simplest to write the conductance in terms of the matching resistance, so that $G = G_{\text{match}}/n$. Then,

$$\frac{dS_{11}}{dG} = Z_{LC}^2/2Z_0 = \frac{2}{G_{\text{match}}(1 + 1/n)^2} \tag{4.8}$$

By moving to lower matching conductances, we increase the sensitivity. Perhaps more importantly, at lower conductances the quantum dot itself becomes more sensitive to the qubit. As a metric, we use the change in reflection due to a change in the voltage of a gate next to the qubit. By working at the maximum sensitivity, about $0.2\ e^2/h$, we are at twice the sensitivity compared to when the dot is tuned to be a quantum point contact, at about $0.5\ e^2/h$.

In the current implementation of the tank circuit, we have two tank circuits multiplexed on one line, with the target frequency of one at 220 MHz and the other at 240 MHz. Typically upon getting a new board, we will choose inductors to put the resonant frequencies in the correct range. Typical inductors will have values from 620 nH to 820 nH, and matching resistances range from about $20,000\ \Omega$ to $30,000\ \Omega$. Both of these are above the matching conductance of a quantum point contact, so we can do better measurements by increasing the tank circuit's impedance.

It is useful to consider where the capacitance and resistance come from in this system. In GaAs, the resistance is simple: the wire bonds and gates are negligible (a few ohms). Using the ohmic process discussed in Appendix C, the contact resistance and undepleted 2DEG resistance across the mesa are about 30 Ω together. After the quantum dot, the current travels to ground through a $2000\ \Omega$ resistor, for filtering, but is probably primarily grounded through shunt capacitance. Thus, at the matching resistance, well over 90% of the resistance is at the quantum dot. In the case of accumulation-mode SiGe devices, this ratio changes dramatically due to the increased resistance of the 2DEG, making the conductance model we use above less useful.

We separate the capacitance into three sources: capacitance across the inductor, capacitance to the PCB, and capacitance of the 2DEG. The inductors themselves have a capacitance of about 200 fF. The PCB typically has the largest share of the capacitance, due to the unavoidable presence of metal on its surface. We saw an increase in that capacitance when we changed over to SMPM surface mount connectors for the RF lines for qubit control instead of connecting coaxial cables directly to the bonding pins. We have found that decreasing the board thickness by half decreased the capacitance by 150 fF, and that removing the metal plating on vias for the tank circuit had a similar effect. In this configuration, the capacitance is about 350 fF. On the device itself, we made two adjustments to reduce the capacitance: first, moving bonding pads away from the bonding pad for readout, and second, reducing the size of the mesa. Together, these reduced the device's capacitance to 140 fF from about 250 fF. We include these numbers to give a useful reference for those developing their own RF reflectometry systems.

This could certainly be reduced further, which, in addition to reducing the total capacitance, would also have the effect of making it possible to tune the sensor gate closest to the input signal more widely; as currently constituted, it must be set negative enough to deplete the 2DEG underneath it, or the capacitance of the ohmics is so high that no resonance can be seen. This wouldn't be necessary if the 2DEG were confined through etching only to the region they are meant to ultimately travel in.

So what improvements can be made? It's important to note that one of the major benefits of these tank circuits is that they are easy to use. The inductors are inexpensive and can easily be changed out to change the frequency. Their quality at 200 MHz is sufficient for the resistances we are matching. The bandwidth is about 10 MHz, which allows for two tank circuits to be multiplexed within the bandwidth of the circulator (the limiting feature in the circuit), reducing the amount of overhead by a factor of two. The frequency is low enough that little care has to be taken in impedance matching, and there are low losses in the coaxial lines going up the fridge. It is likely that improvements in matching resistance of about 50% can be made by further optimizing the board and gate design, but for more than that, a new approach is required. On the simpler end would be investing more in boards made with Rogers instead of FR-4, and making the RF lines properly impedance matched, allowing us to move the RF connectors away from the tank circuit. More invasive would be putting the inductor on the device, requiring additional fabrication, losing tunability of frequency, and likely pushing the frequency of the circuit up. At this point, other sensing means altogether, such as gate or resonator based dispersive sensing, become more appealing.

4.3 SOFTWARE FEEDBACK OF NUCLEAR MAGNETIC GRADIENT

Because the nuclear bath fluctuates on the timescale of seconds, there are a number of techniques that can be exploited to reduce its effect, such as the Hamiltonian estimation discussed in Chapter 2. To set the mean value of the gradient to our chosen value and reduce its fluctuations, we've typically used the technique of nuclear feedback described in Bluhm et al. [9] in the past, but recently have begun using software feedback. In software feedback, we measure the gradient, then perform singlet or triplet-plus pumping (in which we load a singlet, and adiabatically cross through the S-T_+ crossing, causing a spin-flip in the nuclei, or vice versa) for an amount of time calculated to shift the gradient to the desired value, then measure again, and repeat until the gradient is within a set tolerance of the given value. We have implemented this with using a Kalman filter, which lets us also track the pumping rates over time, and see that when the device is centered, we pump at about 0.1 to 0.2 MHz per ms (this corresponds to 30 μT). To minimize the measurement time, we collect data with the maximum time spacing possible that lets us resolve the frequency (we have used up to 4 ns, but larger values are possible) and fitting the data with a fast Fourier transform. Performing all of this in MATLAB, we can extend T_2^* to about 250 ns. It's certainly possible to do better than this; for instance, using an FPGA to analyze the data, we can achieve T_2^* of $1\ \mu s$.

However, this would increase the amount of overhead required, making basic experiments more difficult to set up and run. So unless experiments specifically are meaningfully improved by enlarging T_2^*, it's unlikely to be worth using. For instance, increasing T_2^* also reduces the amount of data it is possible to take before performing feedback again. We use the measurement of the diffusion rate from Chapter 2, $\mathcal{D} = 45$ kHz$^2/\mu s$ to approximate T_2^* as a function of the amount of time we run experiments for. If we assume that we feedback until ΔB_z has standard deviation σ_0, and then run experiments for a time t such that $\sigma_0 = \sqrt{Dt}, T_2^* \approx 1/1.3(\pi\sqrt{2Dt}) \approx 800$ ns$/\sqrt{\mathrm{t}}$ where t is the amount of time in milliseconds. If we assume that each feedback run takes a constant amount of time (this is reasonable, because too achieve larger T_2^*, we must achieve proportionally tighter tolerance on the set point), then working with $T_2^* = 1$ μs takes 16 times longer than $T_2^* = 250$ ns, so it's important to make sure that the trade off is worth it.

4.4 CHARGE NOISE

In measuring the S-T_0-resonator device, after checking that it was tunable, we were interested in if it had similar amounts of charge noise as had been measured in the past. We make two measurements of charge noise, the so-called low-frequency and high-frequency quantities.

The low-frequency noise measurement is similar to the dephasing curve measured in the previous section on Software Feedback (4.3). The pulse sequence is the Ramsey pulse sequence discussed in Chapter 1, in which we load a $|0\rangle$, perform an $\pi_x/2$ gate to rotate the state onto the y-axis of the Bloch Sphere, then turn on exchange, finally reading the state out with another $\pi_x/2$ gate to the z-axis, followed by measurement. We consider the noise to be quasistatic, and thus can use the decay function derived in Chapter 1, 1.9. We think of the noise as arising from charge fluctuations leading to fluctuations in ϵ, $\delta\epsilon$. Then the amount of frequency noise is $\delta J = \frac{dJ}{d\epsilon}\delta\epsilon = \frac{1}{\sqrt{2}\pi T_2^*}$. Numerically differentiating is quite noisy, so instead we make the empirically valid approximation that

$$J(\epsilon) = J_0 + J_1 \exp(-\epsilon/\epsilon_0), \tag{4.9}$$

and so we can write

$$\frac{dJ}{d\epsilon} = -J_1/\epsilon_0 \exp(-\epsilon/\epsilon_0). \tag{4.10}$$

We can then fit

$$-J_1/\epsilon_0 \exp(-\epsilon/\epsilon_0)\delta\epsilon + \sigma_0 = \frac{1}{\sqrt{2}\pi T_2^*}, \tag{4.11}$$

where we have included σ_0 as a first-order approximation to noise not dependent on $\frac{dJ}{d\epsilon}$. Fitting this equation gives us $\delta\epsilon = 18\ \mu V$. Again, the shaky units of ϵ come out to play: this ϵ refers to the voltages applied to the gates, not the chemical potential of the dot. To get a meaningful unit for the fluctuations in the qubit energy, we need the lever arm, which we did not measure for this device. However, the gate design is very similar to the device in Dial et al. [20], so we can directly compare the measured amounts of noise. In that case, $\delta\epsilon = 8\mu V$, indicating low-frequency noise as increased by about a factor of two. σ_0 is found to be 1 MHz.

One useful metric is $Q = JT_2^*$, the number of coherent oscillations.

$$Q = \epsilon_0 \frac{J}{J - J_0} \tag{4.12}$$

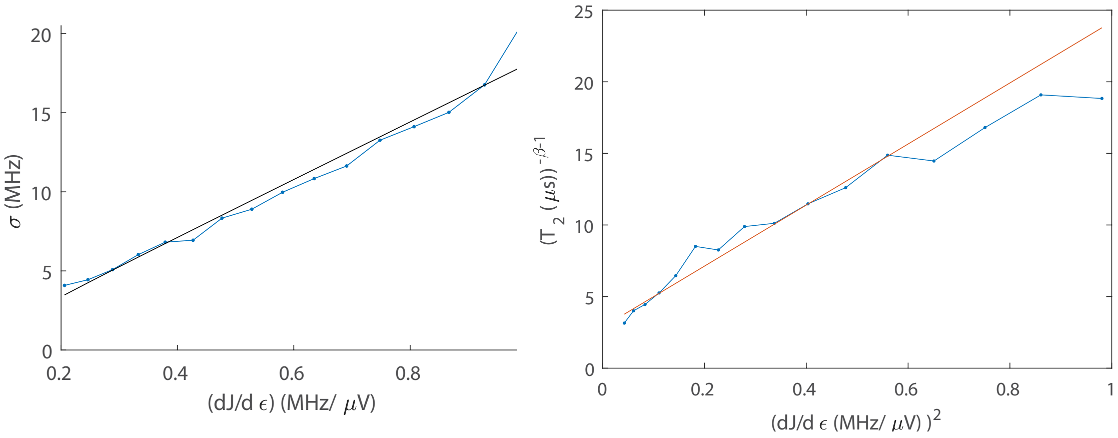

Figure 4.2: a) The linear fit for the high frequency noise. b) Linear fit for low frequency noise.

The Q for this device is around 3, about 4 times smaller in this device than in the previous device. Half of the reduction comes from increased noise, and half because ϵ_0 is about half as large as in the past. Qualitatively, this is probably related to a larger tunnel-coupling in this device than in the past. The high-frequency measurement is slightly more complicated. We follow the protocol described in Appendix B, assuming that the power spectral density has the form $S(\omega) = S_\epsilon/\omega^\beta$, so that

$$T_2^{1+\beta} = \left(\eta(\beta) S_\epsilon \frac{dJ}{d\epsilon}^2\right)^{-1}. \tag{4.13}$$

Then, we measure T_2, the Hahn echo coherence time, as a function of J, and extract the noise power, β, and magnitude S_ϵ. A summary of the data analysis is shown in Fig. 4.3. We note in particular that the fit for β is quite noisy. While this may be due to flaws in the data fit, it also may indicate that power law noise is no longer the correct form for the noise seen in the device, and other forms, such as the combination of white and $1/f$ noise, are worth examining. While the maxi-

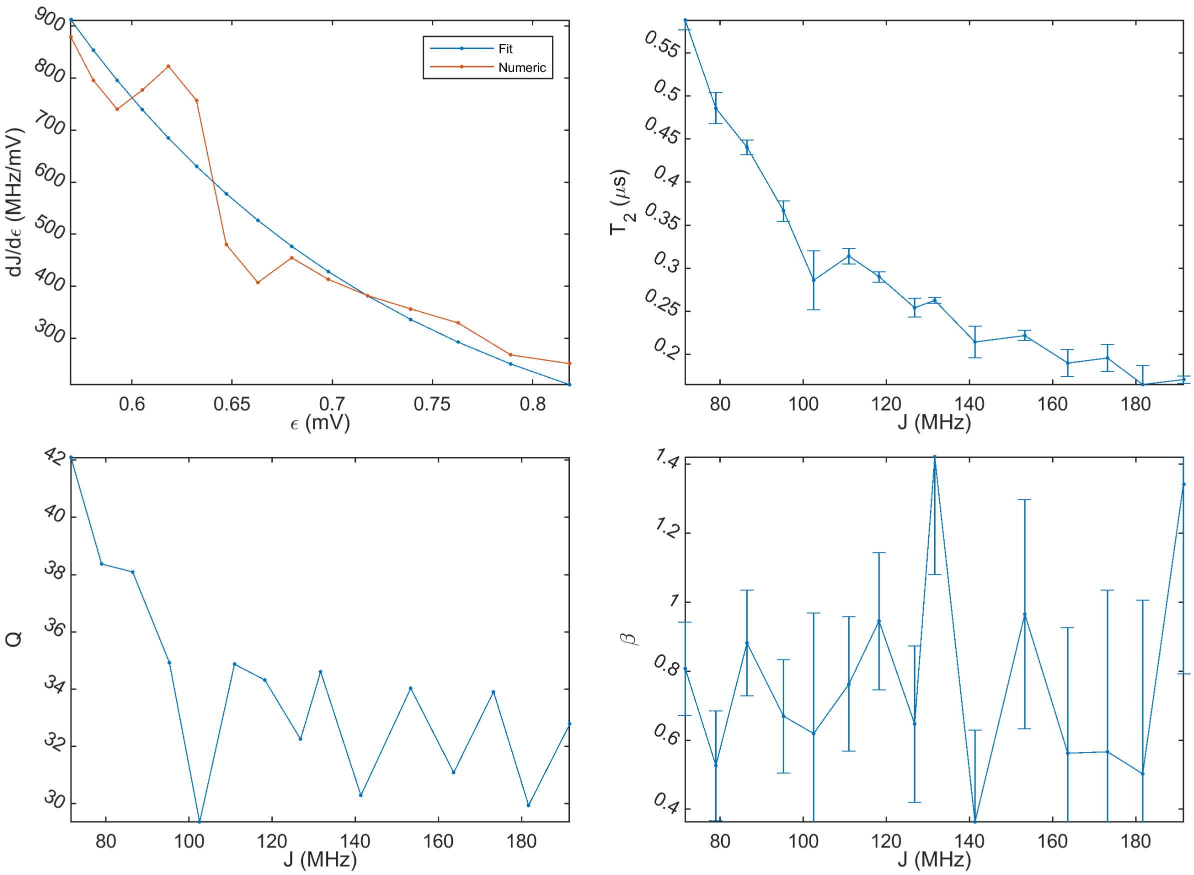

Figure 4.3: a) Numerically differentiated data for $\frac{dJ}{d\epsilon}$ (red) and $\frac{dJ}{d\epsilon}$ extracted from fit to $J(\epsilon)$ (blue). b) T_2 for echo data plotted vs. $J(\epsilon)$. c) Number of coherent oscillations for Hahn echo data. d) β, the noise power, plotted vs. $J(\epsilon)$

mum likelihood value of β, 0.75, is similar to the value of 0.7 measured in the past, the magnitude of the noise at 1 MHz is much larger, at $4\ \text{nV}/\sqrt{\text{Hz}}$. We have measured $0.5\ \text{nV}/\sqrt{\text{Hz}}$ [20] and $1.5\ \text{nV}/\sqrt{\text{Hz}}$ with other material grown by Mike Manfra.

We solve for Q_e, the number of coherent oscillations in the Hahn Echo experiment, using equations (4.9), (4.10) and (B.12), to find

$$Q_e = T_2 J = \frac{J}{[S_\epsilon \eta(\beta)(J - J_0)^2/\epsilon_0^2]^{1/(1+\beta)}}. \tag{4.14}$$

While we largely don't see the expected dependence on J, we can use this equation to compare these values of Q_e to those measured in the past. Values of Q_e in the previous data set were almost 20 times higher, at up to 500. Again, while part of the reduction stems from the increase in noise, another component comes from the change in ϵ_0, which has Q has a nearly nearly linear dependence on. It would be interesting in the future to investigate if it would be possible to increase the Q_e values of the device by reducing ϵ_0.

5

Superconducting Nanowire Fabrication and Measurements

Spin qubits have reduced coupling to charge compared to charge qubits, giving them far larger dephasing times and making them more viable for fault tolerant quantum computing. However, this also makes coupling to other qubits challenging, as quantum-dot-based qubits typically require electric charge in some form to mediate two-qubit interactions, as the magnetic fields generated by electron spins are too weak. As discussed in the previous chapter, using a resonator with characteristic impedance larger than $50\ \Omega$ enhances the coupling between qubit and resonator, because the magnitude of the voltage on the resonator antinode is proportional to the square root of the impedance. Increasing the impedance is thus a way to increase the gate speed without directly increasing the gate noise, making it an extremely valuable approach to improving gate fidelities.

To achieve large impedances of thousands of ohms, working with kinetic inductance is necessary, because magnetic inductance is limited to approximately the impedance of vacuum, $377\ \Omega$. Kinetic inductance arises from the inertia of charge carriers in the system. We can derive it using the Drude model, writing the equation of motion for charged particles in an electric field as

$$m\dot{v} = qE + mv/\tau,$$

where τ is the mean free time, m the particle's mass and q its charge. In superconductors, $\tau \to \infty$, and the right term drops out. If E is driven sinusoidally at frequency ω, we can solve for this easily, finding

$$v_0 e^{i\omega t} = \frac{qE_0}{i\omega m} e^{i\omega t}, \tag{5.1}$$

where we've used the '0' subscript to describe the amplitude of oscillating terms. This has the same linear dependence of velocity on electric field as magnetic inductance, though of course the coefficients and physical origin are completely different (and this breaks down as $\omega \to 0$, as the system will stop superconducting at some point). We make this more explicit by considering a wire made out of a superconducting kinetic inductor with length l, cross-sectional area A, and supercurrent density n_s, and describe the current density and voltage across it:

$$J_0 = n_s(2e)v_0 = \frac{2e^2 n_s}{i\omega m} E_0, \qquad V = \frac{i\omega m_e}{2e^2 n_s} \frac{l}{A} I \tag{5.2}$$

Thus the kinetic inductance L_{kin} is equal to $\frac{l}{A}\frac{m_e}{2e^2 n_s}$. There are two clear properties of the wire, then, that we can use to maximize the kinetic inductance: geometric dimensions and supercurrent density. The former is controlled in fabrication, by growing thin films, typically under 20 nm, and and writing the wires to be about 100 nm wide. The limitations to these dimensions come from the breakdown of superconducting behavior, and are discussed in the following sections. The inverse dependence on supercurrent density, can be understood by noting that the fewer charge carriers that are being excited, the greater the speed each has to travel at to achieve a given current. These low density superconductors can be achieved in a number of ways, include chains of SQUIDs [6], granular aluminum [31], and the approach we examine in this work, type-II superconductors. Titanium nitride, niobium titanium nitride and niobium nitride (NbN) the most typically used; in this work we focus on NbN.

Niobium nitride has been studied for decades, with Keskar [38] in 1974 describing sputtered NbN films with upper critical fields of up to 290 kOe and transition temperatures (T_c) of 17.3 K. Such high values of T_c are achieved by depositing above 600 °C on substrates such as MgO, which is nearly lattice matched to NbN. GaAs is latticed mismatched by 27%, and the arsenic begins to evaporate above 400 °C, both of which lead to T_c being reduced to 14.7 K on GaAs [54].

The fabrication of NbN nanowires was pioneered in the field of hot-electron bolometry, in which the narrow, thin superconducting films are meant to be easily turned normal, so that they are effective single electron sensors [30]. As we learned quickly, changing the application, and hence some of the fabrication techniques, can cause meaningful changes in results. The fabrication processes for bolometers typically involve depositing NbN on a bare substrate, and proceeding from there. By contrast, any resonators meant to be coupled with quantum dots will face other fabrication challenges. For example, the heterostructure will have a two-dimensional electron gas, which will need to be removed to prevent dissipation. For this reason, one focus has been developing techniques to put the resonator on a separate chip as the quantum dot, then connect them via indium bumps [78]. In recent year, there has also been increasing interest in using them as resonators for quantum computing purposes [80]. We present what we've learned about fabricating resonators in quantum-dot-compatible processes below.

5.1 SPUTTERING AND FILM TESTS

We sputter the NbN films in an AJA DC magnetron sputterer, with a 2" 99.999% Nb target at power 200 W, pressure 3 mTorr, argon flow of 50 sccm, and N_2 flow of about 5 sccm. The system has a load lock, cryopump, and base pressure of about 10^{-8} Torr. We sputter with the sample holder held at room temperature (through water cooling). We note that the most straightforward qubit-resonator devices sputter the NbN sheet onto a substrate partially covered in a electron beam or photo resist, due to the potential for damaging the heterostructure when etching the region where the quantum dot will be formed. The resists we work with cannot be heated above 180 °C, at which point there are no benefits from heating the substrate, so we are content to work at room temperature.

We perform regular characterizations of the T_c of films of NbN, in particular after opening the chamber or other maintenance. While we are largely satisfied at this time that our protocols ensure consistent results, we find that performing these measurements has allowed us to stay ahead of maintenance and other film issues.

To characterize films, we typically cut 4 mm square pieces of GaAs or high-resistivity silicon, perform a four-solvent clean, and then load them in the sputterer. Once sputtered, the film is glued to a PCB that has a RuOx thermometer from Lakeshore Cryotronics connected to it. Contact is made to the 4 corners using silver paint. We then measure the T_c by dipping the PCB into a helium dewar while measuring the sample's resistivity via a van der Pauw measurement. The temperature is monitored at the same time and varies as a function of the height of the PCB in the dewar. While this is clearly a noisy measurement, it suffices for our measurements, which are meant to determine differences between films over time and for different processes. It has been invaluable in discovering surprising degradations in process quality, and we find that the results we've gathered track those acquired by members of the Lukin group measuring similar samples in a cryogenic probe station.

We believe that many of the small shifts we see in T_c over time come from variations in sputter rate over time. While the rate is largely constant over short stretches of time, between a new target and a half-eroded target, the rate decreases by about 15%. Likewise, while small changes on the

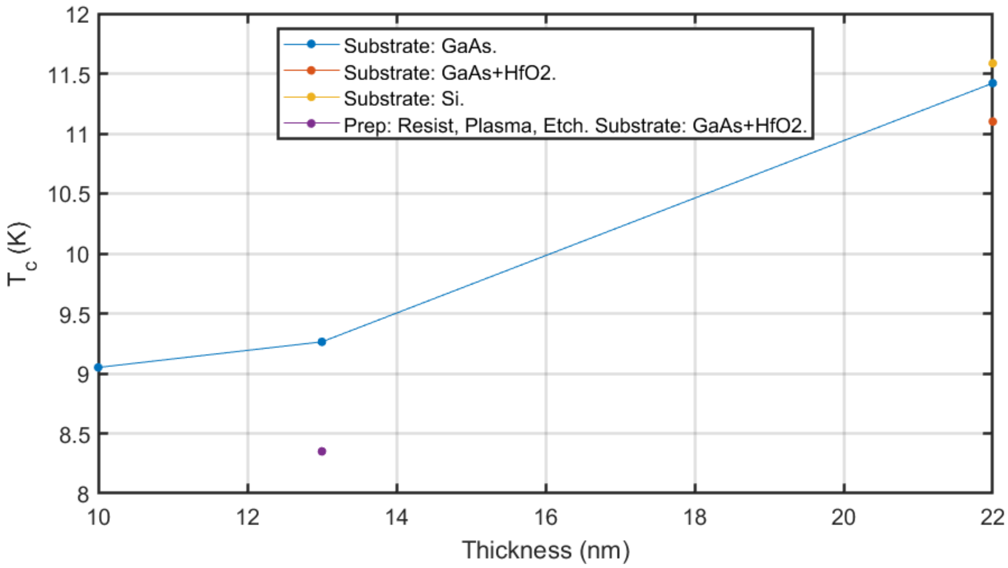

Figure 5.1: T_c measured for NbN films as a function of thickness, substrate, and preparation technique.

order of 10-20% in the rate of nitrogen gas flow into the chamber do not affect the rate, if the rate is changed by a factor of 4, the rate is diminished by about 20%. For this reason, we limit usage of the Nb target to thin films, to slow down erosion of the target, making recalibration necessary only rarely.

We find that after closing and pumping down the chamber, we see an increase in T_c of about 1 K by performing a titanium evaporation (using the electron beam evaporator in the system) at least an hour before. While it's not clear that it's necessary to do this each time a sample is loaded, we have adopted that procedure as a way to compensate for the frequent use of the chamber by other users. However, we do not see any correlation between the pressure sputtered at and the film quality. The Lukin group has performed extensive studies of different N_2 percentage and pressure, but have either found a reduction in T_c or no change. While we have seen enhanced T_c at higher powers, these seem to damage the target, leading to lower T_c over time.

With the T_c measurement method we use, transition width has not been a useful diagnostic, likely due to the noisiness of our measurements. In general, we have not found that resistivity is a useful metric. The resistivities we measure are higher than those found in the literature, but we believe that this is largely because those are typically sputtered at elevated temperatures.

The film tests have also been helpful in understanding the effects of processing on the devices. We performed a number of exploratory tests to get a sense of how T_c varied with substrate, thickness, and preparation method, shown in Fig. 5.1. Along with the clear decrease of T_c with a decrease in thickness, we also see negative effects from spinning the resist on the chip and adding ALD. However, later we did a more systematic test, cutting 7 samples from GaAs heterostructure, performed a varied set of etches, anneals, resist spins, ALD growth, and cleans on them, then sputtered 22 nm of NbN all at the same time. The measured T_c were all equal to within 0.2 K, approximately the sensitivity of the measurement. It's possible that they were more similar because they were sputtered at the same time, and thus lacked some of the variations discussed above, or it may be because these are on the thicker side, and the surface may be unimportant in such cases. Finally, it's possible that other parts of the fabrication process, more difficult to replicate – developing the resist, performing evaporation, have a far more meaningful effect.

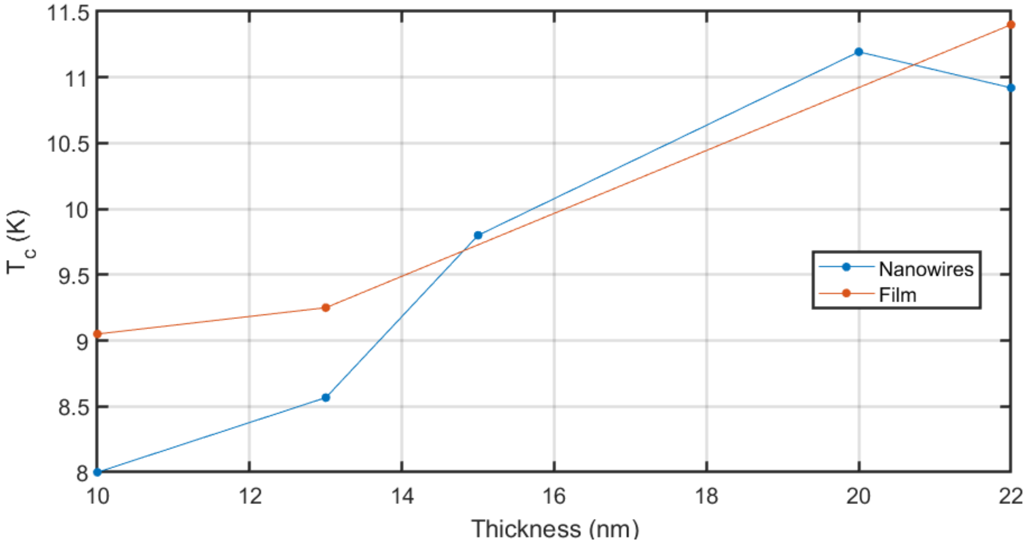

Figure 5.2: T_c is plotted for several nanowires in blue, with the T_c for films of the same thickness plotted in red.

5.2 NANOWIRES

To etch the films into nanowires with substantial kinetic inductance, we use a reactive-ion-etching process to define wires of width 100 or 150 nm. To test if the etch process has damaged them, we measure the T_c and compare to that of the bare films, the results of which are shown in Fig. 5.2. While the data at larger thicknesses tracks well, at lower thicknesses T_c is reduced by about 1 K. There could be a number of explanations for this, in particular that the etched samples measured here had undergone additional processing before film deposition in comparison to the bare films, and this may have degraded the surface. We note that T_c is comparable for samples of 100 and 150 nm, an indication that the etch is not damaging the film.

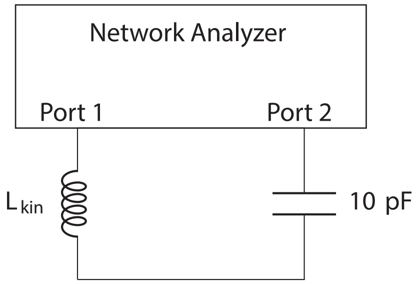

Figure 5.3: The circuit used to measure the inductance of the nanowire circuit.

5.3 INDUCTANCE MEASUREMENTS

To measure the inductance of the nanowires, we use a similar technique as that described in Annunziata et al. [1]. We use a PCB with a coplanar wave guide, and attach the inductor chip to the center along with a 10 pF capacitor. We find this value of capacitor offers a good trade off of being large enough to pull down the frequency to a workable level (about 100 MHz) while keeping the quality large enough to make it a sensitive detector of inductance, and so that parasitic capacitance in the circuit does not have a large effect. We use a series circuit instead of a parallel circuit because we found that having the sample directly connected to ground caused it to stay normal, presumably due to the flow of currents. Our system was flaky enough that we found it best to measure signals in transition rather than reflection, despite the increase in overhead of 2 coaxial lines instead of 1. We use two wire bonds, finding that adding more does not further decrease their effective inductance or improve the measured signal.

Because the supercurrent density increases as the temperature decreases, the kinetic inductance will also decrease. Since our inductance measurements are typically performed by dipping the sam-

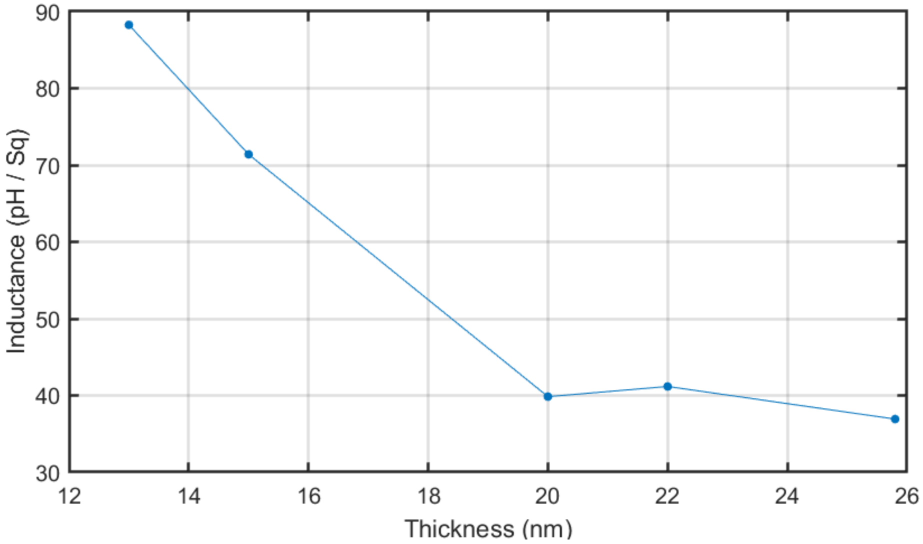

Figure 5.4: Measurements of Inductance per square for several widths and thicknesses of nanowire.

ple into liquid helium, and hence are at 4.2 K, while our qubit experiments are performed at about 50 mK, we are interested in determining their zero-temperature value. Following Annunziata et al. [1] and using Ginzburg-Landau theory, we can write $n_s(T) \approx n_s(0)(1 - T/T_c)$, for T near T_c, so that we can write

$$L_{\text{kin}}(0) = L_{\text{kin}}(T)(1 - T/T_c). \tag{5.3}$$

By combining T_c measurements with measurements of L, we can find L_0, which is plotted as a function of thickness in Fig 5.4. Based on simulations performed in Sonnet, these inductances are sufficient to achieve impedance around 2000 Ω for our resonators in the qubit design. We find that while the inductance (in units of pH-nm) does vary with thickness, it does not vary with nanowire width, another indication that our etch process is not damaging the film. Using Ginzburg-Landau theory, we expect that the room temperature resistivity should be linearly proportional to T_c. The

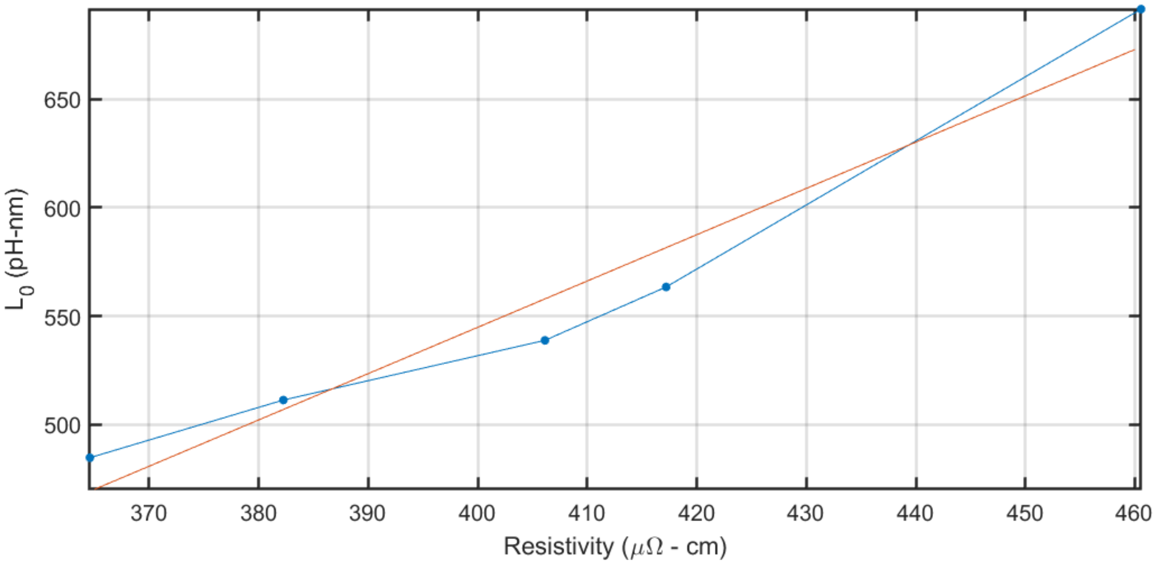

Figure 5.5: Plotting the zero-temperature inductance (calculated using a T_c measurement) versus the room temperature resistance. The red line is a linear fit to the data.

results are shown in Fig. 5.5, and we find that there is at least some correlation, so that it may be possible to predict inductance without performing RF measurements.

5.4 Contact Resistance

The thick oxide that NbN forms can cause issues when making contact to it. The contact resistance can grow to above $100\ k\Omega\ \mu\text{m}^2$. By etching it in dilute HF (BOE 5:1), and pumping it down in a thermal evaporator within minutes, we find that it is reduced to under $5\ \Omega\ \mu\text{m}^2$ (with the lower bounds limited by the measurement). This oxide is not self-limiting, and we've found that etching for 5 s is adequate within a day, but after 10 days, this does not etch the full oxide. BOE 5:1 does not measurably etch NbN (under a nanometer for 60 s of etching), so we have begun using 30 s BOE 5:1

etches before applying contacts, though it remains a good idea to limit the amount of time between depositing NbN and applying contacts.

These tests were performed using PMMA resist developed with MIBK:IPA 1:3. In general, TMAH-based developers will also etch the oxide, reducing the need for HF.

6

Conclusion

In the introduction to this thesis, I discussed what I saw as the most pressing issues limiting the growth of S-T_0 qubits as a platform for quantum computing at the start of my PhD, and how I tackled them during it. In this conclusion, I'd like to widen my perspective, both to other types of quantum-dot-based qubits and to the work that other groups are doing around the world that are pushing the field forward.

I listed these major issues as being nuclear magnetic field noise, charge noise, entangling gate, and fabrication and tuning of devices.

Our work in the Yacoby group on nuclear magnetic field noise substantially reduced it's ill-effects on coherence. Other groups working with S-T_0 qubits in GaAs have used dynamical decoupling to measure T_2 of close to a millisecond [53], indicating that there are a number of approaches that can reduce the impact of nuclear noise. In the world outside of S-T_0 qubits, the move toward isotopically-purified silicon has energized work into several varieties of single spin qubits, which have generally not been amenable to use in GaAs due to nuclear noise, but which show dramatically reduced coupling to charge due to their spin-like nature [96, 62]. An important phase of this research investigates new technologies for isotopically purifying silicon, to increase the supply to levels that allow many groups around the world to work in the field [56, 61, 36].

As research into silicon qubits has grown, it's become clear that levels of low-frequency charge noise in such qubits are comparable to those in GaAs [55, 105]. Excitingly, there has recently been a number of studies probing charge noise in silicon at higher frequencies [106, 15]. As this becomes more standard, it ought to provide a insight into the origins of charge noise.

There has also been a great deal of progress on entangling gates for quantum dots. In the Yacoby group, we performed an experiment on S-T_0 qubits that reduced the sensitivity of qubit to charge noise by performing the entanglement in the regime where it is primarily a spin (rather than charge) qubit [63], which increased the process fidelity of the entangling gate to 90%. In other groups, coherent coupling between spin qubits and resonators has been achieved, bringing us closer to using resonators to couple two S-T_0 qubits. Moreover, entangling gates have been demonstrated in a number of single-spin systems [97, 108, 101].

Some of the most exciting recent work in spin qubits has involved developing techniques that will be essential in scaling up to larger systems. Automated tuning has become possible in recent years, including the process of tuning quantum dots to the single-electron regime [2, 58, 48], tuning of tunnel coupling [95, 91], and measurement of the energy spectrum and location of charge transitions [11]. There has also been progress in implementing fast readout using parametric amplifiers [88] and tank circuits. Such technologies are crucial, because they dramatically speed up the time it takes to test new devices, which will be essential in finding optimized materials and architectures. There has been exploration of new gate architectures, such as those using overlapping gates, that are more easily tuned than the traditional stadium architecture, and simulations have been used to aid in designing such devices [107].

I would also add a new item to the list of limitations. Current architectures typically have large numbers of gates, which is ideal for prototype systems, where having the ability to explore a wide phase space is ideal. However, these systems, with up to 15 gates per qubit, and several RF lines, are not sustainable as we scale to larger numbers of qubits. Developing architectures in which multiple qubits can be controlled by each gate will be helpful, but will likely require not only accurate simulation, but also improved materials [51]. Another approach is to reduce the overhead associated with measurement, which typically requires several DC gates and ohmic contacts to form a sensing quantum dot, by replacing it with readout through a gate [17, 102] or resonator [45, 109]. Furthermore, as heating and cost become more central, considering the electronics that can be used will also be increasingly important [34, 73] . That we are adding items to the list of imminent challenges should be seen as a triumph rather than as a failure; it means that we are making progress and pushing into new regimes of study.

A

Rotating Frame for Singlet-Triplet Qubits

This appendix derives the equations for the evolution of the singlet-triplet in the rotating frame, as is used in Chapter 2 and Nichol et al. [63]. The Hamiltonian for the S-T_0 qubit is

$$\hat{H} = \hbar/2(\Delta B_z \sigma_x + J(\epsilon)\sigma_z) \tag{A.1}$$

This is our conventional Hamiltonian for S-T_0 qubits, but is non-standard for the rotating frame, as the static part of the Hamiltonian will be oriented mostly in the x-direction. While it would be ideal if the static part were solely the $\Delta B_z \sigma_x$ component, because $J(\epsilon)$ is strictly positive, if the static $J(\epsilon)$ were 0, we would not be able to turn on an oscillating $J = J_0 \cos(\omega t + \phi)$. Instead, we work at a value of $\epsilon = \epsilon_0$ where $J(\epsilon_0) \ll \Delta B_z$. Then, if we add a small oscillating drive ϵ_d, the Hamiltonian becomes

$$\hat{H} = \hbar/2 \Big[\Delta B_z \sigma_x + \left(J(\epsilon_0) + \frac{dJ}{d\epsilon}\Big|_{\epsilon_0} \epsilon_d \cos(\omega t + \phi) \right) \sigma_z \Big] \tag{A.2}$$

$$= \hbar/2 \Big[\Delta B_z \sigma_x + \left(J_0 + J_1 \cos(\omega t + \phi) \right) \sigma_z \Big]. \tag{A.3}$$

We've defined the terms J_0 and J_1 to simplify notation and ω and ϕ represent the frequency and phase of the applied drive, and can be chosen arbitrarily. While in the first chapter I discussed how the singlet-triplet qubit is notable in that it can be tuned to be primarily a spin or charge qubit, in the rotating frame, it is fundamentally a hybrid spin-charge qubit. We must be in the region where ΔB_z is dominant to enter the rotating frame. However, if we are in the region of ϵ where exchange is fully off and small changes to the gates do not cause the singlet orbital state to shift, we cannot turn on an oscillating J. Thus it is essential to consider the effects of both charge and magnetic noise for all rotating-frame experiments.

We now enter a rotated coordinate frame where the static splitting is in the direction of

$$\tilde{\sigma_x} = \Delta B_z/B\sigma_x + J_0/B\sigma_z = \tilde{\sigma_x} = \cos(\theta)\sigma_x + \sin(\theta)\sigma_z \tag{A.4}$$

where we've defined $B = \sqrt{\Delta B_z^2 + J_0^2}$ and $\tan(\theta) = J_0/\Delta B_z$. Then, we end up with the Hamiltonian

$$\hat{H} = \hbar/2\Big[\big(B + J_1\sin(\theta)\cos(\omega t + \phi)\big)\tilde{\sigma_x} + J_1\cos(\theta)\cos(\omega t + \phi)\tilde{\sigma_z}\Big]. \tag{A.5}$$

We see here that one penalty of working with larger values of J_0 for a given value of ΔB_z is that it reduces the effective size of the oscillating drive. Now, we can enter the rotating frame of $\hat{H}_r = \hbar\omega/2\tilde{\sigma_x}$. Using the standard unitary transformation, we now work with the Schrödinger equation

$$-i\hbar\frac{d\tilde{\psi}}{dt} = \hat{H}'\tilde{\psi}, \qquad \tilde{\psi} = \exp(i\omega/2\tilde{\sigma_x}t)\psi, \tag{A.6}$$

where

$$\begin{aligned}\hat{H}' =& \hbar/2\Big[\big(B + J_1\sin(\theta)\cos(\omega t + \phi) - \omega\big)\tilde{\sigma_x} \\ &+ \exp(i\omega/2\tilde{\sigma_x}t)J_1\cos(\omega t + \phi)\tilde{\sigma_z}\exp(-i\omega/2\tilde{\sigma_x}t)\Big].\end{aligned} \tag{A.7}$$

We can further simplify the second line of the equation:

$$\begin{aligned} & J_1\cos(\omega t+\phi)\big(I\cos(\omega t/2)+i\tilde{\sigma_x}\sin(\omega t/2)\big)\tilde{\sigma_z}\big(I\cos(\omega t/2)-i\tilde{\sigma_x}\sin(\omega t/2)\big) \qquad \text{(A.8)} \\ =& J_1\cos(\omega t+\phi)\big(\cos(\omega t)\tilde{\sigma_z}+\sin(\omega t)\tilde{\sigma_y}\big) \\ =& J_1/2\Big[\big(\cos(\phi)+\cos(\omega t+\phi)\big)\tilde{\sigma_z}+\big(\sin(\phi)-\sin(\omega t+\phi)\big)\tilde{\sigma_y}\Big]. \end{aligned}$$

Assuming that $\omega - B \ll \omega + B$, we can make the rotating-frame approximation, ignoring terms that oscillate at frequency 2ω. These oscillate far faster than the precession frequencies remaining in the Hamiltonian, $J_1/2$ and $B-\omega$, so we can safely treat them as their average value of 0. We use this same analysis to assume that the term $J_1\sin(\theta)\cos(\omega t+\phi)$ in (A.7) can be averaged to 0. Then, the equation becomes

$$\hat{H}' = \hbar/2\Big[(B-\omega)\tilde{\sigma_x}+J_1/2\left(\cos(\phi)\tilde{\sigma_z}+\sin(\phi)\tilde{\sigma_y}\right)\Big]. \qquad \text{(A.9)}$$

We'll consider only $\phi = 0$ for the remainder of this section.

Next we include noise in this model. We express B as a combination of its components' mean values and fluctuating noise terms:

$$\begin{aligned}
B &= \sqrt{(\overline{\Delta B_z} + \delta\Delta B_z)^2 + (\overline{J_0} + \delta J_0)^2}. \\
&\approx \sqrt{\overline{B}^2 + 2\overline{\Delta B_z}\delta\Delta B_z + 2\overline{J_0}\delta J_0} \\
&\approx \overline{B} + \overline{\Delta B_z}\delta\Delta B_z/\overline{B} + \overline{J_0}\delta J_0/\overline{B} \\
&= \overline{B} + \delta\Delta B_z\cos(\theta) + \delta J_0 \sin(\theta). \qquad \text{(A.10)}
\end{aligned}$$

We've kept only the first order error terms, and we use $\tan(\theta) = \overline{J_0}/\overline{B}$, as in (A.4), but now having used the mean values for the splittings to define the angle. The total noise is thus

$$\delta B = \delta\Delta B_z\cos(\theta) + \delta J_0 \sin\theta. \qquad \text{(A.11)}$$

Now, we will start considering Rabi and Ramsey experiments. In both Ramsey and Rabi experiments, we start by loading a $|\tilde{+}\rangle$ state, the ground state when J_1 is off. Because we do not perform any dynamical decoupling, the noise is effectively quasistatic.

For the Rabi, we use the pulse sequence shown in Fig. 2.2**e**: we turn on J_1 for the entire experiment, and set $\omega = B$, so we evolve under the Hamiltonian

$$\hat{H}' = \hbar/2\Big[\delta B\cos(\theta)\tilde{\sigma_x} + (\overline{J_1} + \delta J_1)\cos(\theta)/2\tilde{\sigma_z}\Big]. \qquad \text{(A.12)}$$

We define the magnitude of the splitting for this Hamiltonian as Ω, and solve for amount of noise:

$$
\begin{aligned}
\Omega &= \sqrt{(\overline{J_1} + \delta J_1)^2 \cos^2(\theta)/4 + (\delta B \cos(\theta))^2} \\
&\approx \cos(\theta)\big((\overline{J_1} + \delta J_1)/2 + \frac{\delta B^2}{\overline{J_1}}\big). \\
\delta\Omega &= \cos(\theta)\big(\delta J_1/2 + \frac{\delta B^2}{\overline{J_1}}\big)
\end{aligned}
\tag{A.13}
$$

Thus, in this experiment, we oscillate at a rate $\overline{J_1}\cos\theta$ and dephase at the rate $\delta\Omega$. We note that our goal in the experiment shown in Fig. 2.3**b** in Chap. 2 is to measure $\delta\Delta B_z$, but in this experiment we have a complicated dependence on it.

For the Ramsey experiment, we use the pulse sequence shown in Fig. 2.2**c**: first, turn on J_1 at a frequency ω offset from B by Δ to perform a $\pi/2\tilde{\sigma_z}$ pulse, putting the qubit in the $\psi_{y,+} = \frac{1}{\sqrt{2}}(|0\rangle + i|1\rangle)$ state. Then, we turn J_1 off and let the qubit evolve under the Hamiltonian

$$\hat{H}' = \hbar/2(\Delta + \delta B)\tilde{\sigma_x} \tag{A.14}$$

for time t. Finally, we read out by again turning on J_1 for a $\pi/2\tilde{\sigma_z}$ pulse. In this case, while there is dephasing during the $\pi/2$ preparation and readout pulses, it is the same for all evolution times. Thus, $T_2^* = \frac{\sqrt{2}}{\delta B}$. For the experiment discussed in Fig. 2.3 in Chap. 2, we are only interested in measuring $\delta\Delta B_z$. By examining (A.11) we see that to do so with this Ramsey experiment, we must be careful to set J_0 low for $\delta B \approx \delta\Delta B_z$. In that experiment, we made sure of that by varying ϵ_0 to reduce J_0 until T_2^* stopped increasing.

Again, this experiment is useful for demonstrating how well we've estimated ΔB_z. For maximizing gate fidelities, however, it's typically better to do Rabi-type experiments that will reduce the effects of residual fluctuations in ΔB_z. This is what we did in our group's 2017 paper on entangling two S-T_0 qubits in a large magnetic field gradient, "High-fidelity entangling gate for double-quantum-dot spin qubits" [63].

Finally, a quick note for my own understanding to quantitatively explain the difference between the experiment we use to measure ΔB_z using DC pulses and the Ramsey experiment just described. In the ΔB_z experiment, shown in Fig. 2.2**a**, we load a $|0\rangle$, let the qubit evolve under $\Delta B_z \sigma_x$ for time t, then measure. The only difference with the rotating-frame Ramsey is that in the Ramsey case we load a $|+\rangle$, then prepare a $|0\rangle$ by performing a $\pi/2\tilde{\sigma_y}$ pulse by turning on $J_1 \sin(Bt)$ for the appropriate time, and perform the same pulse for readout before measuring. (I note that here I've changed the phase of the drive to perform a $\pi_y/2$ pulse instead of $\pi_z/2$, but this does not change anything). While the state evolution is the same for the two experiments, the readout is different. In general, in rotating-frame experiments, we are measuring in the basis of the static splitting; in this case, the $|\tilde{+}\rangle$ and $|\tilde{-}\rangle$ states. These states are not affected by the rotating-frame transformation, so that, e.g.

$$|\langle\tilde{+}|\tilde{\psi}\rangle| = |\langle e^{-i\omega t/2\tilde{\sigma_x}}\tilde{+}|\psi\rangle| = |\langle\tilde{+}|\psi\rangle|, \tag{A.15}$$

so our experimental measurements are those we expect from the calculated $\tilde{\psi}$. However, for the static experiment, we would be measuring in the $|0\rangle$ and $|1\rangle$ states. In this case,

$$|\langle 0|\tilde{\psi}\rangle| = |\langle e^{-i\omega t/2\tilde{\sigma_x}} 0|\psi\rangle| \neq |\langle 0|\psi\rangle|. \tag{A.16}$$

So while we have $\tilde{\psi}$ is largely static, rotating at only Δ, the measurement basis is rotating at ω.

B

Measuring Charge Noise using Hahn Echo Data

In this appendix, we will derive the relationship between a singlet-triplet qubit's T_2, the dynamically decoupled dephasing time, and the power spectral density (PSD) of the voltage noise in the system. This technique is applied in Dial et al. [20], and is a useful metric for understanding the amounts of high frequency charge noise affecting different qubits.

B.1 Dependence of T_2 on J

The initial derivation follows that provided in Cywiński et al. [18]. For Gaussian noise, we expect decay to follow the form $W(t) = e^{-\chi(t)}$, where

$$\chi(t) = \int_0^\infty \frac{d\omega}{2\pi} S(\omega)|\tilde{f}(t;\omega)|^2 = \int_0^\infty \frac{d\omega}{\pi} S(\omega)\frac{F(\omega t)}{\omega^2}. \tag{B.1}$$

The filter function describes the effect of the pulse sequence on the qubit state, and is defined as

$$F(\omega t) = \frac{1}{2}\left|\Sigma_{k=0}^{n}(-1)^k(e^{i\omega t_{k+1}} - e^{i\omega t_k})]\right|^2, \tag{B.2}$$

where t_k represents the times at which π pulses are performed. For a Hahn echo, it simplifies to $F(\omega t) = 8\sin^2(\omega t/4)$.

For the remainder of this note, we will consider only power law noise, $S(\omega) = S_\omega/\omega^\beta$ and $0 \leq \beta \leq 3$. We will start by considering a PSD representing phase noise on the qubit, where $S(\omega)$ has units of $\phi^2/(\mathrm{rad/s})$. It's defined as in [18] as

$$S(\omega) = \int_{-\infty}^{\infty} e^{i\omega t} S(t)dt, \tag{B.3}$$

where $S(t)$ is the two point correlation function,

$$S(t_1 - t_2) = \langle \upsilon(t_1)\upsilon(t_2) \rangle \tag{B.4}$$

and υ represents the noise term in the qubit's Hamiltonian,

$$\hat{H} = \frac{1}{2}[\Omega + \upsilon]\sigma_z. \tag{B.5}$$

We start by converting units between $S(\omega)$ and $S(f)$ (which we will ultimately use to quote the noise level). Unitswise, $S(f) = 2\pi S(\omega)$.

$$S_f/f^\beta = S_f/(\omega/(2\pi))^\beta = 2\pi S_\omega/\omega^\beta. \tag{B.6}$$

$$S_f = (2\pi)^{1-\beta} S_\omega \tag{B.7}$$

Next, because we are interested in the charge noise, we will write this in terms of the voltage noise bath affecting the qubit. To convert S_w to $S_{\epsilon,\omega}$, the voltage PSD, normalized as effective noise from a nearby gate, we substitute in the Hamiltonian for the qubit undergoing exchange into (B.5):

$$\hat{H} = \frac{1}{2}[\Omega + \upsilon(t)]\sigma_z = \frac{1}{2}(J_\omega + \frac{dJ_\omega}{d\epsilon}\delta\epsilon)\sigma_z, \tag{B.8}$$

so we can write $\upsilon = \frac{dJ_\omega}{d\epsilon}\delta\epsilon$. Then, through examination of (B.6),

$$\frac{1}{2}\left(\frac{dJ_\omega}{d\epsilon}\right)^2 S_{\epsilon,\omega} = S_\omega, \tag{B.9}$$

where the factor of 1/2 stems from (B.3) being integrated being only from 0 to ∞ for S_ϵ.

Now, we use (B.9) and (B.6), to write $S_{\epsilon,f}$ in terms of S_ω:

$$S_{\epsilon,f} = 2(2\pi)^{1-\beta}\left(\frac{dJ_\omega}{d\epsilon}\right)^{-2} S_\omega \tag{B.10}$$

This term has units of $\mathrm{V}^2/\mathrm{Hz}^{1-\beta}$. Next, we turn to (B.1). For power-law noise, there is a closed solution for $\chi(t)$ for a Hahn echo pulse (and for small pulse numbers for some other sequences):

$$\chi_{\mathrm{HE}}(t) = \frac{1}{\pi}\sin(\frac{\pi\beta}{2})\Gamma[-1-\beta]S_\omega(1-2^{1-\beta})t^{1+\beta}. \tag{B.11}$$

Since $t = T_2$ when $\chi(t) = 1$, we can write

$$\begin{aligned} T_2^{1+\beta} =& \pi\left(\sin(\frac{\pi\beta}{2})\Gamma[-1-\beta]S_\omega(1-2^{1-\beta})\right)^{-1} \\ &= (2\pi)^{-\beta}\left(\sin(\frac{\pi\beta}{2})\Gamma[-1-\beta]S_{\epsilon,f}(1-2^{1-\beta})\frac{dJ_f}{d\epsilon}^2\right)^{-1} \\ &= \left(\eta(\beta)S_{\epsilon,f}\frac{dJ_f}{d\epsilon}^2\right)^{-1}, \end{aligned} \tag{B.12}$$

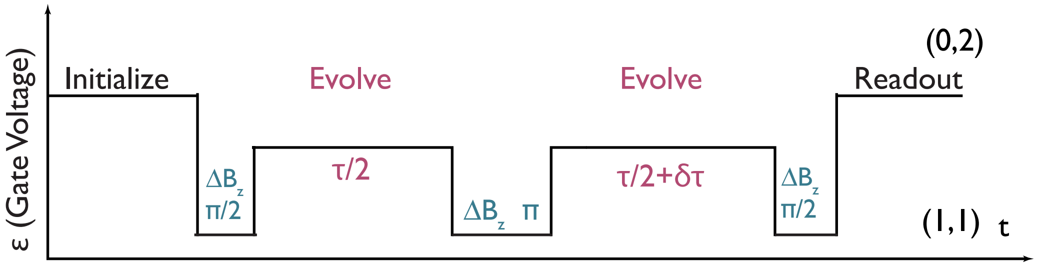

Figure B.1: Pi pulse

.

where we have now defined

$$\eta(\beta) = (2\pi)^\beta \sin(\frac{\pi\beta}{2})\Gamma[-1-\beta](1-2^{1-\beta}). \tag{B.13}$$

As a side note, Γ is infinite at integers, but if we perform the integral for each integral value of β, they are solvable:

$$\begin{aligned} \beta = 0: &\quad T_2 = \frac{dJ_f}{d\epsilon}/S_{\epsilon,f} \\ \beta = 1: &\quad T_2 = \sqrt{\frac{(2\pi)^3}{\log(2)S_{\epsilon,f}}}\frac{dJ_f}{d\epsilon} \\ \beta = 2: &\quad T_2 = 2\pi\sqrt[3]{12\frac{dJ_f}{d\epsilon}^2/S_{\epsilon,f}}. \end{aligned} \tag{B.14}$$

B.2 FITTING DATA

To measure $S_{\epsilon,f}$, we measure T_2 as a function of $\frac{dJ_f}{d\epsilon}$, and fit (B.12).

To do this, we first, take Hahn echo data at a variety of $\frac{dJ}{d\epsilon}$ by varying ϵ. We use the pulse sequence shown in Figure B.1. Within each data set we vary τ, the total evolution time, and $\delta\tau$, the difference in evolution time before and after the pi pulse. We fit each two-dimensional data set using the following function:

$$\begin{aligned} A(\tau, \delta\tau) =& y_{0,i} + A_0 \cos(\omega_i \delta\tau + \phi_i) \exp(-((\delta\tau - \tau_{0,i})/T_2^*)^2) \times \exp(-\tau/T_2)^{1+\beta} \\ &+ A_{0,f} \cos(\omega_i \delta\tau + \phi_{f,i}) \exp(-((\tau/2 + \delta\tau)/T_2^*)^2) \end{aligned} \tag{B.15}$$

where the terms with i subscripts are allowed to vary for different values of τ. The terms with f subscripts represent the "fish-like" shape the data takes at short times: If $\tau/2 \lesssim T_2^*$, then we will see in the data the initial decay of amplitude over T_2^* that wasn't echoed away (due to pulse imperfections) as well as the refocusing that occurs with the echo pulse.

After analyzing the data sets for all values of ϵ, we can examine the values of β fit. In Dial et al. [20], β was nearly constant for different values of ϵ, allowing us to conclude that we have power law noise. We then take the mean of the values of β to get β_0, and perform a linear fit $T_2^{-(1+\beta_0)} = p(1)(dJ/d\epsilon)^2 + p(2)$. We can read off the equation for (B.12) to see that $p(1) = \eta(\beta)S_\epsilon$, so knowing β, it is simple to find S_ϵ. The offset allows for background noise that doesn't depend on J, for instance (to first order) tunneling noise or magnetic noise.

To find $\frac{dJ}{d\epsilon}$, we measure $J(\epsilon)$ across the relevant range of ϵ, subtracting off ΔB_z in quadrature, then fit to an exponential, as discussed in Chapter 4. We then use the fit to calculate $\frac{dJ}{d\epsilon}$.

The data that we fit has units of $[T_2] = \mu$s and $[\frac{dJ}{d\epsilon}]$ =MHz/μV. To get the units in V^2/Hz$^{1-\beta}$, we write the fit equation with them having units of s and Hz / V, respectively.

$$
\begin{aligned}
(T_2(\mu\mathrm{s}))^{-(1+\beta)} &= \mathrm{p}(1)\left(\frac{\mathrm{dJ(MHz)}}{\mathrm{d}\epsilon(\mu\mathrm{V})}\right)^2 + \mathrm{p}(2) \\
(T_2(s))^{-(1+\beta)} &= p(1) * 10^{-18+6\beta}\left(\frac{dJ(\mathrm{Hz})}{d\epsilon(\mathrm{V})}\right)^2 + p(2) \qquad \text{(B.16)}
\end{aligned}
$$

Combining this with (B.12), this is

$$p(1) * 10^{-18+6\beta} = \eta(\beta)S_\epsilon(\mathrm{V}^2/\mathrm{Hz}^{1-\beta}). \qquad \text{(B.17)}$$

The exact term for comparison with equations is

$$S_\epsilon = p(1) * 10^{-18+6\beta}(2\pi)^{-\beta}\left(\sin(\frac{\pi\beta}{2})\Gamma[-1-\beta](1-2^{1-\beta})\right)^{-1} \qquad \text{(B.18)}$$

We note that in Dial et al. [20], an incorrect equation was given, which reduced S_ϵ by a factor of 2π, thus reducing the amount of noise at 1 MHz by $\sqrt{2\pi} \approx 2.5$, so in fact the amount of noise at 1 MHz should have been 0.5 nV/$\sqrt{\text{Hz}}$, not 0.2 nV/$\sqrt{\text{Hz}}$.

B.3 Quick Techniques to Estimate Noise

These data sets can take days to take in full, but while the data is coming in, you may want to get a sense of how much noise the system has compared to previous systems by comparing T_2 as a function of J for the two. Let's see how rigorous that is.

We will assume that we have $J = J_0 \exp(\epsilon/\epsilon_0)$, $J' = J/\epsilon_0$. We'll assume that β is the same across samples a and b. In that case, the same J implies the same $\frac{dJ}{d\epsilon}$, and by referencing (B.12):

$$(T_{2,a}/T_{2,b})^{1+\beta} = \frac{S_{\epsilon,b}}{S_{\epsilon,a}} \frac{\epsilon_{0,a}^2}{\epsilon_{0,b}^2} \tag{B.19}$$

Our usual shorthand, noise at 1 MHz, is proportional to the square root of S_ϵ:

$$N_b/N_a = (T_{2,a}/T_{2,b})^{(1+\beta)/2} \frac{\epsilon_{0,b}}{\epsilon_{0,a}} \tag{B.20}$$

This is pretty close to a linear scaling with T_2 for $\beta \approx 0.7$.

C

Ohmic Fabrication

C.1 OHMICS

Summary of section:

1. **Ohmics don't work if too much time passes between mesa etch and ohmic deposition.** Solution: Can deposit ohmics within 12 hours, but for minimum contact resistance with any amount of time passing, dip sample in BOE 5:1 for 10 s.
2. **Ohmics don't work if graphite susceptor bad.** Bare silicon wafer works well.

3. **Ohmics don't work with material 4 mm from edge.** Solution: move to at least 6 mm from edge.
4. Ohmic contact can be checked by measuring resistance in room temperature probe station with light and off.

To make contact to the 2DEG, we use a Ni/Au/Ge/Ni/Au stack, heated above eutectic temperature of Au/Ge.

Issues with ohmics seem to crop up periodically. For my first few years, we used an image-reversal photo process and did not do any cleaning between developing the ohmic pattern and depositing metal. I began having issues with the ohmics not making good contact; they would conduct at room temperature but freeze out at 4 K. Mike Manfra's student John Watson suggested that we try to do the mesas and ohmics within about 12 hours, and this fixed the issue.

In the current recipe, the ohmics are one of the first steps out of many, so it makes sense to be certain that they work before continuing. We have not found that visual inspection is helpful (unless the sample has been so underheated that the metal didn't melt). However, wire bonding and cooling to 4 K can introduce grime onto the chip and leave wire bond residue, while cutting of a piece is time consuming and wastes material. Instead, after noting that the "bad" ohmics would increase in resistance immediately after the probe was closed, we began testing the ohmics in a room temperature probe station, comparing the resistance with the light on and off, and have thus far had 100% success in determining if the ohmics will work. That said, it unsurprisingly is not effective at differentiating excellent from merely good contacts. The first chart below shows data from a case in which we performed tests because two weeks passed between etching mesas and depositing ohmics. we see that the numbers vary only slightly as a function of the maximum temperature and time we sit at it. The reported resistances are the average of 3 two-probe measurements between three different ohmic contacts

Temp (C)	Time (s)	Light (Ω)	Dark (Ω)	Cold (Ω)	Ratio D-L
445	75	3480	4260	72	1.2
445	85	2500	4530	60	1.8
450	65	3000	5130	55	1.7
450	75	2560	4340	50	1.7
455	60	3550	4500	100	1.26
460	55	3450	4130	65	1.2

In the second chart, we show the results from two fabrication runs where there are some issues with ohmics. In the first run (the first four measurements), no ohmics worked cold. We think the issue is that the sample was taken from too close to the edge of the wafer. We can see that both the light and dark resistances are elevated, but the dark in particular (the ohmics pattern is the same as in the previous test). We were able to diagnose this issue by noting that the resistances did not vary meaningfully with time and temperature, but the ohmics that were on the part of the chip more central on the wafer were lower in resistance. In the second run, we took samples from a several millimeters further in on the wafer, and here we can see that for poorly annealed sample (the fifth in the list), where it's light and dark resistances are close to as bad as those that didn't conduct cold, indeed has a high contact resistance. In either case, we see that there are clear signs differentiating good and bad ohmics.

Temp (C)	Time (s)	Light (Ω)	Dark (Ω)	Cold (Ω)	Ratio D-L
440	60	7920	18,400	Inf	2.3
440	65	3650	14,500	Inf	4
450	75	5900	118,000	Inf	20
460	60	4350	59,000	Inf	13.5
440	60	5700	15400	875	2.7
450	60	3640	7860	210	2.15
450	75	3360	5310	70	1.6
460	60	3090	5660	100	1.8

At another point, the ohmics stopped working with no apparent process change. After a useful conversation with members of Reilly Group, we began to suspect our susceptor, the graphite wafer the sample sits on inside the rapid thermal processor (RTP). This is made of graphite, but according to the person who runs the tool, it had become infused with oxygen due to the practices of other users, and this may have affected its thermal conductivity. In conversation with Jingyee Chee of the Ham group, who was also having issues, we changed to a silicon wafer as the base, and have not had such issues since.

As we changed the recipe over to use electron beam lithography, we found that there were a few issues with the cleaning step. HCl:H_2O seemingly caused the resist to harden, as liftoff was not possible: all the gold stayed affixed to the surface. Using HNO_3 worked, but if dipped for more than 2 -3 s, all of the resist will lift off. We have settled on using BOE 5:1, which seems to be able to etch all the oxide even with long gaps between the mesa etch and ohmics deposition. PMMA is also stable in it, with no issues after a full minute of etching. It seems to not etch GaAs. Performing an etch test, we see that 1.2 nm of ‘GaAs’ is etched after 10 s, and 1.5 nm after 50 s, suggesting that it is only etching the oxide. Furthermore, we have achieved excellent ohmic contacts with a 30 s etch.

References

[1] A. J. Annunziata, D. F. Santavicca, L. Frunzio, G. Catelani, M. J. Rooks, A. Frydman, and D. E. Prober. Tunable superconducting nanoinductors. *Nanotechnology*, 21(44):445202, 2010. doi:10.1088/0957-4484/21/44/445202.

[2] T. A. Baart, P. T. Eendebak, C. Reichl, W. Wegscheider, and L. M. K. Vandersypen. Computer-automated tuning of semiconductor double quantum dots into the single-electron regime. *Applied Physics Letters*, 108(21):213104, May 2016. doi:10.1063/1.4952624.

[3] G. Balasubramanian, P. Neumann, D. Twitchen, M. Markham, R. Kolesov, N. Mizuochi, J. Isoya, J. Achard, J. Beck, J. Tissler, V. Jacques, P. R. Hemmer, F. Jelezko, and J. Wrachtrup. Ultralong spin coherence time in isotopically engineered diamond. *Nature Materials*, 8(5): 383–387, May 2009. doi:10.1038/nmat2420.

[4] C. Barthel, D. J. Reilly, C. M. Marcus, M. P. Hanson, and A. C. Gossard. Rapid Single-Shot Measurement of a Singlet-Triplet Qubit. *Physical Review Letters*, 103(16):160503, Oct. 2009. doi:10.1103/PhysRevLett.103.160503.

[5] C. W. J. Beenakker. Theory of Coulomb-blockade oscillations in the conductance of a quantum dot. *Physical Review B*, 44(4):1646, 1991. URL `http://journals.aps.org/prb/abstract/10.1103/PhysRevB.44.1646`.

[6] M. T. Bell, I. A. Sadovskyy, L. B. Ioffe, A. Y. Kitaev, and M. E. Gershenson. Quantum Superinductor with Tunable Nonlinearity. *Physical Review Letters*, 109(13), Sept. 2012. doi:10.1103/PhysRevLett.109.137003.

[7] P.-M. Billangeon, J. S. Tsai, and Y. Nakamura. Scalable architecture for quantum information processing with superconducting flux qubits based on purely longitudinal interactions. *Physical Review B*, 92(2):020509, July 2015. doi:10.1103/PhysRevB.92.020509.

[8] A. Blais, R.-S. Huang, A. Wallraff, S. Girvin, and R. Schoelkopf. Cavity quantum electrodynamics for superconducting electrical circuits: An architecture for quantum computation. *Physical Review A*, 69(6), June 2004. doi:10.1103/PhysRevA.69.062320.

[9] H. Bluhm, S. Foletti, D. Mahalu, V. Umansky, and A. Yacoby. Enhancing the Coherence of a Spin Qubit by Operating it as a Feedback Loop That Controls its Nuclear Spin Bath. *Physical Review Letters*, 105(21):216803, Nov. 2010. doi:10.1103/PhysRevLett.105.216803.

[10] H. Bluhm, S. Foletti, I. Neder, M. Rudner, D. Mahalu, V. Umansky, and A. Yacoby. Dephasing time of GaAs electron-spin qubits coupled to a nuclear bath exceeding 200 Ms. *Nature Physics*, 7(2):109–113, Feb. 2011. doi:10.1038/nphys1856.

[11] T. Botzem, M. D. Shulman, S. Foletti, S. P. Harvey, O. E. Dial, P. Bethke, P. Cerfontaine, R. P. G. McNeil, D. Mahalu, V. Umansky, A. Ludwig, A. Wieck, D. Schuh, D. Bougeard, A. Yacoby, and H. Bluhm. Tuning Methods for Semiconductor Spin Qubits. *Physical Review Applied*, 10(5):054026, Nov. 2018. doi:10.1103/PhysRevApplied.10.054026.

[12] C. Buizert, F. H. L. Koppens, M. Pioro-Ladrière, H.-P. Tranitz, I. T. Vink, S. Tarucha, W. Wegscheider, and L. M. K. Vandersypen. Insitu reduction of charge noise in GaAs/$\mathrm{Al_xGa_{1-x}}$As schottky-gated devices. *Physical Review Letters*, 101(22), Nov. 2008. doi:10.1103/PhysRevLett.101.226603.

[13] H. Carmichael. *An Open Systems Approach to Quantum Optics: Lectures Presented at the Université Libre de Bruxelles, October 28 to November 4, 1991*. Lecture Notes in Physics Monographs. Springer-Verlag, Berlin Heidelberg, 1993. ISBN 978-3-662-13926-4. URL `//www.springer.com/us/book/9783662139264`.

[14] P. Cerfontaine, T. Botzem, S. S. Humpohl, D. Schuh, D. Bougeard, and H. Bluhm. Feedback-tuned noise-resilient gates for encoded spin qubits. *arXiv:1606.01897 [cond-mat, physics:quant-ph]*, June 2016. URL `http://arxiv.org/abs/1606.01897`.

[15] K. W. Chan, W. Huang, C. H. Yang, J. C. C. Hwang, B. Hensen, T. Tanttu, F. E. Hudson, K. M. Itoh, A. Laucht, A. Morello, and A. S. Dzurak. Assessment of a Silicon Quantum Dot Spin Qubit Environment via Noise Spectroscopy. *Physical Review Applied*, 10(4):044017, Oct. 2018. doi:10.1103/PhysRevApplied.10.044017.

[16] W. Coish and D. Loss. Hyperfine interaction in a quantum dot: Non-Markovian electron spin dynamics. *Physical Review B*, 70(19), Nov. 2004. doi:10.1103/PhysRevB.70.195340.

[17] J. Colless, A. Mahoney, J. Hornibrook, A. Doherty, H. Lu, A. Gossard, and D. Reilly. Dispersive Readout of a Few-Electron Double Quantum Dot with Fast rf Gate Sensors. *Physical Review Letters*, 110(4), Jan. 2013. doi:10.1103/PhysRevLett.110.046805.

[18] L. Cywiński, R. Lutchyn, C. Nave, and S. Das Sarma. How to enhance dephasing time in superconducting qubits. *Physical Review B*, 77(17), May 2008. doi:10.1103/PhysRevB.77.174509.

[19] J. H. Davies. *The Physics of Low-Dimensional Semiconductors: An Introduction*. Cambridge University Press, 1998. ISBN 978-0-521-48491-6.

[20] O. Dial, M. Shulman, S. Harvey, H. Bluhm, V. Umansky, and A. Yacoby. Charge Noise Spectroscopy Using Coherent Exchange Oscillations in a Singlet-Triplet Qubit. *Physical Review Letters*, 110(14), Apr. 2013. doi:10.1103/PhysRevLett.110.146804.

[21] N. Didier, J. Bourassa, and A. Blais. Fast Quantum Nondemolition Readout by Parametric Modulation of Longitudinal Qubit-Oscillator Interaction. *Physical Review Letters*, 115(20): 203601, Nov. 2015. doi:10.1103/PhysRevLett.115.203601.

[22] S. J. Elman, S. D. Bartlett, and A. C. Doherty. Long-range entanglement for spin qubits via quantum Hall edge modes. *Physical Review B*, 96(11):115407, Sept. 2017. doi:10.1103/PhysRevB.96.115407.

[23] K. Eng, T. D. Ladd, A. Smith, M. G. Borselli, A. A. Kiselev, B. H. Fong, K. S. Holabird, T. M. Hazard, B. Huang, P. W. Deelman, I. Milosavljevic, A. E. Schmitz, R. S. Ross, M. F. Gyure, and A. T. Hunter. Isotopically enhanced triple-quantum-dot qubit. *Science Advances*, 1(4): e1500214, May 2015. doi:10.1126/sciadv.1500214.

[24] S. Fallahi, J. R. Nakamura, G. C. Gardner, M. M. Yannell, and M. J. Manfra. Impact of silicon doping on low-frequency charge noise and conductance drift in GaAs/$\mathrm{Al_xGa_{1-x}As}$ nanostructures. *Physical Review Applied*, 9(3):034008, Mar. 2018. doi:10.1103/PhysRevApplied.9.034008.

[25] C. Ferrie, C. E. Granade, and D. G. Cory. How to best sample a periodic probability distribution, or on the accuracy of Hamiltonian finding strategies. *Quantum Information Processing*, 12(1):611–623, Jan. 2013. doi:10.1007/s11128-012-0407-6.

[26] S. Foletti, H. Bluhm, D. Mahalu, V. Umansky, and A. Yacoby. Universal quantum control of two-electron spin quantum bits using dynamic nuclear polarization. *Nature Physics*, 5(12): 903–908, Dec. 2009. doi:10.1038/nphys1424.

[27] S. E. Foletti. *Manipulation and Coherence of a Two-Electron Logical Spin Qubit Using GaAs Double Quantum Dots*. PhD thesis, Harvard University, 2010.

[28] J. Gambetta, A. Blais, M. Boissonneault, A. A. Houck, D. I. Schuster, and S. M. Girvin. Quantum trajectory approach to circuit QED: Quantum jumps and the Zeno effect. *Physical Review A*, 77(1):012112, Jan. 2008. doi:10.1103/PhysRevA.77.012112.

[29] K. Geerlings, S. Shankar, E. Edwards, L. Frunzio, R. J. Schoelkopf, and M. H. Devoret. Improving the quality factor of microwave compact resonators by optimizing their geometrical parameters. *Applied Physics Letters*, 100(19):192601, 2012. doi:10.1063/1.4710520.

[30] G. N. Gol'tsman, O. Okunev, G. Chulkova, A. Lipatov, A. Semenov, K. Smirnov, B. Voronov, A. Dzardanov, C. Williams, and R. Sobolewski. Picosecond superconducting single-photon optical detector. *Applied Physics Letters*, 79(6):705, 2001. doi:10.1063/1.1388868.

[31] L. Grünhaupt, U. von Lüpke, D. Gusenkova, S. T. Skacel, N. Maleeva, S. Schlör, A. Bilmes, H. Rotzinger, A. V. Ustinov, M. Weides, and I. M. Pop. An argon ion beam milling process for native AlOx layers enabling coherent superconducting contacts. *Applied Physics Letters*, 111(7):072601, Aug. 2017. doi:10.1063/1.4990491.

[32] E. L. Hahn. Spin Echoes. *Physical Review*, 80(4):580–594, Nov. 1950. doi:10.1103/PhysRev.80.580.

[33] S. P. Harvey, C. G. L. Bøttcher, L. A. Orona, S. D. Bartlett, A. C. Doherty, and A. Yacoby. Coupling two spin qubits with a high-impedance resonator. *Physical Review B*, 97(23): 235409, June 2018. doi:10.1103/PhysRevB.97.235409.

[34] J. M. Hornibrook, J. I. Colless, I. D. Conway Lamb, S. J. Pauka, H. Lu, A. C. Gossard, J. D. Watson, G. C. Gardner, S. Fallahi, M. J. Manfra, and D. J. Reilly. Cryogenic Control Architecture for Large-Scale Quantum Computing. *Physical Review Applied*, 3(2):024010, Feb. 2015. doi:10.1103/PhysRevApplied.3.024010.

[35] X. Hu and S. D. Sarma. Hilbert-space structure of a solid-state quantum computer: Two-electron states of a double-quantum-dot artificial molecule. *Physical Review A*, 61(6):062301, 2000. URL `http://journals.aps.org/pra/abstract/10.1103/PhysRevA.61.062301`.

[36] K. M. Itoh and H. Watanabe. Isotope engineering of silicon and diamond for quantum computing and sensing applications. *MRS Communications*, 4(4):143–157, Dec. 2014. doi:10.1557/mrc.2014.32.

[37] A. J. Kerman. Quantum information processing using quasiclassical electromagnetic interactions between qubits and electrical resonators. *New Journal of Physics*, 15(12):123011, Dec. 2013. doi:10.1088/1367-2630/15/12/123011.

[38] K. S. Keskar. Rf reactively sputtered superconducting NbNx films. *Journal of Applied Physics*, 45(7):3102, 1974. doi:10.1063/1.1663730.

[39] J. P. Kestner, X. Wang, L. S. Bishop, E. Barnes, and S. Das Sarma. Noise-Resistant Control for a Spin Qubit Array. *Physical Review Letters*, 110(14):140502, Apr. 2013. doi:10.1103/PhysRevLett.110.140502.

[40] M. S. Khalil, F. C. Wellstood, and K. D. Osborn. Loss Dependence on Geometry and Applied Power in Superconducting Coplanar Resonators. *IEEE Transactions on Applied Superconductivity*, 21(3):879–882, June 2011. doi:10.1109/TASC.2010.2090330.

[41] D. Kim, Z. Shi, C. B. Simmons, D. R. Ward, J. R. Prance, T. S. Koh, J. K. Gamble, D. E. Savage, M. G. Lagally, M. Friesen, S. N. Coppersmith, and M. A. Eriksson. Quantum control and process tomography of a semiconductor quantum dot hybrid qubit. *Nature*, 511(7507): 70–74, July 2014. doi:10.1038/nature13407.

[42] D. Klauser, W. Coish, and D. Loss. Nuclear spin state narrowing via gate-controlled Rabi oscillations in a double quantum dot. *Physical Review B*, 73(20), May 2006. doi:10.1103/PhysRevB.73.205302.

[43] S. Kogan. *Electronic Noise and Fluctuations in Solids*. Cambridge University Press, July 2008. ISBN 978-0-521-07019-5.

[44] A. J. Landig, J. V. Koski, P. Scarlino, U. C. Mendes, A. Blais, C. Reichl, W. Wegscheider, A. Wallraff, K. Ensslin, and T. Ihn. Coherent spin–photon coupling using a resonant exchange qubit. *Nature*, 560(7717):179, Aug. 2018. doi:10.1038/s41586-018-0365-y.

[45] A. J. Landig, J. V. Koski, P. Scarlino, C. Reichl, W. Wegscheider, A. Wallraff, K. Ensslin, and T. Ihn. Microwave cavity detected spin blockade in a few electron double quantum dot. *arXiv:1811.03907 [cond-mat]*, Nov. 2018. URL `http://arxiv.org/abs/1811.03907`.

[46] D. Leibfried. Toward Heisenberg-Limited Spectroscopy with Multiparticle Entangled States. *Science*, 304(5676):1476–1478, June 2004. doi:10.1126/science.1097576.

[47] D. Leibfried, R. Blatt, C. Monroe, and D. Wineland. Quantum dynamics of single trapped ions. *Reviews of Modern Physics*, 75(1):281, 2003. doi:10.1103/RevModPhys.75.281.

[48] D. T. Lennon, H. Moon, L. C. Camenzind, L. Yu, D. M. Zumbühl, G. A. D. Briggs, M. A. Osborne, E. A. Laird, and N. Ares. Efficiently measuring a quantum device using machine learning. *arXiv:1810.10042 [cond-mat, physics:quant-ph]*, Oct. 2018. URL `http://arxiv.org/abs/1810.10042`.

[49] P. H. Leung, K. A. Landsman, C. Figgatt, N. M. Linke, C. Monroe, and K. R. Brown. Robust 2-Qubit Gates in a Linear Ion Crystal Using a Frequency-Modulated Driving Force. *Physical Review Letters*, 120(2):020501, Jan. 2018. doi:10.1103/PhysRevLett.120.020501.

[50] J. Levy. Universal Quantum Computation with Spin-1/2 Pairs and Heisenberg Exchange. *Physical Review Letters*, 89(14), Sept. 2002. doi:10.1103/PhysRevLett.89.147902.

[51] R. Li, L. Petit, D. P. Franke, J. P. Dehollain, J. Helsen, M. Steudtner, N. K. Thomas, Z. R. Yoscovits, K. J. Singh, S. Wehner, L. M. K. Vandersypen, J. S. Clarke, and M. Veldhorst. A crossbar network for silicon quantum dot qubits. *Science Advances*, 4(7):eaar3960, July 2018. doi:10.1126/sciadv.aar3960.

[52] D. Loss and D. P. DiVincenzo. Quantum computation with quantum dots. *Physical Review A*, 57(1):120, 1998. doi:10.1103/PhysRevA.57.120.

[53] F. K. Malinowski, F. Martins, P. D. Nissen, E. Barnes, L. Cywiński, M. S. Rudner, S. Fallahi, G. C. Gardner, M. J. Manfra, C. M. Marcus, and F. Kuemmeth. Notch filtering the nuclear environment of a spin qubit. *Nature Nanotechnology*, 12(1):16–20, Jan. 2017. doi:10.1038/nnano.2016.170.

[54] F. Marsili, D. Bitauld, A. Gaggero, S. Jahanmirinejad, R. Leoni, F. Mattioli, and A. Fiore. Physics and application of photon number resolving detectors based on superconducting parallel nanowires. *New Journal of Physics*, 11(4):045022, Apr. 2009. doi:10.1088/1367-2630/11/4/045022.

[55] B. M. Maune, M. G. Borselli, B. Huang, T. D. Ladd, P. W. Deelman, K. S. Holabird, A. A. Kiselev, I. Alvarado-Rodriguez, R. S. Ross, A. E. Schmitz, M. Sokolich, C. A. Watson, M. F. Gyure, and A. T. Hunter. Coherent singlet-triplet oscillations in a silicon-based double quantum dot. *Nature*, 481(7381):344–347, Jan. 2012. doi:10.1038/nature10707.

[56] V. Mazzocchi, P. G. Sennikov, A. D. Bulanov, M. F. Churbanov, B. Bertrand, L. Hutin, J. P. Barnes, M. N. Drozdov, J. M. Hartmann, and M. Sanquer. 99.992 % ${2̂8}$Si CVD-grown epilayer on 300 mm substrates for large scale integration of silicon spin qubits. *Journal of Crystal Growth*, 509:1–7, Mar. 2019. doi:10.1016/j.jcrysgro.2018.12.010.

[57] J. Medford, J. Beil, J. M. Taylor, S. D. Bartlett, A. C. Doherty, E. I. Rashba, D. P. DiVincenzo, H. Lu, A. C. Gossard, and C. M. Marcus. Self-consistent measurement and state tomography of an exchange-only spin qubit. *Nature Nanotechnology*, 8(9):654–659, Sept. 2013. doi:10.1038/nnano.2013.168.

[58] S. Meenehan. APS -APS March Meeting 2019 - Event - Strategies for Automated Tune-up of Quantum Dot Arrays. In *Bulletin of the American Physical Society*. American Physical Society, Mar. 2019. URL `https://meetings.aps.org/Meeting/MAR19/Session/X34.4`.

[59] X. Mi, J. V. Cady, D. M. Zajac, P. W. Deelman, and J. R. Petta. Strong coupling of a single electron in silicon to a microwave photon. *Science*, 355(6321):156–158, Jan. 2017. doi:10.1126/science.aal2469.

[60] X. Mi, M. Benito, S. Putz, D. M. Zajac, J. M. Taylor, G. Burkard, and J. R. Petta. A coherent spin–photon interface in silicon. *Nature*, 555(7698):599–603, Mar. 2018. doi:10.1038/nature25769.

[61] S. Miyamoto and K. M. Itoh. Silicon Isotope Technology for Quantum Computing. In *2018 IEEE International Electron Devices Meeting (IEDM)*, pages 6.4.1–6.4.4, Dec. 2018. doi:10.1109/IEDM.2018.8614609.

[62] J. T. Muhonen, J. P. Dehollain, A. Laucht, F. E. Hudson, R. Kalra, T. Sekiguchi, K. M. Itoh, D. N. Jamieson, J. C. McCallum, A. S. Dzurak, and A. Morello. Storing quantum information for 30 seconds in a nanoelectronic device. *Nature Nanotechnology*, 9(12):986–991, Oct. 2014. doi:10.1038/nnano.2014.211.

[63] J. M. Nichol, L. A. Orona, S. P. Harvey, S. Fallahi, G. C. Gardner, M. J. Manfra, and A. Yacoby. High-fidelity entangling gate for double-quantum-dot spin qubits. *npj Quantum Information*, 3(1):3, Jan. 2017. doi:10.1038/s41534-016-0003-1.

[64] M. A. Nielsen. A simple formula for the average gate fidelity of a quantum dynamical operation. *Physics Letters A*, 303(4):249–252, Oct. 2002. doi:10.1016/S0375-9601(02)01272-0.

[65] M. A. Nielsen and I. L. Chuang. *Quantum Computation and Quantum Information*. Cambridge University Press, Oct. 2000. ISBN 978-0-521-63503-5.

[66] N. M. Nusran, M. U. Momeen, and M. V. G. Dutt. High-dynamic-range magnetometry with a single electronic spin in diamond. *Nature Nanotechnology*, 7(2):109–113, Dec. 2012. doi:10.1038/nnano.2011.225.

[67] J. Petta, A. Johnson, A. Yacoby, C. Marcus, M. Hanson, and A. Gossard. Pulsed-gate measurements of the singlet-triplet relaxation time in a two-electron double quantum dot. *Physical Review B*, 72(16), Oct. 2005. doi:10.1103/PhysRevB.72.161301.

[68] J. R. Petta, A. C. Johnson, J. M. Taylor, E. A. Laird, A. Yacoby, M. D. Lukin, C. M. Marcus, M. P. Hanson, and A. C. Gossard. Coherent manipulation of coupled electron spins in semiconductor quantum dots. *Science*, 309(5744):2180–2184, 2005. doi:10.1126/science.1116955.

[69] J. F. Poyatos, J. I. Cirac, and P. Zoller. Complete Characterization of a Quantum Process: The Two-Bit Quantum Gate. *Physical Review Letters*, 78(2):390–393, Jan. 1997. doi:10.1103/PhysRevLett.78.390.

[70] J. Preskill. Quantum Information and Computation: Lecture Notes for Physics 229, California Institute of Technology. Apr. 2016. URL `http://www.theory.caltech.edu/~preskill/ph219/ph219_2018-19`.

[71] J. Preskill. Quantum Computing in the NISQ era and beyond. *Quantum*, 2:79, Aug. 2018. doi:10.22331/q-2018-08-06-79.

[72] M. D. Reed, L. DiCarlo, S. E. Nigg, L. Sun, L. Frunzio, S. M. Girvin, and R. J. Schoelkopf. Realization of three-qubit quantum error correction with superconducting circuits. *Nature*, 482(7385):382–385, Feb. 2012. doi:10.1038/nature10786.

[73] D. J. Reilly. Engineering the quantum-classical interface of solid-state qubits. *npj Quantum Information*, 1:15011, Oct. 2015. doi:10.1038/npjqi.2015.11.

[74] D. J. Reilly, C. M. Marcus, M. P. Hanson, and A. C. Gossard. Fast single-charge sensing with a rf quantum point contact. *Applied Physics Letters*, 91(16):162101, 2007. doi:10.1063/1.2794995.

[75] S. M. Reimann and M. Manninen. Electronic structure of quantum dots. *Reviews of Modern Physics*, 74(4):1283–1342, Nov. 2002. doi:10.1103/RevModPhys.74.1283.

[76] S. Richer and D. DiVincenzo. Circuit design implementing longitudinal coupling: A scalable scheme for superconducting qubits. *Physical Review B*, 93(13):134501, Apr. 2016. doi:10.1103/PhysRevB.93.134501.

[77] C. F. Roos. Ion trap quantum gates with amplitude-modulated laser beams. *New Journal of Physics*, 10(1):013002, 2008. doi:10.1088/1367-2630/10/1/013002.

[78] D. Rosenberg, D. Kim, R. Das, D. Yost, S. Gustavsson, D. Hover, P. Krantz, A. Melville, L. Racz, G. O. Samach, S. J. Weber, F. Yan, J. L. Yoder, A. J. Kerman, and W. D. Oliver. 3D integrated superconducting qubits. *npj Quantum Information*, 3(1):42, Oct. 2017. doi:10.1038/s41534-017-0044-0.

[79] B. Royer, A. L. Grimsmo, N. Didier, and A. Blais. Fast and high-fidelity entangling gate through parametrically modulated longitudinal coupling. *Quantum*, 1:11, May 2017. doi:10.22331/q-2017-05-11-11.

[80] N. Samkharadze, A. Bruno, P. Scarlino, G. Zheng, D. P. DiVincenzo, L. DiCarlo, and L. M. K. Vandersypen. High-Kinetic-Inductance Superconducting Nanowire Resonators for Circuit QED in a Magnetic Field. *Physical Review Applied*, 5(4):044004, Apr. 2016. doi:10.1103/PhysRevApplied.5.044004.

[81] N. Samkharadze, G. Zheng, N. Kalhor, D. Brousse, A. Sammak, U. C. Mendes, A. Blais, G. Scappucci, and L. M. K. Vandersypen. Strong spin-photon coupling in silicon. *Science*, 359(6380):1123–1127, Mar. 2018. doi:10.1126/science.aar4054.

[82] M. D. Schroer and J. R. Petta. Quantum dots: Time to get the nukes out. *Nature Physics*, 4 (7):516–518, July 2008. doi:10.1038/nphys1007.

[83] M. J. A. Schuetz, G. Giedke, L. M. K. Vandersypen, and J. I. Cirac. High-fidelity hot gates for generic spin-resonator systems. *Physical Review A*, 95(5):052335, May 2017. doi:10.1103/PhysRevA.95.052335.

[84] A. Sergeevich, A. Chandran, J. Combes, S. D. Bartlett, and H. M. Wiseman. Characterization of a qubit Hamiltonian using adaptive measurements in a fixed basis. *Physical Review A*, 84 (5):052315, 2011. doi:10.1103/PhysRevA.84.052315.

[85] M. Shulman. *Entanglement and Metrology with Singlet-Triplet Qubits*. PhD thesis, Harvard University, 2015.

[86] M. D. Shulman, O. E. Dial, S. P. Harvey, H. Bluhm, V. Umansky, and A. Yacoby. Demonstration of Entanglement of Electrostatically Coupled Singlet-Triplet Qubits. *Science*, 336 (6078):202–205, Apr. 2012. doi:10.1126/science.1217692.

[87] M. D. Shulman, S. P. Harvey, J. M. Nichol, S. D. Bartlett, A. C. Doherty, V. Umansky, and A. Yacoby. Suppressing qubit dephasing using real-time Hamiltonian estimation. *Nature Communications*, 5:5156, Oct. 2014. doi:10.1038/ncomms6156.

[88] J. Stehlik, Y.-Y. Liu, C. M. Quintana, C. Eichler, T. R. Hartke, and J. R. Petta. Fast Charge Sensing of a Cavity-Coupled Double Quantum Dot Using a Josephson Parametric Amplifier. *Physical Review Applied*, 4(1):014018, July 2015. doi:10.1103/PhysRevApplied.4.014018.

[89] A. Stockklauser, P. Scarlino, J. Koski, S. Gasparinetti, C. K. Andersen, C. Reichl, W. Wegscheider, T. Ihn, K. Ensslin, and A. Wallraff. Strong Coupling Cavity QED with Gate-Defined Double Quantum Dots Enabled by a High Impedance Resonator. *Physical Review X*, 7(1), Mar. 2017. doi:10.1103/PhysRevX.7.011030.

[90] T. H. Taminiau, J. Cramer, T. van der Sar, V. V. Dobrovitski, and R. Hanson. Universal control and error correction in multi-qubit spin registers in diamond. *Nature Nanotechnology*, 9 (3):171–176, Mar. 2014. doi:10.1038/nnano.2014.2.

[91] J. D. Teske, S. Humpohl, R. Otten, P. Bethke, P. Cerfontaine, J. Dedden, A. Ludwig, A. D. Wieck, and H. Bluhm. A Machine Learning Approach for Automated Fine-Tuning of Semiconductor Spin Qubits. *arXiv:1901.01972 [cond-mat]*, Jan. 2019. URL `http://arxiv.org/abs/1901.01972`.

[92] J. D. Teufel. *Superconducting Tunnel Junctions as Direct Detectors for Submillimeter Astronomy*. PhD thesis, Yale University, 2008.

[93] G. S. Uhrig. Exact results on dynamical decoupling by π pulses in quantum information processes. *New Journal of Physics*, 10(8):083024, Aug. 2008. doi:10.1088/1367-2630/10/8/083024.

[94] W. G. van der Wiel, S. De Franceschi, J. M. Elzerman, T. Fujisawa, S. Tarucha, and L. P. Kouwenhoven. Electron transport through double quantum dots. *Reviews of Modern Physics*, 75(1):1, 2002. doi:10.1103/RevModPhys.75.1.

[95] C. J. van Diepen, P. T. Eendebak, B. T. Buijtendorp, U. Mukhopadhyay, T. Fujita, C. Reichl, W. Wegscheider, and L. M. K. Vandersypen. Automated tuning of inter-dot tun-

nel coupling in double quantum dots. *Applied Physics Letters*, 113(3):033101, July 2018. doi:10.1063/1.5031034.

[96] M. Veldhorst, J. C. C. Hwang, C. H. Yang, A. W. Leenstra, B. de Ronde, J. P. Dehollain, J. T. Muhonen, F. E. Hudson, K. M. Itoh, A. Morello, and A. S. Dzurak. An addressable quantum dot qubit with fault-tolerant control-fidelity. *Nature Nanotechnology*, 9(12):981–985, Oct. 2014. doi:10.1038/nnano.2014.216.

[97] M. Veldhorst, C. H. Yang, J. C. C. Hwang, W. Huang, J. P. Dehollain, J. T. Muhonen, S. Simmons, A. Laucht, F. E. Hudson, K. M. Itoh, A. Morello, and A. S. Dzurak. A two-qubit logic gate in silicon. *Nature*, 526(7573):410–414, Oct. 2015. doi:10.1038/nature15263.

[98] J. J. Viennot, M. C. Dartiailh, A. Cottet, and T. Kontos. Coherent coupling of a single spin to microwave cavity photons. *Science*, 349(6246):408–411, July 2015. doi:10.1126/science.aaa3786.

[99] G. Waldherr, J. Beck, P. Neumann, R. S. Said, M. Nitsche, M. L. Markham, D. J. Twitchen, J. Twamley, F. Jelezko, and J. Wrachtrup. High-dynamic-range magnetometry with a single nuclear spin in diamond. *Nature Nanotechnology*, 7(2):105–108, Feb. 2012. doi:10.1038/nnano.2011.224.

[100] G. Waldherr, Y. Wang, S. Zaiser, M. Jamali, T. Schulte-Herbrüggen, H. Abe, T. Ohshima, J. Isoya, J. F. Du, P. Neumann, and J. Wrachtrup. Quantum error correction in a solid-state hybrid spin register. *Nature*, 506(7487):204–207, Feb. 2014. doi:10.1038/nature12919.

[101] T. F. Watson, S. G. J. Philips, E. Kawakami, D. R. Ward, P. Scarlino, M. Veldhorst, D. E. Savage, M. G. Lagally, M. Friesen, S. N. Coppersmith, M. A. Eriksson, and L. M. K. Vandersypen. A programmable two-qubit quantum processor in silicon. *Nature*, 555(7698):633–637, Mar. 2018. doi:10.1038/nature25766.

[102] A. West, B. Hensen, A. Jouan, T. Tanttu, C.-H. Yang, A. Rossi, M. F. Gonzalez-Zalba, F. Hudson, A. Morello, D. J. Reilly, and A. S. Dzurak. Gate-based single-shot readout of spins in silicon. *Nature Nanotechnology*, page 1, Mar. 2019. doi:10.1038/s41565-019-0400-7.

[103] A. Wild, J. Kierig, J. Sailer, J. W. Ager, E. E. Haller, G. Abstreiter, S. Ludwig, and D. Bougeard. Few electron double quantum dot in an isotopically purified 28Si quantum well. *Applied Physics Letters*, 100(14):143110, Apr. 2012. doi:10.1063/1.3701588.

[104] H. M. Wiseman and G. J. Milburn. *Quantum Measurement and Control*. Cambridge University Press, 2010. ISBN 978-0-521-80442-4.

[105] X. Wu, D. R. Ward, J. R. Prance, D. Kim, J. K. Gamble, R. T. Mohr, Z. Shi, D. E. Savage, M. G. Lagally, M. Friesen, S. N. Coppersmith, and M. A. Eriksson. Two-axis control of a singlet–triplet qubit with an integrated micromagnet. *Proceedings of the National Academy of Sciences*, 111(33):11938–11942, Aug. 2014. doi:10.1073/pnas.1412230111.

[106] J. Yoneda, K. Takeda, T. Otsuka, T. Nakajima, M. R. Delbecq, G. Allison, T. Honda, T. Kodera, S. Oda, Y. Hoshi, N. Usami, K. M. Itoh, and S. Tarucha. A quantum-dot spin qubit with coherence limited by charge noise and fidelity higher than 99.9%. *Nature Nanotechnology*, page 1, Dec. 2017. doi:10.1038/s41565-017-0014-x.

[107] D. M. Zajac, T. M. Hazard, X. Mi, E. Nielsen, and J. R. Petta. Scalable Gate Architecture for a One-Dimensional Array of Semiconductor Spin Qubits. *Physical Review Applied*, 6(5): 054013, Nov. 2016. doi:10.1103/PhysRevApplied.6.054013.

[108] D. M. Zajac, A. J. Sigillito, M. Russ, F. Borjans, J. M. Taylor, G. Burkard, and J. R. Petta. Resonantly driven CNOT gate for electron spins. *Science*, 359(6374):439–442, Jan. 2018. doi:10.1126/science.aao5965.

[109] G. Zheng, N. Samkharadze, M. L. Noordam, N. Kalhor, D. Brousse, A. Sammak, G. Scappucci, and L. M. K. Vandersypen. Rapid high-fidelity gate-based spin read-out in silicon. *arXiv:1901.00687 [cond-mat, physics:quant-ph]*, Jan. 2019. URL `http://arxiv.org/abs/1901.00687`.